Measurement of differential di-photon plus jet cross sections using the ATLAS detector

Martin Florian Bessner

Department of Physics

University of Hamburg

PhD thesis in Physics

This PhD thesis has been carried out
by Martin Florian Bessner,
born in Heidelberg, Germany,
at the
Deutsches Elektronen-Synchrotron
under the supervision of
Dr. Kerstin Tackmann and Prof. Dr. Peter Schleper

April 2017

Abstract: Measurement of differential di-photon plus jet cross sections using the ATLAS detector

A good understanding of the strong interaction is crucial for every experiment at a hadron collider. Events with photons provide a direct access to study processes of the strong interaction. This thesis presents the measurement of differential cross sections of events with two photons as a function of the number of hadronic jets. Photons are required to be isolated from hadronic activity in the event. Collision data is used corresponding to an integrated luminosity of 20.3 fb^{-1} at a proton-proton collision energy of $\sqrt{s} = 8$ TeV collected by the ATLAS detector at the Large Hadron Collider (LHC) in 2012.

The dominant background contribution comes from hadronic jets which are identified as photons, occurring mainly when a π^0 carries most of the jet energy. Two methods to remove this contribution are presented. A smaller background contribution arising from electrons misidentified as photons is removed as well. The measured event yields are corrected for detector inefficiencies and resolution effects. An unfolding method based on singular value decomposition of the resolution matrix is extended to two-dimensional distributions and applied to the reconstructed distributions. All systematic uncertainties are evaluated, the dominant uncertainties arise from the jet background subtraction and the uncertainty in the jet energy scale.

16 observables are studied to explore the photon and jet kinematics. Double differential cross sections are shown as function of those observables and the number of jets, both inclusively ($\geq n$ jets) and exclusively ($= n$ jets). The results are compared to theoretical predictions from SHERPA, PYTHIA and GOSAM.

Kurzfassung: Messung differenzieller Wirkungsquerschnitte von Ereignissen mit zwei Photonen und Jets mit dem ATLAS-Detektor

Ein gutes Verständnis der starken Wechselwirkung ist entscheidend für jedes Experiment an Hadronen-Speicherringen. Ereignisse mit Photonen bieten einen direkten Zugang, um Prozesse der starken Wechselwirkung zu untersuchen. Diese Arbeit stellt die Messung des differentiellen Wirkungsquerschnitts von Ereignissen mit zwei Photonen in Abhängigkeit der Zahl der hadronischen Teilchenjets vor. Die Photonen müssen isoliert von hadronischer Aktivität im Ereignis sein. Die verwendeten Daten von Proton-Proton-Kollisionen bei einer Schwerpunktsenergie von $\sqrt{s} = 8$ TeV entsprechen einer integrierten Luminosität von 20,3 fb^{-1}. Sie wurden 2012 mit dem ATLAS-Detektor am Large Hadron Collider (LHC) gesammelt.

Der wichtigste Untergrundprozess kommt von hadronischen Jets, die als Photonen rekonstruiert werden, insbesondere wenn ein π^0 den größten Teil der Jetenergie erhält. Zwei Methoden, um diesen Beitrag zu entfernen, werden vorgestellt. Ein kleinerer Beitrag zum Untergrund kommt von Elektronen, dieser Beitrag wird ebenfalls subtrahiert. Die gemessenen Ereignisraten werden korrigiert, um Detektor-Ineffizienzen und Auflösungseffekte zu berücksichtigen. Eine Entfaltungsmethode, “SVD unfolding”, wird auf zweidimensionale Verteilungen erweitert und angewendet. Alle systematischen Unsicherheiten werden bestimmt, die Subtraktion des hadronischen Untergrunds und die Unsicherheit in der Energieskala der Jets sind dominant.

16 Observablen werden untersucht, um die Kinematik der Photonen und Jets im Ereignis zu studieren. Die differentiellen Wirkungsquerschnitte werden als Funktion dieser Observablen und der Zahl der Jets bestimmt, sowohl inklusiv ($\geq n$ Jets) als auch exclusiv ($= n$ Jets). Die Ergebnisse werden mit theoretischen Vorhersagen von SHERPA, PYTHIA und GOSAM verglichen.

Contents

Chapter 1

Introduction

The Large Hadron Collider (LHC) at CERN in Geneva is the world's largest and highest-energetic particle accelerator. In the LHC, proton beams with an energy of up to 6.5 TeV per proton (design: 7 TeV) are collided in four main detectors: ATLAS, CMS, ALICE and LHCb. The first collisions took place in 2009, with regular operation from 2010 to 2012 and since 2015.

The primary target of the LHC detectors is the search for physics beyond the Standard Model of particle physics (Standard Model), together with precision measurements of parameters of the Standard Model. One of the main results so far was the discovery of a new boson, which has been identified as a Higgs boson [1]. Nuclear physics is explored with proton-lead and lead-lead collisions, mainly with the ALICE detector.

The Standard Model is well established. Up to now, no striking violation from its predictions was found by particle physics experiments. However, it is known that the Standard Model is incomplete, as it has theoretical limits for high energies and it cannot describe experimental results from cosmology such as the size of the matter-antimatter asymmetry or the nature of dark matter. In addition, it does not include gravity. Therefore, it is expected that the Standard Model is only an effective description of a more general theory.

There are two different approaches to search for possible new effects, both are pursued at the LHC detectors: In the first approach one searches for the production of new particles by reconstructing them via their decay products. ATLAS and CMS focus on this direct method to probe new effects. The other possibility is to perform precision measurements of decay properties of particles already known, as new physics can alter the decay properties. While LHCb is specialized on this approach, ATLAS and CMS do precision measurements as well.

The ATLAS detector is a general purpose detector around one of the beam interaction points in the LHC. It covers the pseudo-rapidity range of $|\eta| < 4.9$ [1] with various subsystems designed to identify different particle types and measure

---

[1] The pseudo-rapidity η is defined as $\eta = -\log\left(\tan\frac{\theta}{2}\right)$ with the polar angle θ.

their momenta. Apart from neutrinos, all known particles can be detected, either directly if they traverse the detector or indirectly via their decay products. Unknown particles can be detected via their decay products (if they are short-living), via their interactions in the detector (if they are long-living and charged) or via an imbalance of transverse momentum (if they are long-living and uncharged).

High-energetic hadron collisions typically produce tens of particles per collision via the strong interaction. Understanding the strong interaction is therefore crucial for every experiment. A better understanding improves theoretical predictions for signal shapes and background contributions in all analyses. The strong interaction can be studied via the production of particle jets that come directly from quarks and gluons. A complementary approach is the study of particles that couple to quarks, but do not participate in the strong interaction, in particular photons and W and Z bosons. They give a more direct access to hard interaction processes as they do not participate in hadronization. The ATLAS physics program covers a large variety of measurements of final states involving jets, photons, W and Z bosons that complement each other. This thesis presents a measurement of double differential cross sections for events with two photons as function of the number of jets and 16 observables. The large number of studied observables makes the comparison with theoretical predictions more powerful and makes it easier to identify regions of the phase space where the theoretical description has to be improved.

In chapter 2, the ATLAS detector is introduced. The Standard Model and the ATLAS physics program are described in chapter 3, with a focus on photon physics. Object reconstruction and identification are presented in chapter 4, with a focus on photons and jets. Chapter 5 describes the study of diphoton production in association with jets, using the dataset collected in 2012: After an introduction (5.1), the event selection is shown (5.2), followed by the background subtraction (5.3 to 5.5) and a discussion of the Higgs contribution (5.6). The efficiency of the event selection is studied (5.7). The correction for resolution effects is described (5.8), systematic uncertainties are evaluated (5.9), and the results are shown (5.10). Chapter 6 contains the summary.

Chapter 2

LHC and ATLAS Detector

2.1 LHC

The LHC is a circular proton-proton collider at CERN in Switzerland. It is the world's largest accelerator with a circumference of 27 km, reaching the highest collision energies ever achieved: The design center-of-mass energy is 14 TeV, up to 13 TeV have been achieved until 2016. Protons are sent through several pre-accelerators until they are injected into the LHC ring at an energy of 450 GeV per proton, where they are accelerated to the collision energy. About 2800 bunches with about 110 billion protons fit in each bunch, with a regular separation of 25 nanoseconds between the bunches, corresponding to a distance of 7.5 meters. Some gaps between bunches have to be larger due to the injection and beam dump procedures. Collisions started in 2009 at low energy, regular operation has taken place from 2010 to 2012 ("Run 1") and since 2015 ("Run 2").

The design luminosity is 10^{34} cm^{-2}s^{-1}, the highest achieved luminosity is $1.4 \cdot 10^{34}$ cm^{-2}s^{-1} [2].

2.2 Overview

The ATLAS detector is a general-purpose detector designed to exploit the full physics potential of the LHC [3]. The overall layout is shown in figure 2.1. The detector has a roughly cylindrical shape with a length of 44 meters, a diameter of 25 meters and a total mass of 7000 tons. It is the largest particle detector constructed at an accelerator so far. With multiple layers of different subdetectors arranged around the central interaction point, it covers the pseudorapidity range of $|\eta| < 4.9$. The subdetectors are designed to identify particles and measure the momenta of different particle types.

Around the interaction point, a silicon pixel detector forms the innermost subsystem, followed by a silicon strip detector (SCT) and a transition radiation tracker (TRT). Together, these subsystems form the inner detector. It is surrounded by a thin superconducting solenoid, producing a magnetic field of about

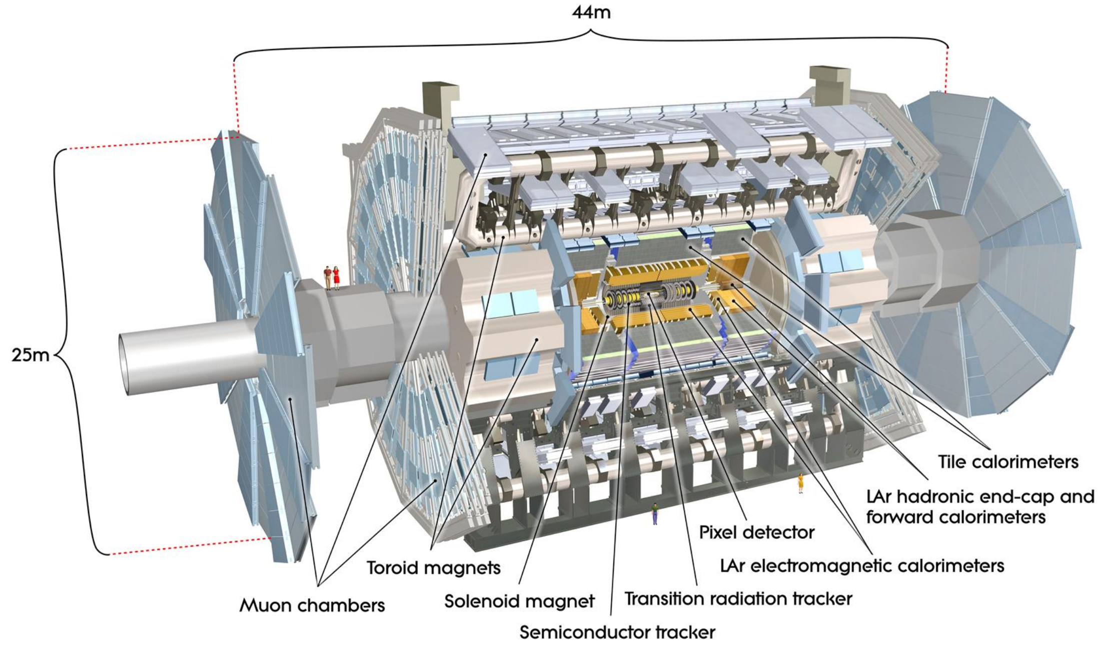

Figure 2.1: *Layout of the ATLAS detector. Humans are shown for scale comparison. Taken from [3].*

2 T. This field bends the tracks of charged particles and allows to measure their momenta. The inner detector covers the pseudorapidity range of $|\eta| < 2.5$.

The calorimeter system surrounds the inner detector. It is split into an electromagnetic and a hadronic calorimeter. The outermost subsystem is the muon detector, it has its own toroidal magnetic field to measure the momentum of muons.

ATLAS uses a cartesian coordinate system centered at the nominal interaction point. The positive x-axis is pointing towards the center of the ring, the positive y-axis is pointing upwards, the z-axis is pointing along the beam axis. Three other parameters are frequently used as they have a closer relation to the processes studied: the azimuthal angle ϕ (where $\tan\phi = \frac{y}{x}$) and radius R in the x-y-plane, and the pseudorapidity $\eta = -\log\left(\tan\frac{\theta}{2}\right)$, where the polar angle θ is the angle relative to the beam axis.

The LHC beams travel roughly along the z-axis and collide in the origin of the coordinate system. Some processes studied at the LHC detectors are extremely rare. To maximize the discovery potential, the number of collisions has to be as large as reasonably possible. Therefore, multiple simultaneous proton-proton collisions per bunch crossing are necessary. In 2012 and 2016, about 40 collisions per bunch crossing were achieved, the distribution for 2012 is shown in figure 2.2. Only a small fraction of those events is of interest for data analysis, the other collisions are called pileup.

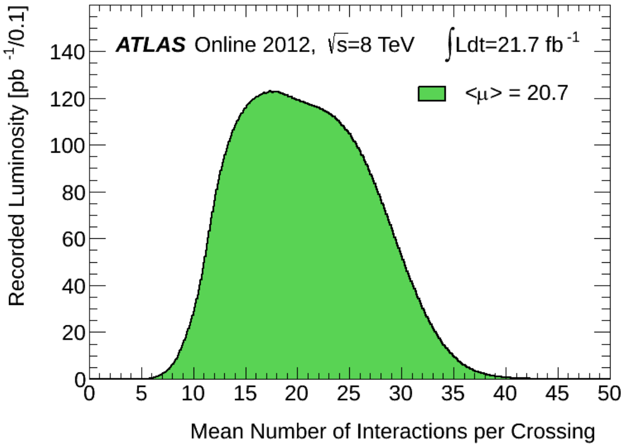

Figure 2.2: *Distribution of the mean number of pileup interactions per bunch crossing in 2012. The average is 20.7, but up to 40 collisions per bunch crossing were achieved. Taken from [4].*

After first collisions in 2009, regular data-taking at the LHC started in 2010 with a small dataset (37 pb^{-1}) at a center-of-mass energy of $\sqrt{s} = 7$ TeV. Larger datasets were collected during 2011 (5.1 fb^{-1} at $\sqrt{s} = 7$ TeV) and 2012 (21.3 fb^{-1} at $\sqrt{s} =$ 8 TeV), and, after upgrades of the accelerator and detectors, during 2015 and 2016 at $\sqrt{s} =$ 13 TeV.

The LHC running conditions lead to challenging conditions for the ATLAS subdetectors: They have to be fast (25 ns between bunch crossings) and very radiation tolerant (more than 1 MGy for some subdetectors). At the same time, they need a high granularity to track the individual particles crossing the detector. In addition, the solid angle covered should be as large as possible and without gaps to maximize the probability to detect particles.

For charged particles, a good momentum resolution and the ability to reconstruct secondary vertices from particle decays are crucial. The total energy of electrons, photons and hadronic jets has to be measured accurately in the calorimeters. Muons are measured accurately with the muon spectrometer, which achieves a good momentum measurement even for high-energetic muons (10% uncertainty for $p_T = 1$ TeV muons).

In the following sections, the detector components are described individually.

2.3 Inner detector

The inner detector with its pixel detector, strip detector and transition radiation tracker provides a tracking system within the pseudorapidity range of $|\eta| < 2.5$, capable of measuring momenta of charged particles with a typical resolution of

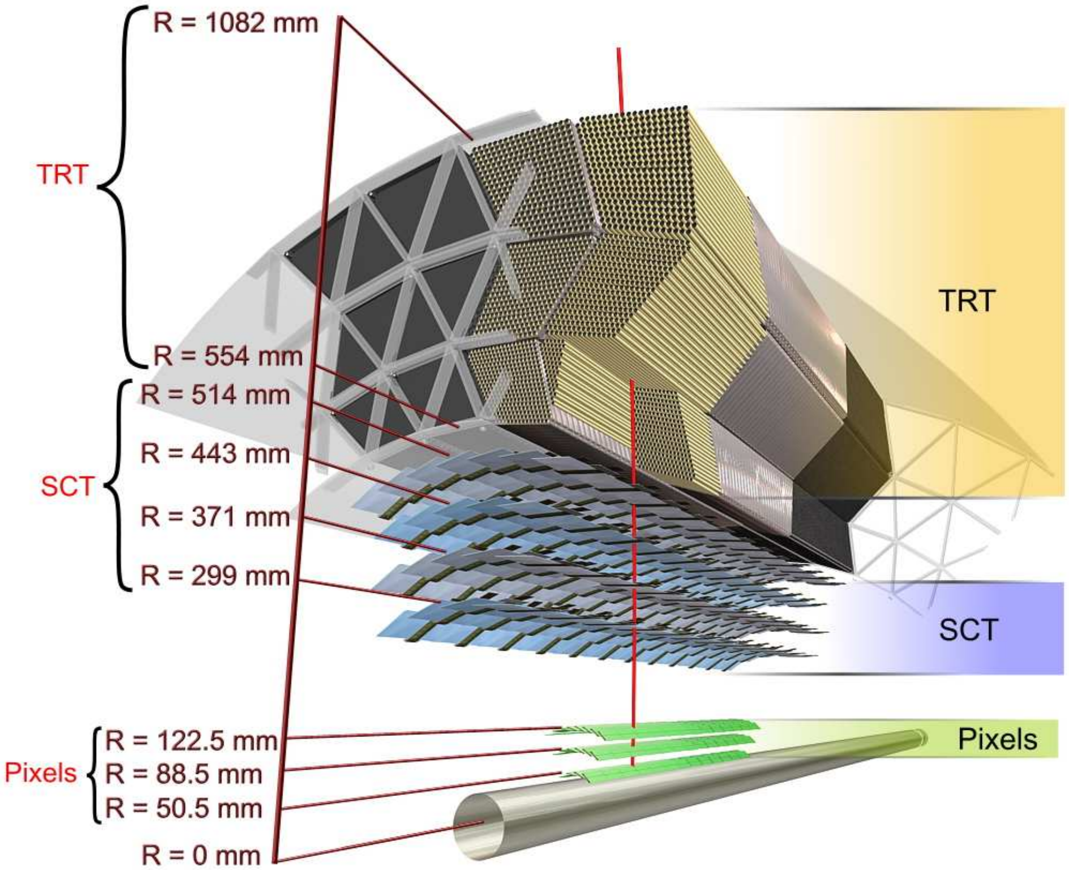

Figure 2.3: *Schematic of the inner detector used in Run 1. SCT is the silicon strip detector. The red line symbolizes a charged track with a transverse momentum of* $p_T = 10$ GeV *and* $\eta = 0.3$. *Taken from [3].*

2-4%, even in the presence of high pileup. About 1000 particles traversed the inner detector per bunch crossing at the running conditions of 2012 and 2016. The layout of the inner detector is shown in figure 2.3.

2.3.1 Silicon pixel detector

The silicon pixel detector [5] consists of a barrel section and two endcap sections, symmetric around the interaction point. The barrel is located at a radius of 5 cm $< R <$ 12 cm around the beam axis and within $|z| <$ 40 cm, while the endcaps span the range 9 cm $< R <$ 15 cm and 50 cm $< |z| <$ 65 cm, where all values are rounded to centimeters. The barrel has three cylindrical layers of pixel detectors, while the endcaps have 3 disks each. The pixel size is 50 × 400 μm^2, with the shorter dimension in the ϕ direction. In total, the pixel detector has about 80 million channels.

During the upgrade phase 2013-2014, the old beam pipe was replaced with a new beam pipe with smaller diameter, in order to make space for another layer of pixel detector directly around the new beam pipe. This additional component is called Insertable B-Layer (IBL) [6].

2.3.2 Silicon strip detector

The silicon strip detector [7] is located around the pixel detector, at a radius of about 25 cm to 60 cm and up to $|z| < 280$ cm. The barrel consists of 4 layers, the two endcaps have 9 disks each. Sensors are on both sides of the layers. The strips with a length between 5 and 13 cm have a pitch of 80 μm, they are aligned with the z-direction in the barrel and with the R-direction in the endcaps. To retain some resolution in this direction, the two sides in each layer are rotated by a stereo-angle of 40 mrad relative to each other.

2.3.3 Transition radiation tracker

The transition radiation tracker (TRT) [8] is located around the silicon strip detector, at a radius of about 60 cm to 110 cm, and extends up to $|z| = 274$ cm, corresponding to a pseudorapidity of $|\eta| < 2$. It uses polyimide straw tubes with a diameter of 4 mm, the signal is collected with gold-plated tungsten anodes inside. A measurement of the time between the particles passing through and the signal arriving at the readout allows to measure the distance between track and wire with an accuracy of 130 μm.

X-ray transition radiation can be emitted when particles cross the border between materials with different dielectric properties. This happens in the straws, in scintillating foils and in the carbon fibers between the straws. In the endcaps, additional foils increase the amount of transition radiation. The conversion of the emitted x-ray photons, mainly due to xenon gas in the detector, leads to a large signal in individual straws. The readout can distinguish between a small signal (from ionization along tracks) and a large signal (from transition radiation). Due to their larger Lorentz factor, electrons are much more likely to emit transition radiation. Up to 2012, a gas mixture of 70% Xe, 27% CO_2 and 3% O_2 was used, from 2015 onwards the mixture was changed to $Ar/CO_2/O_2$ in some segments that show gas leakage. Argon is more easily available, but leads to a lower x-ray detection efficiency, reducing the electron identification efficiency [9].

The TRT allows tracking particles and distinguishing electrons from other charged particles. While it has a lower spatial resolution per hit than the silicon detectors, it records more hits (typically 35 per track) and has a larger radius, improving the overall tracking performance.

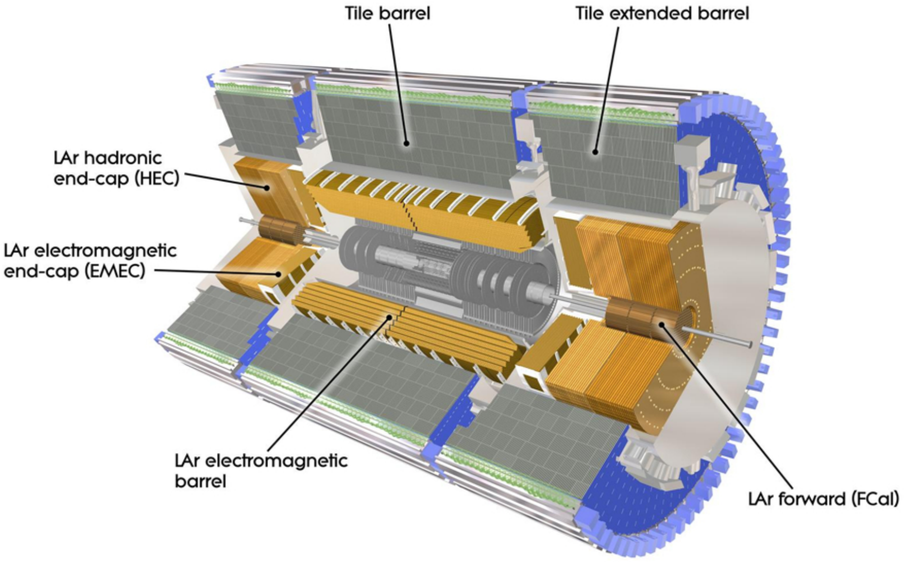

Figure 2.4: *Schematic of the calorimeter system [3].*

2.4 Calorimeters

The calorimeters provide total energy measurements for all particles apart from muons and neutrinos. This is especially important for neutral particles like photons and neutrons, as they cannot be measured in the tracking detectors. The energy measurement of electrons is based on the calorimeters to take Bremsstrahlung into account. The energy of jets is measured with the calorimeters as well. The inner part of the calorimeters is the electromagnetic calorimeter, which measures the energy of electromagnetic showers. Hadronic showers typically start in the electromagnetic calorimeter but deposit most of their energy in the following hadronic calorimeter. The ATLAS calorimeters are sampling calorimeters — active layers measure the deposited energy, while absorbers between the active layers are used to speed up showering in order to keep the overall size and cost of the calorimeters reasonable. The overall layout is shown in figure 2.4.

2.4.1 Electromagnetic calorimeter

The electromagnetic calorimeter [10] primarily measures the energy of electrons and photons. It is a liquid argon sampling calorimeter with absorber plates made out of lead and steel, arranged in an accordion shape in the (R-ϕ) plane to provide a ϕ coverage without cracks. The barrel calorimeter covers the pseudorapidity range of $|\eta| < 1.475$, while the endcap calorimeter is installed in the range of $1.375 < |\eta| < 3.2$. The two ranges overlap as the borders of the components are aligned with the x-y-plane, not with the direction of constant pseudorapidity (see

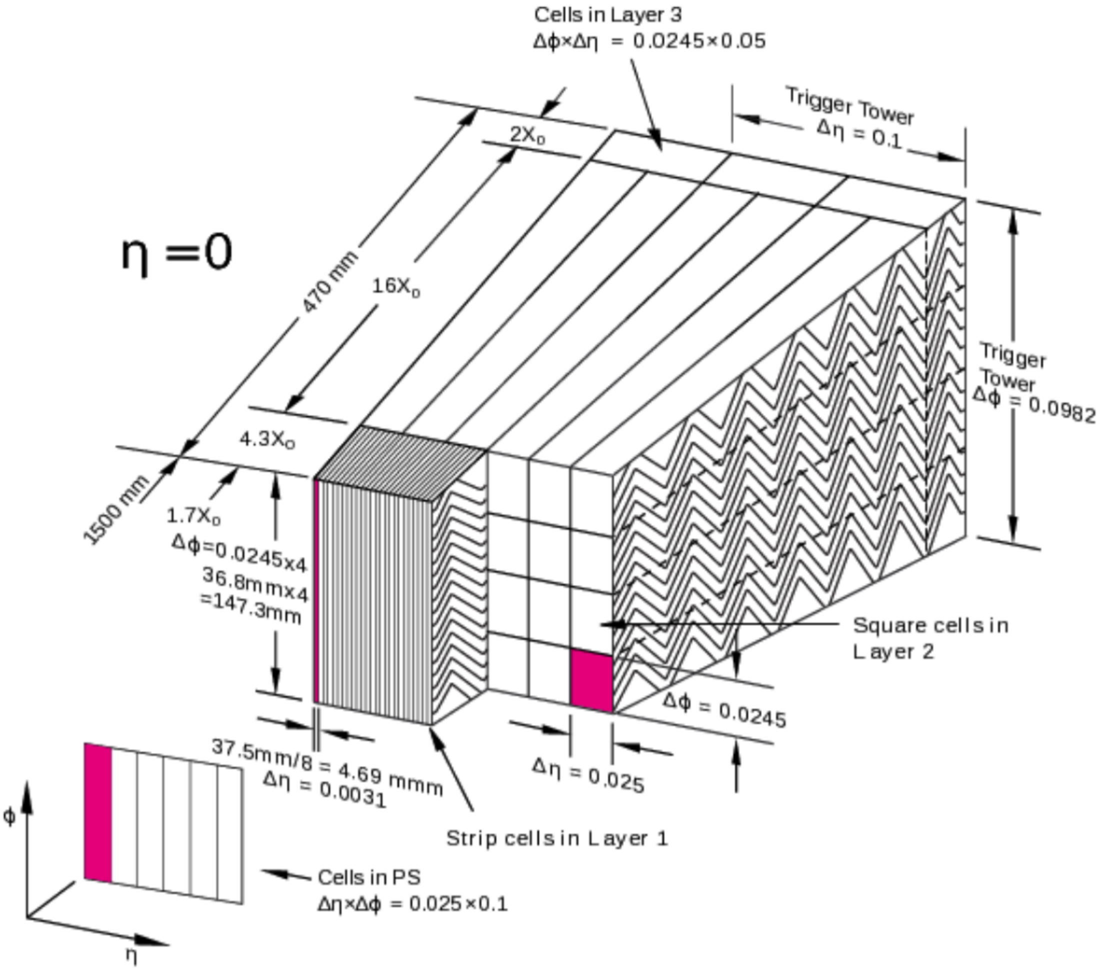

Figure 2.5: *Schematic of the electromagnetic calorimeter. Taken from [3].*

figure 2.4). The layout of the electromagnetic calorimeter is shown in figure 2.5. The calorimeter consists of three layers with an additional presampling detector in front. The presampling layer [11], located in front of the first layer of the electromagnetic calorimeter for $|\eta| < 1.8$, has 11 mm of active liquid argon. The granularity in the (η-ϕ) plane is 0.025×0.1. It allows to estimate the energy loss in the inner detector, the superconducting solenoid and the calorimeter cryostat. The presampling calorimeter improves the energy resolution by up to 40%.

The first layer of the main calorimeter has a fine granularity (0.0031 in η, 0.098 in ϕ), this is important in the photon identification (see section 4.4). The second layer has a larger granularity of 0.025×0.0245 in the η-ϕ plane. Most of the energy of electromagnetic showers is deposited here. The third layer captures the tails of the shower with a larger granularity of 0.05×0.0245.

Readout electrodes in the middle of the active regions. The drift gap of 2.1 millimeters leads to a total drift time of about 500 ns. As this is long compared to the bunch crossing period of 25 ns, the signals of multiple bunch crossings overlap in the calorimeter.

In total, the electromagnetic calorimeter has a depth of at least 22 electromagnetic radiation lengths everywhere. The energy resolution has been determined as

$$\frac{\sigma(E)}{E} = \frac{a}{\sqrt{E/\mathrm{GeV}}} \oplus b \tag{2.1}$$

where E/GeV is the particle energy in GeV, a=10% describes the stochastic term, and b=0.17% is a constant. The stochastic term comes from the limited number of particles in the shower, the variable fraction of energy deposited in the active part of the calorimeter and the randomness involved in the production of a signal in the active elements.

2.4.2 Hadronic calorimeter

The hadronic calorimeter [12] measures the energy of all hadronic showers. In the barrel for $|\eta| < 1.7$, it is built as a sampling tile calorimeter with scintillators as active material and steel absorbers, where each module covers a range of 0.1 in ϕ and approximately 0.1 in η. The barrel has a depth of about 7.4 hadronic interaction lengths. The endcaps are sampling calorimeters based on liquid argon as active material with copper absorbers. They cover the range of $1.5 < |\eta| < 4.9$ with a cell size of 0.1×0.1 up to $|\eta| = 2.5$, and 0.2×0.2 for larger pseudorapidities.

The region of $3.1 < |\eta| < 4.9$ uses a matrix of copper tubes and plates as absorber in the first layer, this layer serves as extension of the electromagnetic calorimeter. Tungsten is used as absorber in the following two layers serving as hadronic calorimeter. Combined, the three layers have a depth of 10.54 hadronic interaction lengths.

The energy resolution has been determined as

$$\frac{\sigma(E)}{E} = \frac{a}{\sqrt{E/\mathrm{GeV}}} \oplus b \tag{2.2}$$

where E/GeV is the particle energy in GeV, a=50% describes the stochastic term, and b=3% is a constant [13].

2.5 Muon system

The muon system [14] is the outermost part of the ATLAS detector and takes up most of its volume. It has a large toroidal magnetic field in the barrel and smaller toroidal end-cap magnets which allow a momentum measurement up to $|\eta| = 2.7$. Muon detection is done with a combination of four different methods used in different parts of the detector: drift tubes, cathode-strip chambers, resistive-plate chambers and thin-gap chambers, where the first two types are used for precision tracking and the last two types are mainly used for triggering.

Chapter 3

Physics at the ATLAS detector

3.1 The Standard Model

Current knowledge about particle physics can be summarized in a theory called the Standard Model of particle physics (SM). The Standard Model is extremely successful. Apart from one exception (the masses of neutrinos), it allows to describe all experimental observations in particle physics so far. The most precise measurements have 13 significant figures (electron g-factor) and still agree with theory predictions [15]. Despite this success, the Standard Model does not include gravity, it does not work for arbitrarily high energies, and it cannot answer several open questions both from the theoretical side and from observations in cosmology. Therefore, several extensions of the Standard Model have been proposed, the most prominent group of extensions is called supersymmetry.

This chapter summarizes the main concepts of the Standard Model and introduces supersymmetry as a possible extension.

The Standard Model is based on quantum field theory. Matter particles are described by fermionic fields, while interactions are described by bosonic fields based on a gauge symmetry. The interactions can be studied by the direct production of their corresponding bosons or by their influence on fermions.

Fermions

There are two classes of fermions in the Standard Model, quarks and leptons. While all quarks have an electric charge, there are charged leptons and uncharged leptons (neutrinos). All types of leptons can be grouped into three families. Each family consists of one “up-type” quark, one “down-type” quark, one charged lepton and one neutrino. The main difference between the families is the mass of the corresponding particles. An overview of all particles in the Standard Model is shown in figure 3.1.

Due to the spin-statistics theorem [16], all fermions have half-integer spin.

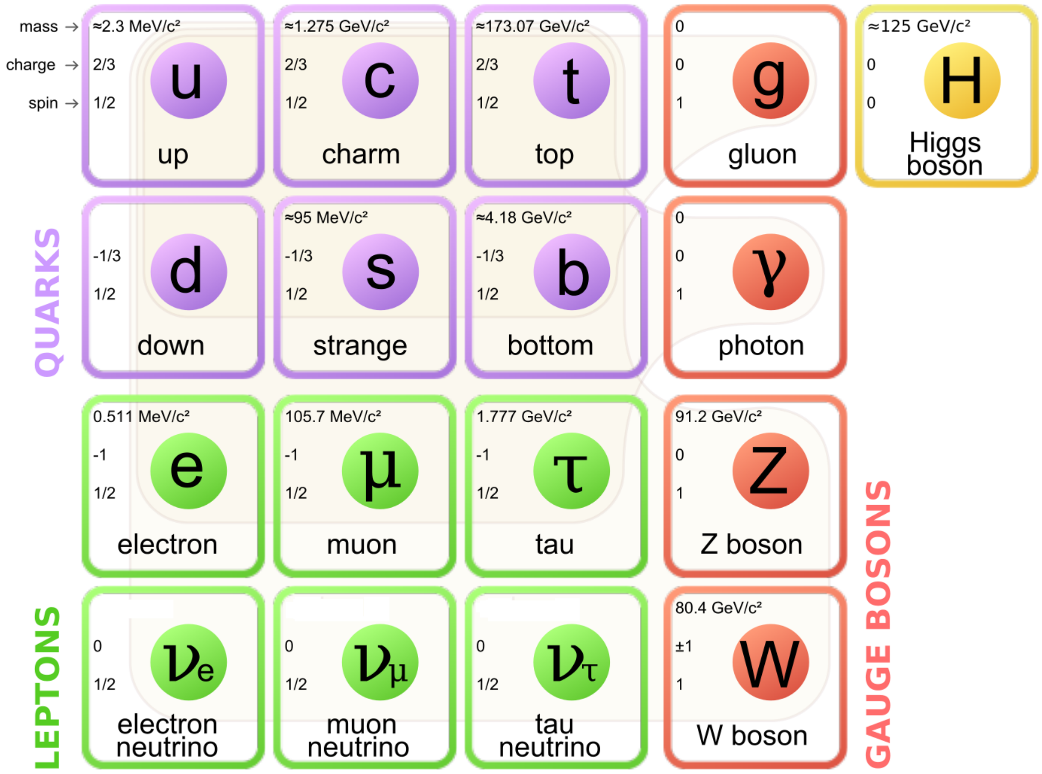

Figure 3.1: *Overview over the particles of the Standard Model. Adapted from [17].*

Interactions and bosons

Interactions are based on the concept of local gauge invariance, where the Lagrangian is invariant under given local group transformations. The group of the Standard Model is $SU(3)_C \otimes SU(2)_L \otimes U(1)_Y$. This can be split into two parts:

- $SU(3)_C$ is the symmetry group of the strong interaction, described by quantum chromodynamics (QCD). Quarks carry a color charge and couple to gluons, the mediators of the strong interaction. As gluons carry a color charge as well, there is also gluon self-coupling.
- $SU(2)_L \otimes U(1)_Y$ corresponds to the electroweak interaction. After symmetry breaking, described in the following section, the observable gauge bosons are the massive W^+, W^-, Z and the massless photon. The electroweak interaction includes couplings to all fermions.

The strength of the interactions can be characterized by dimensionless coupling constants. The constants depend on the energy of the process. At low energies, the coupling constant of the electromagnetic interaction is the fine-structure constant, about $\frac{1}{137}$. The constant increases with increasing energy. The coupling strength of the strong interaction is of the order of 1 for low-energetic processes (about 1 GeV), but decreases towards higher energies, a process called asymptotic freedom. The strength of the weak interaction is between the strength of the other two interactions, and the coupling constant shows only a small energy-dependence.

Gluon self-coupling and the strong coupling of the strong interaction lead to confinement: Quarks and gluons (together refered to as "partons") cannot exist as isolated objects with a color charge, they only exist within hadrons, color-neutral composite objects (quark-gluon plasmas are not discussed here).

Electroweak symmetry breaking

In gauge theories, gauge bosons have to be massless, introducing masses would violate local gauge invariance. Experimental evidence shows that the boson of the weak interaction have mass. The introduction of a new field, the Higgs field, can lead to boson masses without breaking the gauge symmetry. This is called the "Higgs mechanism".

The Higgs field is introduced as SU(2) doublet

$$\phi = \begin{pmatrix} \phi^+ \\ \phi^0 \end{pmatrix}$$

with a Lagrangian density

$$\mathcal{L} = \frac{1}{2} \left(\partial_\mu \phi\right) \left(\partial^\mu \phi\right) - V(\phi)$$

where the potential

$$V(\phi) = \mu^2 \phi^\dagger \phi + \lambda (\phi^\dagger \phi)^2$$

is called "Mexican hat" potential. The parameter λ has to be positive to ensure the potential has a lower bound. If $\mu^2 < 0$, the minimum is not at zero. This leads to a spontaneously broken symmetry, where the vacuum expectation value is at a potential minimum of $\nu = \sqrt{\frac{-\mu^2}{\lambda}}$. The couplings with the vector bosons then lead to their masses: An expansion around the minimum of the Higgs potential leads to the terms equivalent to mass terms for vector bosons but preserving the gauge symmetry of the interactions. Adding a coupling between the Higgs field and the fermion fields leads to masses of the fermions.

One degree of freedom of the Higgs field leads to a scalar boson, the Higgs boson. First theorized in 1964 [18][19][20], it was the last particle of the Standard Model to be discovered. The first observation was made in 2012 independently by the ATLAS [21] and CMS [22] collaborations.

Open questions in the Standard Model

Despite its large success in particle physics, it is known that the Standard Model is not complete, and it has several theoretical and experimental issues:

- The Standard Model does not include gravity. It cannot be used for predictions of very high-energy processes where gravity becomes relevant. This is especially important in the very early universe (the first 10^{-40} seconds), where the energy density was extremely high) and for black holes.
- Cosmological observations show the existence of dark matter [23]. The Standard Model does not have a suitable particle that could correspond to dark matter.
- The uniformity of the cosmic microwave background suggests that the early universe had a phase of exponential expansion ("inflation") [24]. There is no corresponding field in the Standard Model that could lead to inflation.
- The observed matter to antimatter asymmetry in the universe is too large to be explained by known matter-antimatter differences.
- Even without gravity, the Standard Model would not work up to arbitrarily high energies, as the electroweak interaction is not asymptotically free [25]: Couplings increase with increasing energy. This leads to the Landau pole where the coupling strength diverges [26] and the theory is not well-defined any more.
- In perturbation theory, loop corrections to the Higgs mass suggest a very large mass of the Higgs boson, of the order of the Planck scale assuming new physics becomes relevant there. While a small mass is possible, it is considered unlikely [27].
- The Standard Model does not explain the origin of the observed fermion mass hierarchy.

Due to those unsolved issues, modifications and extensions to the Standard Model have been developed, which address at least some of those points. The most notable example is supersymmetry, although it does not include gravity and does not solve all the issues mentioned above. It is discussed in the following section. While the analysis presented in this thesis is not directly sensitive to supersymmetric particles, it studies an important background in searches for supersymmetric particles.

3.2 Supersymmetry

Supersymmetry is based on the introduction of a new symmetry between bosons and fermions. It introduces a superpartner for every particle in the Standard Model: bosons as partners of fermions and fermions as partners of bosons. In addition, the Higgs sector gets extended.

An unbroken supersymmetry would lead to the same masses for particles and their superpartners. This has been ruled out by experiments. Therefore, if supersymmetry exists, it has to be a broken symmetry. The most general approach for symmetry breaking leads to more than 100 free parameters in the theory. Several simplified models have been developed, most notably the "Minimal Supersymmetric Standard Model" (MSSM).

Supersymmetry with particle masses not too much above the mass of the Higgs boson can solve two of the problems mentioned above. Loop corrections to the Higgs boson mass coming from supersymmetric particles would cancel the loop corrections coming from Standard Model particles, leading to a smaller Higgs mass compatible with the experimental result. In addition, the lightest supersymmetric particle can be stable or at least long-living. If it is neutral, it is a candidate for the observed dark matter.

Supersymmetric particles would influence the energy-dependence of the interaction strengths. If they have masses accessible at the LHC, they can lead to all three coupling strengths meeting at a single point at about 10^{16} GeV, leading to approaches to unify the strong and the electroweak interaction.

Searches for supersymmetric particles and the measurement of the mass of the discovered Higgs boson have constrained the possible parameter space for supersymmetry significantly [28].

3.3 Theoretical predictions

To test the Standard Model, it is important to evaluate its predictions for the processes in collisions. As this not possible exactly, different approximation methods have been developed. If the coupling constant is much smaller than 1, perturbation theory is the most successful approach. The interaction is modeled as small deviation from a coupling strength of 0, similar to a Taylor series. Calculations are then performed for each power of the coupling constant separately. The lowest possible order of a process is called "leading order" (LO), the following one is called "next-to-leading order" (NLO), higher orders are called "next-to-next-to-leading order" (NNLO) and so on. Higher orders lead to more accurate predictions, but they are harder to evaluate. For interactions with a coupling constant of the order of 1, perturbation theory does not work. This is important for QCD at low energies. Lattice calculations can be used in these cases [29], they are not discussed here.

If the final state of the calculation (the "hard interaction") involves partons, they are produced as isolated objects in perturbative calculations. This state is unphysical, however, as free partons do not exist. Quarks can emit additional gluons, and gluons can split into quark-antiquark pairs. This parton showering can repeat until all partons form hadrons in a process called hadronization. These hadrons are typically grouped around the directions of the initial high-energetic partons, and considered together as “jets“. As hadronization happens at low energies, the strong interaction is strong, and perturbation theory cannot describe this step accurately. The transition from the hard interaction to separated hadrons is one of the leading contributions to the uncertainties of theoretical predictions. Another source of uncertainty in proton-proton collisions comes from the initial state, described with parton distribution functions (PDFs), describing the effective momentum distributions of partons of different types in the proton.

Two different approaches are followed for predictions used in this thesis.

- Fixed-order calculations focus on the hard interaction, they do not include parton showering or hadronization. It is assumed that every parton of sufficient energy produces a jet. The GoSam [30] calculation used in this thesis evaluates the production of two photons and one or two jets at NLO.
- Monte Carlo (MC) generators include parton showering and hadronization, but their calculation is typically at a lower order. Two MC generators with LO predictions are studied. Sherpa [31] produces two photons and up to three jets in the hard interaction, while Pythia [32] only produces two photons, jets have to come from the parton showering process.

Uncertainties coming from the choice of the PDFs could not be evaluated, as the predictions are available with a fixed PDF set only. Uncertainties from the choice of the energy scale between perturbative and non-perturbative description are evaluated for GoSam, the uncertainties for Sherpa and Pythia have not been evaluated yet. Fixed-order calculations can be improved with non-perturbative corrections [33], these are typically of the order of a few percent. They are still under study for GoSam.

Multiple processes contribute to the production of two photons. The dominant processes are shown in figure 3.2. A box diagram involving only gluons in the initial state, shown in figure 3.3, is possible as well. Additional jets can come from gluon emission or quark splitting, leading to a large number of production processes that have to be considered in the predictions.

3.4 Measurements with the ATLAS detector

The ATLAS detector covers a wide range of particle physics measurements using proton-proton, proton-lead and lead-lead collisions at the LHC. An overview over the ATLAS physics program for can be found in [34]. It can be grouped into multiple topics:

- Measurements of properties of the discovered Higgs boson and searches for additional particles with similar properties
- Measurements of the top-quark

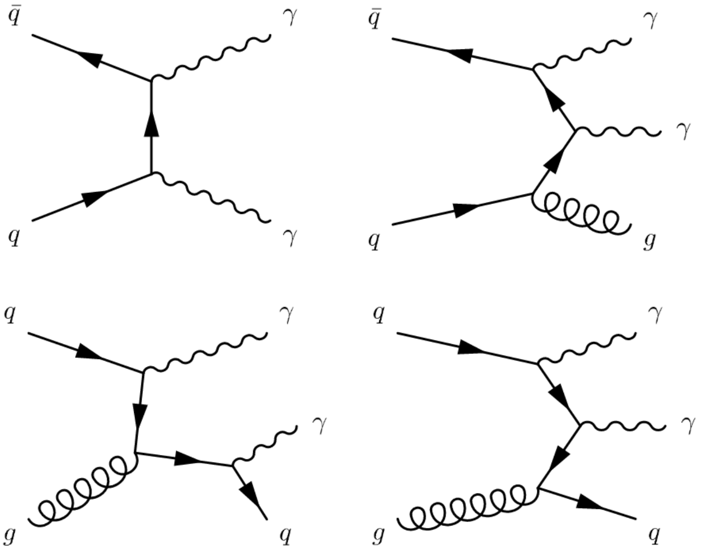

Figure 3.2: *Leading-order processes with two photons in the final state. Quark-antiquark annihilation producing two photons (upper left) or two photons plus one gluon (upper right), and interactions between quark and gluon (lower two diagrams).*

- Measurements of other heavy quarks (bottom and charm)
- Measurements of electroweak physics
- Measurements concerning the strong and electromagnetic interaction
- Searches for supersymmetry
- Searches for other physics beyond the Standard Model.
- Studies of heavy ion collisions.

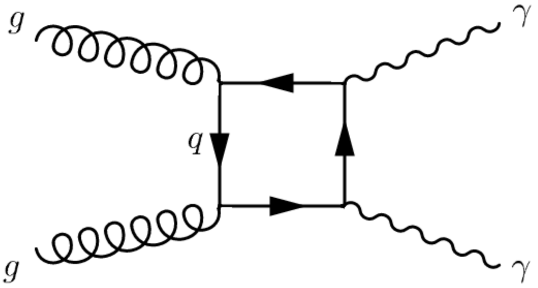

Figure 3.3: *Photon production from gluon annihilation.*

Measurements of the Higgs boson and the strong and electroweak interaction are briefly discussed here.

3.4.1 Higgs boson

The search for the Higgs boson was one of the main goals of the ATLAS experiment. After the discovery of a Higgs-like boson in 2012 [21], measurements of its properties became a major priority. This includes a precise mass measurement, measurements of its production modes and decay channels to determine its couplings, and a determination of spin and parity. With increasing statistics, differential cross section measurements get interesting. Higgs self-interaction provides a method to determine the Higgs potential in more detail.

Multiple decay modes of the Higgs boson are studied. The decay to two photons plays a crucial role in the Higgs measurements. While the branching fraction is small, the decay allows a reconstruction of the Higgs mass, the background from other processes is smooth in the invariant mass spectrum and the signal to background ratio is sufficient to study the Higgs boson.

There are also searches for additional Higgs-like particles, especially particles of the Higgs sector predicted by supersymmetry. A list of all publications can be found at [35].

3.4.2 Strong and electroweak interaction

As the LHC is a hadron collider, the strong interaction participates in nearly all collisions. This makes particles produced by this interaction an important background in every search for new physics and all measurements of Standard Model particles. A good understanding of the strong interaction is therefore crucial. The ATLAS collaboration has a large collection of measurements of strong processes: the total inelastic cross section, charged-particle multiplicities and other track-based observables, cross sections of jets, production of light mesons, angular correlations between particles and various other studies. All publications are listed at [36].

A complementary approach is the study of photon production. Photons couple to quarks, but not to gluons, and they do not participate in hadronization, leading to a more direct access to the hard processes. Studying final states with photons allows measurements of processes involving quarks. In addition, there are final states where gluons in the initial state dominate. Therefore, measurements of photon cross section can be sensitive to quark and gluon PDFs separately.

The ATLAS collaboration measured the differential cross section of single photons [37][38] and single photons with a jet [39][40]. Studying events with two photons gives access to a larger range of observables. A measurement of events with two photons at a center-of-mass energy of 7 TeV has been performed [41], a measurement using 8 TeV collisions is currently in preparation [42]. Studying events with two photons and additional jets continues this program and leads to more observables where the accuracy of theoretical descriptions can be tested. A measurement of this final state is presented in this thesis. In addition to testing the Standard Model, those measurements also provide insights into the background contributions for measurements of the Higgs boson. See chapter 5 for a more detailed discussion.

Chapter 4

Object reconstruction and identification

In order to analyze the collision data, the events have to be collected and the involved particles have to be reconstructed and identified. This chapter is limited to systems and objects relevant for the analysis presented, a more general discussion can be found in [3].

4.1 Trigger system

At the nominal LHC bunch collision frequency of 40 MHz, the produced data rate is too large to be fully read out, and too large to be fully analyzed by current computer systems. A trigger system, consisting of multiple stages, rejects most events and reduces the event rate to a manageable rate, 300 to 600 Hz in 2012 and about 1 kHz in 2015 and 2016 [43].

The first stage of the trigger system ("L1") is implemented in dedicated hardware. It uses partial information from the muon system and data from the calorimeter system at a reduced granularity. Muons are reconstructed based on the muon chambers only. Several individual algorithms ("trigger lines") look for signatures of interesting events, all above given energy thresholds:

- Muons;
- Clusters of energy deposition in the calorimeter: regions of adjacent cells where the summed energy exceeds the thresholds;
- Missing transverse energy: The transverse components of the momenta of all energy depositions in the calorimeter are summed, an imbalance is an indication of neutrinos or other particles which escaped the detector;
- Combinations of these signals.

This approach retains many hard proton-proton collisions, but filters out most of the soft collisions. The event rate is reduced to about 100 kHz. If an event is kept, the whole detector is read out, and all data are passed on to the "L2" trigger stage.

The L2 stage of the trigger system performs a fast partial event reconstruction. It investigates the L1 decision using the full granularity of the detector. It also includes information from the inner detector, which is not available at the L1 stage. This is important in order to be able to distinguish electrons from photons, for example, as their signatures in the calorimeter look very similar. Events that pass the L2 trigger are passed on to the "event filter".

The event filter performs a full event reconstruction and applies tighter selection criteria than the previous steps. Events that pass the event filter are permanently stored for analysis. They are processed again later ("offline reconstruction") with a similar reconstruction, but using more refined algorithms that would be too time-consuming for the trigger system.

For Run 2, starting in 2015, L2 and event filter were merged to a single trigger stage [43].

4.2 Track reconstruction

The inner detector is specialized on the detection and momentum measurement of charged particles. The nominal track-finding algorithm starts with seeds formed from the pixel detector and the strip detector. The seed tracks are then extended outwards, and matching hits in the remaining strip detector are added. A fit to this extended track is again extended outwards to the TRT. After adding matching hits in the TRT, a full track fit is performed.

Long-living particles and photon conversions in the inner detector can lead to tracks that do not start in the pixel detector. Those tracks are not found by the previous method. Track segments in the TRT are produced based on TRT hits not yet associated to tracks. The track segments are extended inwards, matching hits in the silicon detectors are added, and a track fit is performed based on all hits associated to the tracks.

Photon conversion in the inner detector lead to two tracks starting at the same point and going in the same direction. A dedicated algorithm searches for this signature. Another algorithm searches for secondary vertices in general to find decays of long-living particles.

4.3 Jet reconstruction

Quarks and gluons produced in interactions hadronize, typically forming jets made out of many hadrons. Their momenta have to be added to study the initial interaction. The energy of jets is measured in the calorimeters. To define the region in the calorimeter corresponding to a jet ("cluster"), ATLAS uses either the "cone" or the (anti-)k_t algorithm [44]. In this thesis, only the anti-k_t algorithm with radius parameter $R = 0.4$ is used.

Not the whole energy of a jet is deposited in the calorimeter, and the ATLAS sampling calorimeters cannot measure the energy deposited in the absorber. The energy of a jet is calculated as weighted sum of the energies recorded in the individual calorimeter cells in the cluster, where the weights are optimized to reduce the average deviation between reconstructed and true energy in simulations. The calibration is verified on data using decays of particles with known masses like pions. The momentum balance in events with a photon and a jet provides a comparison of purely electromagnetic showers with mainly hadronic showers, and events with two jets allow a comparison of the jet energy calibration in different regions of the detector [45].

4.4 Photon reconstruction and identification

Photons play an important role in the physics program of ATLAS, see section 3. As an example, they played a key role in the discovery of the Higgs boson [21][22]. Photons are also an important tool to check theoretical calculations based on the Standard Model and to measure parton distribution functions of the proton (see section 5). A very efficient and selective photon identification is therefore crucial for the ATLAS physics program.

Photons are reconstructed and selected both in the trigger system and in the offline processing step later.

4.4.1 Photon reconstruction

Photon and electron candidates are first reconstructed based on energy clusters in the electromagnetic calorimeter, where these particles deposit most of their energy in the form of electromagnetic showers [46]. These showers are typically larger than a single calorimeter cell. A sliding-window algorithm with a window size of 3×5 cells in η-ϕ range is used to search for clusters.

Photons can convert to electron-positron pairs in the inner detector. Therefore, converted photons will lead to two charged particle tracks starting at the conversion points. After selecting energy clusters in the calorimeter, tracking information is used to distinguish between unconverted photons, converted photons and electrons. Tracks in the inner detector are considered if their extrapolation to the calorimeter matches the position of the calorimeter cluster. Objects without a matching track are classified as unconverted photon candidates, objects with at least one associated track starting in the inner detector are treated as converted photon candidates. Objects with a track compatible with an electron are considered as electrons. As the origin of a track cannot be determined with 100 %

accuracy, some candidates get classified both as potential converted photon and as potential electron. The difference between converted and unconverted photons is not considered in the trigger as photon conversions are not reconstructed there.

The energy of photon candidates is then estimated as function of the measured energy deposition in the different calorimeter layers. In the second layer, the final cluster size is 3x7 cells for converted photons in the barrel, 3x5 for unconverted photons in the barrel calorimeter, and 5x5 for both converted and unconverted photons in the endcap calorimeter. The calibration is based on simulation and measurements of decays of Z and J/Ψ to electron-positron pairs, as those decays lead to prominent invariant mass peaks of known energies. More details can be found in [47].

4.4.2 Photon isolation

Photons can be produced directly in the hard interaction, emitted by quarks later ("fragmentation photons") or produced in the decays of hadrons. Typically analyses are interested in the first category only. To discriminate between these categories, the energy deposition in the calorimeter close to the photon is studied. The separation between different objects in the calorimeter can be expressed as

$$\Delta R = \sqrt{(\eta_1 - \eta_2)^2 + (\phi_1 - \phi_2)^2}. \tag{4.1}$$

The reconstruction provides information about energy deposition in a $\Delta R < 0.4$ cone around the central photon position. Similar to transverse momentum, a "transverse energy" can be calculated, neglecting the mass of particles in the calorimeter. The total transverse energy in all topological clusters within a $\Delta\ R\ <\ 0.4$ cone around the photon is called "isolation energy" E_T^{isol}. This is described in more detail in [48]. The isolation energy is typically small for photons from the hard interaction, but larger for fragmentation photons and photons from hadron decays, therefore it can be used to distinguish between those categories. The isolation energy is larger for jets as well, providing separation power in addition to the photon identification discussed in the following section.

Energy deposition in the calorimeter can also come from pileup collision. This contribution does not contain information about the origin of the photons. Its expected contribution is calculated and removed based on the overall activity in the detector.

While a 5x7 window of calorimeter cells covering the photon is not included in the calculation of the isolation energy, a small fraction of the photon energy (typically 2% to 4%) can be found outside. The average leakage is measured in events containing a single photon and no other activity in the detector and subtracted from the measured isolation energy [49].

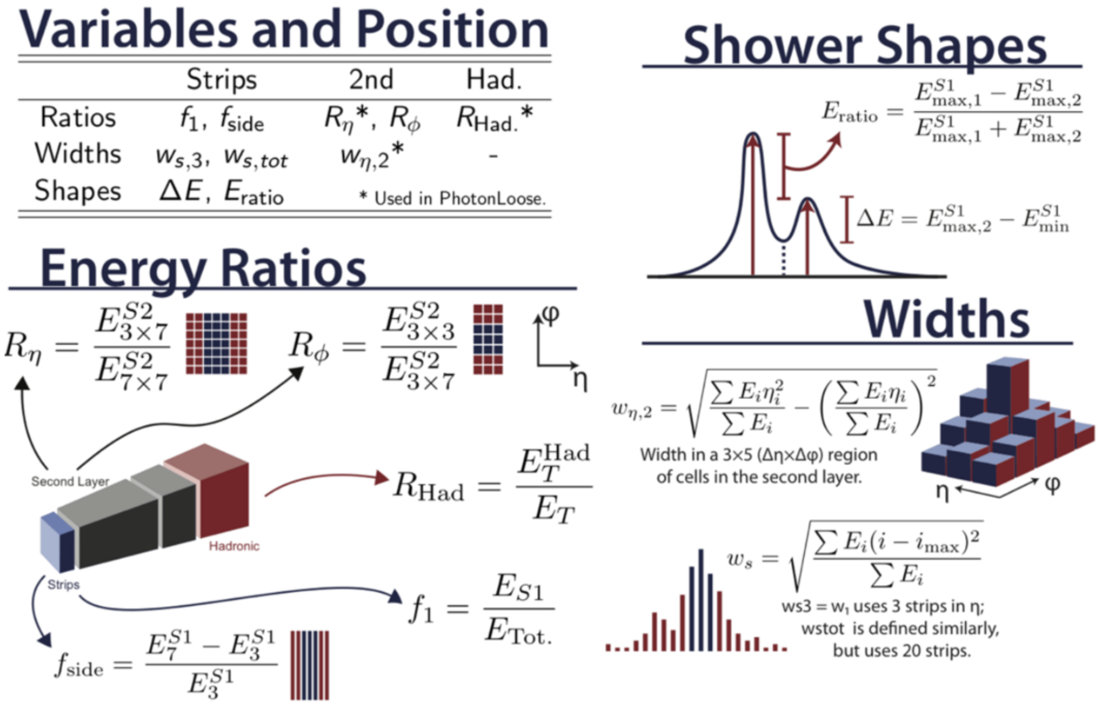

Figure 4.1: *Illustration of shower shapes used in the photon identification. Taken from [50].*

4.4.3 Photon identification

Photon identification in ATLAS relies on nine parameters, called “shower shapes”, that are calculated for each reconstructed photon. They describe different aspects of the shape of the photon shower in the calorimeter. The shower shapes are shown in figure 4.1 and listed in table 4.1. The same set of shower shapes is used in the trigger and the offline photon identification.

The shower shapes are chosen to maximize the discrimination power between actual photons and jets that are falsely reconstructed as photons. A false reconstruction can happen in jets where a single π^0 contains most of the energy of the jet. High-energy pions decay into a pair of collimated photons, producing two showers close together in the calorimeter. The first layer of the electromagnetic calorimeter is finely segmented to resolve the two showers.

Three different sets of selection criteria exist, called “loose”, “medium” and “tight”, in order of increasing background rejection and decreasing photon efficiency. The “loose” selection uses R_η, $w_{\eta 2}$ and R_{had}, these variables are based on the shower width in the second calorimeter layer and the fraction of energy deposited in the hadronic calorimeter. The “medium” selection (only used in the trigger) uses E_{ratio} in addition, the “tight” selection uses all nine parameters. Apart from R_ϕ, all additional shower shapes are sensitive to the substructure of the shower in the first layer.

Shower shape	Definition
R_{had}	Ratio of E_T in the whole hadronic calorimeter to E_T of the cluster in the electromagnetic calorimeter. This variable is used in the region $0.8 < \lvert\eta\rvert < 1.37$.
$R_{\text{had},1}$	Ratio of E_T in the first layer of the hadronic calorimeter to E_T of the cluster in the electromagnetic calorimeter. This variable is used for $\lvert\eta\rvert < 0.8$ and $1.52 < \lvert\eta\rvert$. R_{had} is used as symbol for both if the η range is not specified.
R_η	Ratio in η of cell energies in 3×7 to 7×7 cells in the second calorimeter layer.
R_ϕ	Ratio in ϕ of cell energies in 3×3 to 3×7 cells in the second calorimeter layer.
$w_{\eta2}$	Shower width in η in a 3×5 region in the second calorimeter layer.
$w_{s,3}$	Shower width in η in 3 strips in the first calorimeter layer.
$w_{\text{s,tot}}$	Shower width in η in 20 strips in the first calorimeter layer.
f_{side}	Ratio in η of energies in 3 to 7 strips in the first calorimeter layer.
ΔE	In the first calorimeter layer, difference between the energy of a second local maximum and the minimum strip energy between this local maximum and the global maximum, in MeV.
E_{ratio}	The energy difference between first and second maximum divided by the sum of the two energies.

Table 4.1: *Shower shape variables used in the photon identification [47].*

If a photon converts to an electron/positron pair before reaching the calorimeter, electron and positron have slightly different trajectories due to the magnetic field, and lead to two showers with a very large overlap. In addition, electrons and positrons can emit Bremsstrahlung, which also hits the calorimeter in the same region. While these objects are close enough to get reconstructed as a single shower, this shower tends to be wider. Therefore, the "tight" identification has different selection criteria for unconverted and converted photons.

Photon triggers and identification criteria used

Jets outnumber photons in proton-proton collisions by a factor of more than 1000. The identification has to reduce their contribution in photon analyses to a manageable level. Therefore, the main identification method in the offline identification is "tight". About 80% to 90% of all photons (depending on their energy and pseudorapidity) are correctly identified, while only about one in a few thousand jets is mistakenly identified as "tight" photon.

The number of jets passing the photon identification criteria has to be accounted for in photon analyses, see section 5.3 for an example. To make this feasible, the analyses need control regions with a larger background contribution. Therefore, the main triggers use the "loose" or "medium" identification. A trigger based on the "tight" identification is used only where the background is not of major concern and where the trigger rate would be unacceptable otherwise.

Three main photon triggers were used in Run 1:

- a diphoton trigger where both photons are required to be "medium" and have $E_T > 20$ GeV;
- a diphoton trigger where the photons are required to be "loose" and have $E_T > 35$ GeV and $E_T > 25$ GeV for leading and subleading photon, respectively;
- a single photon trigger requiring $E_T > 120$ GeV for a "loose" photon.

Triggers with a lower threshold or looser identification criteria were used for running conditions with lower luminosity. In addition to the main triggers, several prescaled triggers with lower E_T requirements were implemented, where only a small fraction of all events are kept.

For Run 2, the higher luminosity and collision energy made an increase in trigger thresholds or a change to tighter identification criteria necessary. A trigger using the "tight" photon identification was added. Three main triggers were used until the end of 2016:

- a diphoton trigger where both photons are required to be "tight" and have $E_T > 22$ GeV;
- a diphoton trigger where the photons are required to be "medium" and have $E_T > 35$ GeV and $E_T > 25$ GeV for leading and subleading photon, respectively;
- a single photon trigger requiring $E_T > 140$ GeV for a "loose" photon.

In 2015 and in early 2016, a single photon trigger requiring $E_T > 140$ GeV for a "loose" photon was used without prescaling. It was prescaled when the increasing luminosity made its rate too high.

As the reconstruction differs between the trigger and the offline selection, in general different selection criteria can be used. The selection aims for a high efficiency of the trigger selection with respect to the offline selection (in order to maximize the number of available events), and for high efficiency of the offline selection with respect to the trigger selection (in order to limit the trigger rate).

Influence of operation conditions

The shower shape distributions of both photons and other objects depend on the conditions of the ATLAS detector and the LHC machine operation. The main impact comes from the following parameters:

- In-time pileup: The number of proton-proton collisions per bunch crossing. On average, more collisions lead to more tracks in the inner detector, more energy is deposited in the calorimeter and the energy deposition patterns can get more complex. In general, this leads to wider reconstructed showers. Pileup conditions change every year and even during a year.
- Out-of-time pileup: The time between consecutive bunch crossings went down from 75 ns in 2010 and 2011 to 50 ns in 2011 and 2012 and 25 ns in 2015 and 2016. Pulses in the calorimeter have a length of up to 500 ns (see section 2.4.1), equivalent to many bunch crossings with overlapping signals, where the number of overlapping bunch crossing signals increased over the years. Similar to in-time pileup, this can lead to wider showers.
- The IBL was inserted for Run 2, which changes the material distribution in the inner detector and the tracking performance, this is important for the difference between unconverted and converted photon candidates.
- Due to gas leaks in the TRT, the gas composition was changed from mainly xenon to mainly argon in some segments (plus carbon dioxide and a small amount of oxygen in both cases). This changes the signal gain in the TRT and therefore the particle identification quality and the tracking efficiency, which is important for the reconstruction of converted photons [9].
- The center-of-mass energy increased from 7 (2010 to 2011) and 8 (2012) to 13 TeV in 2015 and 2016. This changes the average energy deposition per event, and also shifts the main focus of some photon-based analyses to higher energies.

Due to these effects, the identification efficiency and the background rejection change if the running conditions change. In order to maintain a high performance, frequent re-optimizations of the identification criteria are necessary. For Run 2, starting in 2015, the identification was changed both in the trigger and in the offline reconstruction. A part of this thesis was the coordination of the trigger and offline identification and the evaluation of efficiency and background rejection for all new selections.

Adjustment of Monte Carlo shower shapes

Photons measured in Run 1 show shower shape distributions different from the predictions from simulations [47]. While the shapes of the distributions agrees,

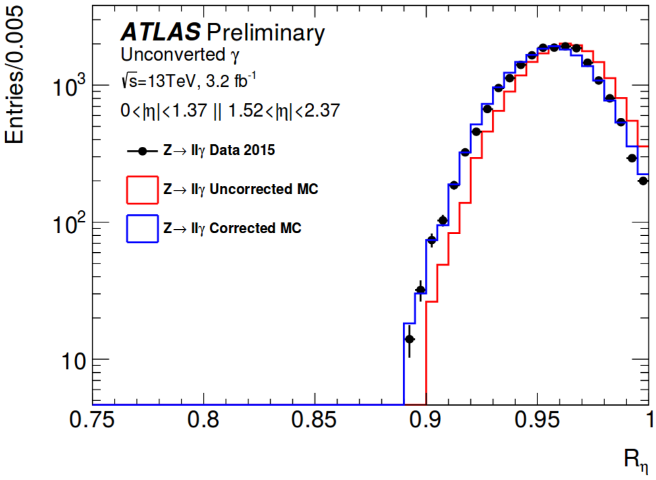

Figure 4.2: *Illustration of the adjustment of Monte Carlo shower shapes using photons from the decays* $Z \to ee\gamma, \mu\mu\gamma$ *to obtain a pure photon sample. Taken from [51].*

the central values show small shifts. The showers in data are wider than simulated, the origin of the discrepancy is not understood. The deviations have been measured as function of η and E_T. All simulated shower shape values for photons are shifted by those measured deviations to improve the accuracy of simulations [51]. An example of this procedure is shown in figure 4.2. As no Run 2 data was available at the time of the optimization of the photon identification for Run 2, the shift values were derived from Run 1 data as described in [47].

4.4.4 Optimization of photon identification

To adapt the photon identification to the conditions of Run 2, Monte Carlo (MC) simulations are produced, either with photons and with jets from a single interaction. Particles from additional interactions (pileup) are simulated with PYTHIA, and added to the simulated events. Different running conditions are simulated — for the optimization, samples with 20 to 40 additional interactions are used as these conditions best match the LHC performance expected in Run 2. The samples contain both the shower shapes of the (simulated) trigger reconstruction and the (simulated) offline reconstruction.

Photon candidates are selected if they pass selection criteria for all shower shapes individually (e. g. "$E_{\text{ratio}} > 0.7$ && $R_\eta > 0.88$ && ..."), as tests with more elaborate selection methods did not show a notable improvement over this procedure [52], and the approach with rectangular cuts leads to more natural control regions used to subtract background from jets (see section 5.3). The nine shower shapes show large correlations, which makes manual tuning inefficient. An example of the distribution of signal and background events in E_{ratio} is shown

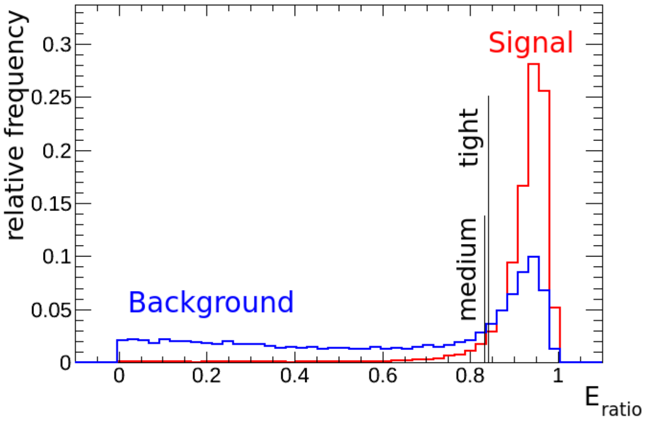

Figure 4.3: *Example of the distribution in* E_{ratio} *for signal (red) and background (blue) events in the pseudorapidity bin 2 in the trigger photon identification. The selection criteria for "medium" and "tight" identification are marked.*

in figure 4.3.

A genetic algorithm implemented in TMVA [53] is used to determine the selection criteria. Half of the simulated data are used as training sample to identify possible selection criteria, the other half are used as validation sample to test the efficiency and background rejection of the chosen criteria. The algorithm produces a set of selection criteria for different identification efficiencies, in steps of 1%, with decreasing background rejection for increasing signal efficiency.

Typically, most analyses use triggers based on the "loose" or "medium" trigger identification, while the "tight" offline identification is used. This determines the focus of the optimization. In addition, a "loose" offline identification is used for control regions in background subtraction methods (see e. g. section 5.3), while the "tight" trigger identification is used for a few dedicated searches at low energy, for example for Higgs-like particles below a mass of 100 GeV, where the high rate of low-energy photon candidate pairs would lead to an unacceptably high trigger rate for a "loose" or "medium" diphoton trigger.

Based on the detector geometry, different regions of the detector have different shapes of the photon showers, mainly due to the η-dependent amount of material in front of the calorimeter but also due to the layout of inner detector and calorimeter. Therefore, the identification is optimized separately in eight bins of absolute pseudorapidity $|\eta|$, following the detector geometry, where each bin has different thresholds for the shower shapes. The bins are listed in table 4.2. The most notable difference occurs between the barrel region and the endcap region. Between the two regions ($1.37 < |\eta| < 1.52$), the first calorimeter with its fine segmentation is missing and detector infrastructure increases the material budget in front of the calorimeter. Therefore, the photon identification is not reliable in this bin, it is excluded in photon analyses. The last bin ($2.37 < |\eta| < 2.47$) is present in the loose and medium selection only. It is not studied further as it does not provide a sufficient discrimination power between signal and background.

Photons close to the boundary between bins can be reconstructed in one bin in the trigger and in a different bin in the offline reconstruction, thus being subject to different selection criteria. This can potentially lead to large discrepancies between the trigger and offline identification. It is verified manually that the selection criteria do not vary too much between the eight bins.

Bin number	0	1	2	3	4	5	6	7
Lower edge $\|\eta\|$	0	0.6	0.8	1.15	1.52	1.81	2.01	2.37
Upper edge $\|\eta\|$	0.6	0.8	1.15	1.37	1.81	2.01	2.37	2.47

Table 4.2: *Bins used for the photon identification. Bins 0 to 3 cover the barrel region, bins 4 to 7 are in the endcap. region.*

As first step, the trigger identification for “medium” is optimized, the “loose” selection is then derived by removing the selection criterion on E_{ratio}. The optimization aims to keep the same average signal efficiencies as in Run 1. The new set of selection criteria is then also used for the “loose” offline identification. As second step, the “tight” offline identification is optimized, independently for converted and unconverted photons. The “tight” offline selection is required to be as least as strict as the parameters of the “medium” trigger selection. As last step, the converted and unconverted offline selection are merged to create the “tight” trigger identification. There is no conversion reconstruction at the trigger level, therefore the trigger needs a single common “tight” menu for all photon candidates. In each bin for each variable, the less restrictive requirement is used. This ensures a high efficiency of the offline selection with respect to trigger events for both converted and unconverted photons. The downside of this procedure is a slightly larger trigger rate as the background rejection deteriorates.

The overall procedure ensures a high performance for the most important trigger and offline selection types, while keeping both as compatible as possible. Loosening the trigger selection with respect to the offline selection has been tested, but found to increase the trigger rates too much even for a small gain in acceptance.

The chosen “medium” selection is shown in table 4.3, the “loose” selection is directly derived from it. The “tight” offline selection criteria are listed in table 4.4 for unconverted and table 4.5 for converted photons. Overall, the identification shows a performance similar to Run 1, but under more challenging conditions, in particular due to the increased pileup.

The identification efficiency of the offline selection has been measured using collision data of 2015 with three different methods [51], the results are shown in figure 4.4 for unconverted photons and figure 4.5 for converted photons.

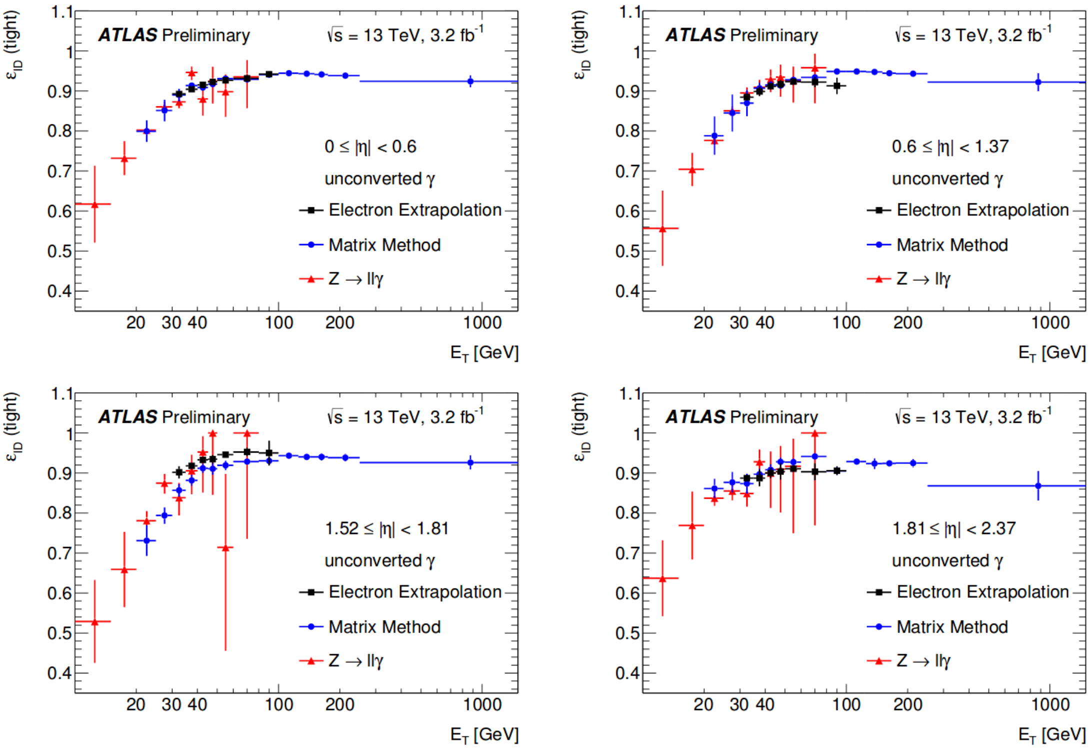

Figure 4.4: *Efficiency of the tight offline selection for unconverted photons, measured with data taken in 2015 [51].*

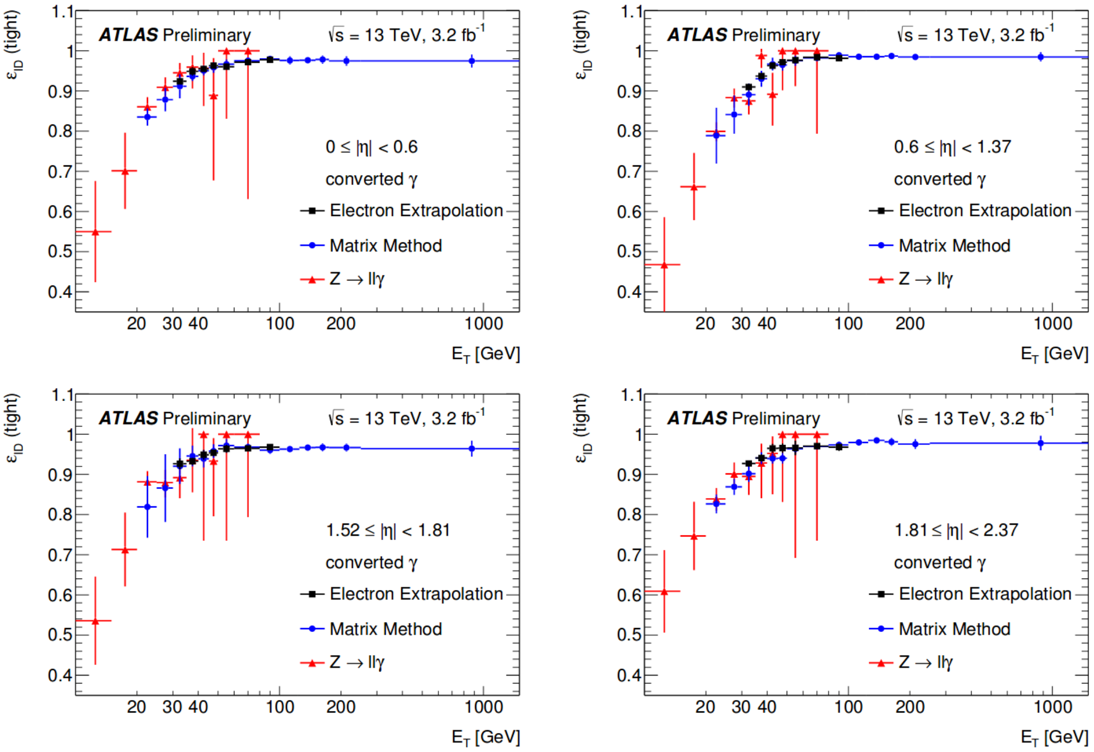

Figure 4.5: *Efficiency of the tight offline selection for converted photons, measured with data taken in 2015 [51].*

The efficiency of the “loose” selection in the trigger and the trigger rates of the three main triggers in 2015 has been evaluated [43], the results are shown in figure 4.6.

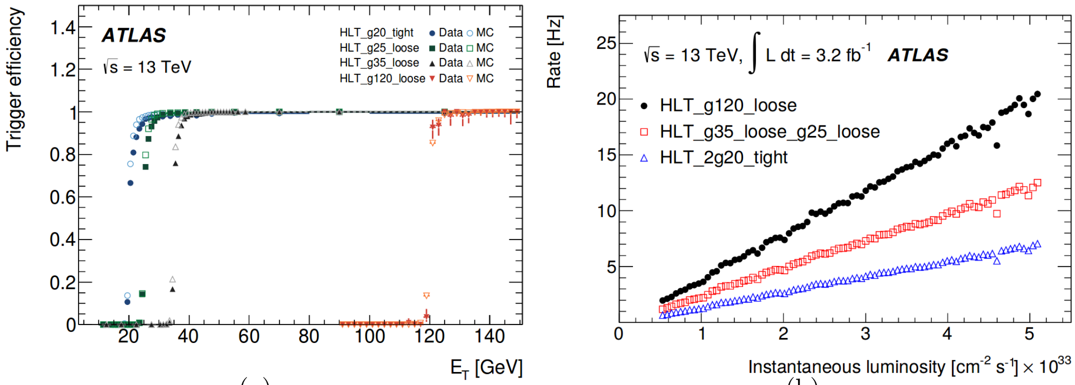

(a) (b)

Figure 4.6: *(a) Trigger efficiency of the “loose” and “tight” selection relative to triggers with lower p_T thresholds. (b) Trigger rates of the main triggers used in 2015 as function of the instantaneous luminosity. Taken from [43]. In 2016, the thresholds of the triggers using “loose” and “tight” photon identification had to be increased.*

Bin number	0	1	2	3
$E_{\text{ratio}} \geq$	0.818435	0.85434	0.832063	0.777831
$R_\eta \geq$	0.917538	0.899968	0.9109	0.891172
$R_{\text{had}} \leq$	0.060612	0.052373	0.064818	0.049078
$w_{\eta 2} \leq$	0.012883	0.014204	0.013615	0.01392
Bin number	4	5	6	7
$E_{\text{ratio}} \geq$	0.837065	0.66645	0.545618	0.76786
$R_\eta \geq$	0.892213	0.922116	0.8903	0.89826
$R_{\text{had}} \leq$	0.047875	0.065063	0.062014	0.040855
$w_{\eta 2} \leq$	0.015245	0.012811	0.012538	0.011836

Table 4.3: *The selection criteria of the medium photon selection. The loose selection is the same but without the requirement on E_{ratio}.*

Bin	0	1	2	3	4	5	6
$\Delta E \leq$	424.846	460.075	90.6112	318.767	504.006	1223.18	1429.46
$E_{\text{ratio}} \geq$	0.847944	0.859798	0.841797	0.821782	0.914389	0.816308	0.585461
$f_{\text{side}} \leq$	0.270098	0.300000	0.403128	0.405609	0.450553	0.237674	0.229234
$R_{\eta} \geq$	0.929292	0.917085	0.920179	0.920034	0.905937	0.927159	0.902958
$R_{\text{had}} \leq$	0.058252	0.051286	0.063215	0.046673	0.044622	0.062716	0.058965
$R_{\phi} \geq$	0.947540	0.932142	0.942694	0.932631	0.93614	0.946772	0.938363
$w_{s,3} \leq$	0.652157	0.779928	0.715151	0.709702	0.745094	0.749026	0.612900
$w_{\eta 2} \leq$	0.011568	0.011963	0.010655	0.011414	0.013209	0.012811	0.012389
$w_{\text{s,tot}} \leq$	2.40322	2.43473	2.81964	2.93974	4.38172	3.62645	1.92694

Table 4.4: *The selection criteria of the tight unconverted photon selection.*

Bin	0	1	2	3	4	5	6
$\Delta E \leq$	124.327	194.579	397.057	241.591	402.416	864.100	826.424
$E_{\text{ratio}} \geq$	0.880184	0.934769	0.887953	0.830081	0.895005	0.897472	0.911688
$f_{\text{side}} \geq$	0.331333	0.395052	0.489296	0.495897	0.556787	0.307892	0.227579
$R_{\eta} \geq$	0.918031	0.902213	0.913792	0.894571	0.896146	0.926236	0.894269
$R_{\text{had}} \leq$	0.058252	0.051286	0.063215	0.046673	0.044622	0.062716	0.058965
$R_{\phi} \leq$	0.486405	0.523354	0.585838	0.666968	0.719156	0.739003	0.851791
$w_{s,3} \leq$	0.682122	0.752878	0.752067	0.748778	0.814085	0.719463	0.650652
$w_{\eta 2} \leq$	0.010600	0.011229	0.011451	0.011723	0.012792	0.011693	0.012485
$w_{\text{s,tot}} \leq$	2.38262	3.31293	3.06913	3.01992	3.86382	2.26193	2.85561

Table 4.5: *The selection criteria of the tight converted photon selection.*

Chapter 5

Measurement of differential cross-sections in events with two isolated prompt photons and jets

5.1 Introduction

Many different final states can be used to probe Standard Model processes and the accuracy of their theoretical predictions. Photons cannot be radiated from gluons, therefore they are always connected to processes involving quarks or leptons, but the latter contribution is small. In addition, they do not interact via the strong interaction: unlike in measurements of jets it is possible to directly test the products of the hard interaction. This makes them an excellent tool to study processes of the strong interaction. Many production processes for photons also involve jets in the final state, measuring them together with the photons increases the range of phenomena that can be studied. In addition, other analyses, in particular measurements of the Higgs boson decaying to two photons, have events with two photons (not coming from a Higgs boson decay) as dominant background contribution. Improving the understanding of events with two photons and jets helps to study the Higgs boson properties as it can guide the development of background descriptions.

This thesis presents the measurement of differential cross sections for diphoton plus jet production in proton-proton collisions at a center-of-mass energy of $\sqrt{s} = 8$ TeV. Only prompt isolated photons are considered, photons originating from hadron decays are excluded. 20.25 ± 0.38 fb^{-1} ($\pm 1.9\%$) collected with the ATLAS detector in 2012 are analyzed. The average number of interactions per bunch crossing was 20.7. The measurements are done double differentially in 16 different observables and the number of jets, where the jet categories are “0 jets”, “1 jet”, “2 jets” and “at least 3 jets”. The jet categories “$\geq$0 jets”, “$\geq$1 jet” and “$\geq$2 jets” are derived from those measurements. The observables and their binning are introduced in section 5.2.5.

Several different theory groups published next-to-leading order (NLO) predictions for the production of two photons in association with jets ([54] to [57]). A comparison of the predictions to the experimental results allows an improvement of the understanding of QCD processes.

5.1.1 Previous measurements

Diphoton production cross sections have been measured by several experiments before, but only one previous study also included jets.

At the Tevatron, using proton-antiproton collisions at a center-of-mass energy of $\sqrt{s} = 1.96$ TeV, the CDF collaboration studied the diphoton cross section based on an integrated luminosity of 9.5 fb^{-1} [58], while the DØ collaboration released two publications based on 4.2 fb^{-1} [59] and 8.5 fb^{-1} [60], respectively.

At the LHC, using proton-proton collisions, the ATLAS collaboration analyzed diphoton cross sections using 37 pb^{-1} [61] and later 4.9 fb^{-1} [41] at $\sqrt{s} = 7$ TeV, an analysis of the $\sqrt{s} = 8$ TeV dataset is in the publication process [42].

The CMS collaboration studied diphoton cross sections based on 36 pb^{-1} [62] and 5.0 fb^{-1} [63]. Preliminary results on diphoton and jet cross sections have been released [64]. All CMS measurements are based on $\sqrt{s} = 7$ TeV collisions.

5.1.2 Overview of the analysis

The outline of this chapter follows the steps of the analysis: The studied data samples and event selection are shown in section 5.2. The fiducial phase space and the 16 studied observables are also introduced in this section. The choice of the studied phase space mainly follows experimental constraints in the subtraction of background contributions. Sections 5.3 and 5.4 present two different methods to subtract backgrounds from jets faking photons. This is the main background in the analysis. Both methods use control regions where the photon identification is loosened or the photon isolation selection is inverted, which allows to estimate the background contribution in the signal region. Section 5.5 presents a method to subtract events where electrons are reconstructed as photons. It is based on the Z-peak visible in the diphoton and photon plus electron invariant mass spectrum, where one or both electrons are misreconstructed as photons. This background contribution is much smaller than the contribution from jets. The very small contribution of Higgs decays is briefly discussed in section 5.6. The efficiency of the event selection and bin migration are described in section 5.7. The background-subtracted yields are unfolded with a modified version of SVD unfolding, shown in section 5.8. Systematic uncertainties are presented in section 5.9. The main contributions come from the jet background subtraction for photons and from the jet energy scale uncertainty for jets. Finally, the results and a comparison

Selection	Number of events
Trigger	27,882,247
All subsystems working	26,566,873
Primary vertex with ≥ 3 tracks	26,566,672
Two reconstructed photons	19,767,185

Table 5.1: *The number of events in the sample after the first selection steps.*

to Sherpa predictions are shown in section 5.10. While some variables show a good agreement, other variables reveal notable deviations.

My contributions to the analysis was to apply the 2x2DSB jet background subtraction method and to study its accuracy, to develop the new unfolding method and to use it in the analysis, to evaluate all systematic uncertainties (apart from those from the second jet background subtraction method) and to put everything together for the results, which I then compared to the Sherpa, Pythia and GoSam predictions.

5.2 Data samples, object and event selection

The fiducial phase space studied in the analysis is driven by the geometric acceptance of the ATLAS detector components, the requirement of a good identification of the studied objects to suppress background, and the available photon triggers.

5.2.1 Data samples

For the analyzed data sample, events are required to be selected by the trigger "2g20vh_medium", which requires two photons with "medium" identification criteria (see section 4.4) and at least 20 GeV transverse momentum each. The efficiency of this trigger was measured as $98.66\%^{+0.14\%}_{-0.16\%}(\text{stat}) \pm 0.10\%(\text{syst})$ [66]. Triggered events go through a more refined offline reconstruction afterwards. Events are required to have at least one primary vertex with at least three reconstructed tracks. It is also required that two photons are reconstructed in those events, again with at least 20 GeV transverse momentum: Due to differences in the trigger and offline reconstruction, photons can be reconstructed with a transverse momentum slightly above 20 GeV in the trigger but slightly below this value in the offline reconstruction.

Events collected at times where not all subsystems of ATLAS were working properly are removed. This affects about 4.5% of the full dataset, the given luminosity value takes this removal into account [67].

Event numbers for the different selection steps are shown in table 5.1.

5.2.2 Simulated event samples

While the analysis relies on data-driven measurements as much as possible, Monte Carlo simulations are crucial for all cross section measurements as not every effect can be evaluated purely based on data samples.

Simulations start with the hard process, where the production of two photons is simulated, possibly with additional partons in the final state. Afterwards parton showers and hadronization are simulated. This is done with two different programs, both leading order Monte Carlo generators:

- The default simulation uses SHERPA [31] with CT10 PDFs [68]. Events in the sample have two photons and up three jets from the hard process, additional jets can come from parton showers. The sample was generated in two slices of the diphoton invariant mass, from 55 GeV to 80 GeV and above 80 GeV.
- Another simulation uses PYTHIA [32] with LO CTEQ6L1 PDFs [69]. Events always have two photons from the hard process, jets can arise from parton showers only. As this underestimates the number and the transverse momenta of jets, PYTHIA is used for comparison only. Generated photons are required to have $p_T^\gamma > 20$ GeV. PYTHIA is also used for a sample of $Z \to ee$ decays to estimate the background from electrons.

The decays of simulated particles and their interactions with the ATLAS detector are then simulated with GEANT4 [70]. The size of the simulated SHERPA samples corresponds to an integrated luminosity of about 500 fb^{-1}, a factor 25 larger than the experimental dataset.

Particles from additional collisions in a bunch crossing (pile-up) are added in order to match experimental conditions as closely as possible.

5.2.3 Photon reconstruction and selection

The initial photon reconstruction, described in section 4.4.1, leads to estimates for the total energy of the photon candidate (referred to as "photon" in this section) E. The pseudorapidity is estimated based on the second layer of the calorimeter, η_{S2}. This allows to calculate an initial estimate for the transverse momentum of the photon:

$$p_{T,S2} = \frac{E}{\cosh(\eta_{S2})} \tag{5.1}$$

Only photons with $p_{T,S2} > 20$ GeV are considered. They are required to be either in the region $|\eta_{S2}| < 1.37$ or $1.56 < |\eta_{S2}| < 2.37$, where the excluded region in the middle is the transition region between barrel and endcap calorimeter, where the photon identification is not selective enough to suppress the background from jets. Photons are required to pass the "loose" identification criteria (see section 4.4).

All photons passing this initial preselection are ordered by their transverse momentum, only the two photons with the largest transverse momentum are kept. η_{S2} is calculated assuming that the photons come from the nominal collision point of z=0 (see chapter 2 for a definition). The finite size of the interaction region leads to deviations from this. The primary vertex that produced the two photons is determined with the photon pointing method as discussed in [21]. The method uses the estimated photon direction from calorimeter data, the parameters of the beam spot and the summed squared transverse momenta of the tracks associated with each vertex. The pseudorapidity η is recomputed using the z-position of the estimated production vertex. p_T is computed using the new pseudorapidity value. The photon with the larger transverse momentum is called “leading” photon, while the other photon is called “subleading” photon.

Both photons are then required to have $p_T > 22$ GeV. The 2 GeV increase relative to the trigger requirements and the preselection ensures a high efficiency of the previous selection steps and leads to a high overall efficiency. The analysis studies the diphoton production in bins of the number of jets. In the 0-jet category, symmetric p_T requirements can lead to large uncertainties in next-to-leading order (NLO) calculations due to infrared divergences. This is described in detail in [71]. Typically diphoton analyses choose asymmetric p_T thresholds for their two photons to avoid the large uncertainties arising from those divergences. This analysis has its focus on the categories with jets where those uncertainties do not arise. Asymmetric p_T criteria would reduce the sample size and increase statistical uncertainties in the jet categories. It has been decided to use a symmetric selection in order to maximize the sensitivity in the categories with jets.

The invariant mass $m_{\gamma\gamma}$ of the two photons is calculated, and $m_{\gamma\gamma} > 60$ GeV is required. This is necessary due to the limited $m_{\gamma\gamma}$ range ($m_{\gamma\gamma} > 55$ GeV) of the SHERPA sample, as this sample is used for unfolding (see section 5.8).

For the signal region, both photons are required to pass the “tight” identification criteria (see section 4.4). This suppresses most of the background from jets identified as photons. Events where at least one of the photons does not pass them, but still passes the “loose” criteria, are used to subtract the remaining background, as discussed in section 5.3.

As discussed in section 4.4.2, the photon reconstruction calculates the isolation energy of photons within $\Delta R < 0.4$. Jets typically have a larger isolation energy than photons. Both photons are required to have $E_T^{\text{isol}} < 4$ GeV to suppress the contribution from jets. A minimal separation of $\Delta R_{\gamma\gamma} > 0.4$ between the central photon positions is required to avoid having a photon within the isolation cone of the other photon.

5.2.4 Jet reconstruction and selection

Jets are reconstructed with the anti-k_t algorithm with parameter R=0.4, as described in section 4.3. They are required to have a pseudorapidity of $|\eta| < 4.4$

and a minimal transverse momentum of $p_T > 25$ GeV. Jets within the isolation cone of one of the two photons ($\Delta R < 0.4$) are discarded to avoid selecting the photons again as jets.

For jets with 25 GeV $< p_T <$ 50 GeV and $|\eta| < 2.4$, the Jet Vertex Fraction [72] (JVF) is evaluated. The transverse momenta of all tracks from the diphoton production vertex associated with the jet are summed. The same calculation is repeated without considering the production vertex. The JVF is then defined as the first sum divided by the second sum. A larger JVF corresponds to more high-energetic tracks coming from the diphoton production vertex. The JVF value is an estimate if the jet is from the same primary vertex as the two photons. It is used to suppress pileup, which is important for low-energetic jets. Jets with a JVF below 0.5 are removed. For jets with 25 GeV $< p_T <$ 50 GeV and $2.4 \leq |\eta| < 4.4$, the missing tracking information does not allow to compute the JVF. Using these jets would include too many selected pileup jets. Therefore, all those jets are removed. This selection leads to about 80% of the selected jets coming from the correct primary vertex at $|\eta| = 2.4$, and an average of about 90%.

Jets are less collimated than photons. Even with a separation a bit above $\Delta R = 0.4$, the jets influence the isolation value of the photon and reduce the isolation selection efficiency. As this effect is not well described in simulations, events are removed completely if any jet that passes the full selection described above is closer than $\Delta R = 0.6$ to a photon.

5.2.5 Studied observables and binning

The cross section is measured in bins of the 16 observables listed in table 5.2.

- 4 observables depend on the photon kinematics only, they follow previous photon analyses: Invariant mass and transverse momentum of the diphoton system, the cosine of the angle θ in the Collins-Soper frame [65], and the azimuthal angle difference between the photons.
- 4 observables depend on the leading and subleading jet. Instead of the angle in the Collins-Soper frame the difference in rapidity is used, the other three observables are equivalent to the diphoton observables.
- 4 observables describe the distance between leading (subleading) photon and leading (subleading) jet.
- 1 observable is the difference in azimuthal angle between the diphoton and the dijet system.
- 3 observables measure the transverse momenta of the jets.

The binning used in this analysis is shown in table 5.3. The bin widths were chosen based on four constraints:

- For each observable, the binning should be the same for all jet categories.
- The bin width should not be smaller than the detector resolution.
- The statistical uncertainty should in general not exceed the systematic uncertainty.
- Each bin should have enough events to allow a data-driven background decomposition.

The 3-jet category is only measured inclusively ($\geq$ 3 jets). All other jet categories are measured exclusively ($= n$ jets), inclusive spectra are derived based on the exclusive cross sections as described in section 5.8.4.

Observable	0-jet	1-jet	2-jet	$\geq$ 3-jet
$m_{\gamma\gamma}$	✓	✓	✓	✓
$p_T^{\gamma\gamma}$	✓	✓	✓	✓
$\cos\theta^*_{\gamma\gamma}$	✓	✓	✓	✓
$\Delta\phi_{\gamma\gamma}$	✓	✓	✓	✓
m_{jj}			✓	✓
p_T^{jj}			✓	✓
$\Delta\phi_{jj}$			✓	✓
Δy_{jj}			✓	✓
$\Delta R_{\gamma_1 j_1}$		✓	✓	✓
$\Delta R_{\gamma_2 j_1}$		✓	✓	✓
$\Delta R_{\gamma_1 j_2}$			✓	✓
$\Delta R_{\gamma_2 j_2}$			✓	✓
$\Delta S_{\gamma\gamma,jj} = \Delta\phi_{\gamma\gamma,jj}$			✓	✓
$p_T^{jet_1}$		✓	✓	✓
$p_T^{jet_2}$			✓	✓
$p_T^{jet_3}$				✓

Table 5.2: *Observables measured in the analysis. The first four observables have been measured inclusively (not as function of the number of jets) before, the other observables are measured for the first time with the ATLAS detector.*

Variable	# bins	bin edges
$m_{\gamma\gamma}$	21	60 65 70 75 80 85 90 95 100 105 110 120 130 140 150 170 200 240 300 400 600 1000
$p_{T,\gamma\gamma}$	21	0 10 20 25 30 35 40 45 50 55 60 65 70 75 80 90 100 125 150 200 300 500
$\Delta\phi_{\gamma\gamma}$	25	0 0.25 0.5 0.75 1 1.25 1.5 1.625 1.75 1.875 2 2.125 2.25 2.375 2.5 2.575 2.65 2.725 2.8 2.85 2.9 2.95 3 3.05 3.1 3.1416
$cos\theta^{*}_{\gamma\gamma}$	25	0 - 1 in bins of 0.04
m_{jj}	23	0 30 40 50 60 70 85 100 115 130 150 175 200 225 250 275 300 350 400 500 600 800 1000 2000
$p_{T,jj}$	16	0 10 20 30 45 60 75 90 115 130 150 200 260 330 400 500 600
$\Delta\phi_{jj}$	18	0 0.3 0.6 0.9 1.2 1.5 1.8 2 2.2 2.4 2.5 2.6 2.7 2.8 2.9 3 3.05 3.1 3.1416
Δy_{jj}	16	0 0.2 0.4 0.6 0.8 1 1.2 1.4 1.6 1.8 2 2.2 2.5 3 3.5 4.5 6
$\Delta S_{\gamma\gamma,jj}$	20	0 0.5 1.0 1.5 1.75 2.0 2.25 2.35 2.45 2.55 2.65 2.7 2.75 2.8 2.85 2.9 2.95 3.0 3.05 3.1 3.1416
$\Delta R_{\gamma j}$	20	0.6 1 1.4 1.8 2 2.2 2.4 2.5 2.6 2.7 2.8 2.9 3 3.1 3.2 3.4 3.6 3.8 4 4.5 6
$p_T^{jet_1}$	13	25 40 50 60 70 80 90 105 125 150 200 275 400 800
$p_T^{jet_2}$	12	25 40 50 60 70 80 90 105 125 150 200 275 400
$p_T^{jet_3}$	11	25 40 50 60 70 80 90 105 125 150 200 275

Table 5.3: *Binning used for the observables in this analysis.*

5.3 Subtraction of hadronic background

In the analysis, the main background component comes from jets being reconstructed and identified as photons, so-called “fake photons”. Jets are more frequent than photons by more than three orders of magnitude, with the precise number depending on the phase space region. While the photon reconstruction and identification (see section 4.4) remove the vast majority of those jets, the remaining contribution, called “jet background”, is still sizable and has to be subtracted. Three different methods have been developed for ATLAS analyses with two photons:

- The “2x2D sideband method” [41] is described in this section.
- The “4x4 matrix method” [61] is described in the following section.
- The “template fit method” [41] is not used in this analysis. For this method templates of photon and jet isolation profiles are produced and the isolation distributions are fitted to estimate their relative fraction.

The 2x2D sideband method was studied first for this analysis. It showed some deviations from the expected result in a closure test. The 4x4 matrix method performed better in this closure test, therefore it was chosen as default method later. The 2x2D sideband method is used as control method and compared to the results of the other method.

Both the 2x2D sideband method and the 4x4 matrix method estimate the jet background using control regions enriched in background events in terms of isolation and photon identification. For the isolation, two different control regions are considered: “non-isolated” ($\tilde{\mathrm{I}}$) photon candidates fail the isolation selection of $E_T^{\mathrm{isol}} < 4$ GeV, “anti-isolated” ($\tilde{\tilde{\mathrm{I}}}$) photon candidates are those with $E_T^{\mathrm{isol}} > 10$ GeV, with additional constraints depending on the method.

For the photon identification control regions (“non-tight”, $\tilde{\mathrm{T}}$), the candidates pass the “loose” photon selection, but they are required to fail at least one out of a given set of shower shape selection criteria for the tight identification - nominally four, but two, three and five are used to estimate systematic uncertainties. This method has been established in [48]. Table 5.4 shows the selection criteria for the different regions.

For each photon candidate, identification and isolation are used to define 4 categories:

- TI: candidates that pass both the tight photon identification and the isolation selection
- T$\tilde{\mathrm{I}}$: candidates that pass the tight photon identification, but not the isolation selection

Region	Candidates fail at least one of those shower shape criteria
T	-
nT_2	$w_{s,3}$, f_{side}
nT_3	$w_{s,3}$, f_{side}, ΔE
nT ($\tilde{\mathrm{T}}$)	$w_{s,3}$, f_{side}, ΔE, E_{ratio}
nT_5	$w_{s,3}$, f_{side}, ΔE, E_{ratio}, $w_{\mathrm{s,tot}}$

Table 5.4: *Definition of the non-tight regions. The variables are chosen as they have a small correlation with the photon isolation.*

- $\tilde{\mathrm{T}}$I: candidates that are in the non-tight control region, but pass the isolation selection

- $\tilde{\mathrm{T}}\tilde{\mathrm{I}}$: candidates that are in the control region both for isolation and photon identification

It is assumed, and verified via simulations, that photon identification and isolation are not correlated notably for photons. In particular, the following relation holds for events with photons:

$$N_{\mathrm{TI}} N_{\tilde{\mathrm{T}}\tilde{\mathrm{I}}} = N_{\mathrm{T}\tilde{\mathrm{I}}} N_{\tilde{\mathrm{T}}\mathrm{I}} \tag{5.2}$$

With two photon candidates, this leads to 16 categories. As an example, the signal region is TITI, where the first TI refers to the leading photon candidate and the second TI refers to the subleading photon candidate.

As identification and isolation do not give a perfect separation between photons and jets all 16 categories consist of a mixture of signal events ($\gamma\gamma$), events with one fake photon (γj and $j\gamma$) and events with two fake photons (jj).

5.3.1 2x2D sideband method

The 2x2D sideband method performs a fit to the observed event yields in the 16 categories to extract the fraction of signal events in each category. This fit is done independently in every bin in every observable and jet category in the analysis.

Fake rates (probability that a jet passes a selection) and efficiencies (probability that a photon passes a selection) are introduced, separately for leading ($k = 1$) and subleading ($k = 2$) photon candidates. All probabilities are relative to the total number of objects either passing the "tight" selection or being in the "non-tight" control region. Photon-jet events are mainly from quarks in the initial state, while events with two jets mainly originate from gluons. Gluons have a larger color charge and lead (on average) to less isolated jets. Therefore, jets in photon-jet events differ from jets in jet-jet events. To take this into account, three additional correlation factors have to be considered, two quantifying the

Variable	Parameters	Description
ε_{Ik}	2	Isolation efficiency for photons
ε_{Tk}	2	Tight identification efficiency for photons
f_{Ik}	2	Isolation fake rate for jets where the other object is a photon
f_{Tk}	2	Tight identification fake rate for jets where the other object is a photon
f'_{Ik}	2	Isolation fake rate for jets where the other object is a jet
f'_{Tk}	2	Tight identification fake rate for jets where the other object is a jet
ξ_{jk}	2	Correlation between identification and isolation fake rate for jets.
ξ_{Ijj}	1	Correlation between the jet isolation fake rates in events with two jets.

Table 5.5: *Parameters used in the* 2x2D *sideband method.*

correlation between identification and isolation, and one quantifying the correlation between the jet isolation fake rates in events with two jets. The parameters are listed in table 5.5.

Together with the number of events with two photons $N_{\gamma\gamma}$, leading photon and subleading jet $N_{\gamma j}$, leading jet and subleading photon $N_{j\gamma}$, and two jets N_{jj}, all summed over the "tight" and "non-tight" photon identification region, those parameters lead to formulas for the event yields in all 16 categories. As an example, $N_{\mathrm{T\tilde{I}\tilde{T}I}}$ is shown here, all formulas can be found in appendix A.5.

$$\begin{aligned} N^{\mathrm{T\tilde{I}\tilde{T}I}} =& N_{\gamma\gamma}\left(1-\varepsilon_{I1}\right)\varepsilon_{T1}\varepsilon_{I2}\left(1-\varepsilon_{T2}\right) \\ &+ N_{\gamma j}\left(1-\varepsilon_{I1}\right)\varepsilon_{T1}f_{I2}\left(1-f_{T2}\xi_{j2}\right) \\ &+ N_{j\gamma}\left(1-f_{I1}\xi_{j1}\right)f_{T1}\varepsilon_{I2}\left(1-\varepsilon_{T2}\right) \\ &+ N_{jj}\left(1-f'_{I1}\xi_{Ijj}\xi_{j1}\right)f'_{T1}f'_{I2}\left(1-f'_{T2}\xi_{j2}\right) \end{aligned} \tag{5.3}$$

In total there are 19 unknown parameters. 16 categories give 16 observed event yields, therefore the system is underconstrained, and additional information has to be used to estimate the event yields.

- Two of the correlation parameters, ξ_{j1} and ξ_{j2}, are set to 1. Monte Carlo studies suggest no significant correlation between tight identification and isolation efficiency for jets. A variation of those parameters is considered as systematic uncertainty.

- The isolation efficiencies ε_{I1}, ε_{I2} for leading and subleading photons are determined in data, as described in the following section.

- The tight identification efficiencies ε_{T1}, ε_{T2} for leading and subleading photons are taken from Monte Carlo simulations, after shifting their shower shapes (see section 4.4.3) and applying efficiency scale factors to improve the agreement with data-driven measurements. The scale factors are derived from a comparison between measurements of the efficiency in data and the result in simulations. Using the measured efficiencies directly would need efficiency measurements in every bin of the analysis, this does not work for some observables and the dataset is not large enough to provide accurate values in most bins. Possible correlations between the tight identification efficiency between the two photons are taken into account as described in [73]. The efficiencies in the different jet bins are shown in table 5.6.

Tight ID eff.	0-jet	1-jet	2-jet	$\geq$ 3-jet
ε_{T1}	0.9602±0.0001	0.9718±0.0001	0.9736±0.0002	0.9762±0.0004
ε_{T2}	0.9442±0.0001	0.9462±0.0002	0.9492±0.0003	0.9507±0.0005

Table 5.6: *Tight identification efficiencies, inclusive in the observables, as function of the number of jets in the event.*

This leads to 13 parameters as fit result and $N_{\gamma\gamma}$ together with the efficiencies allows to calculate the number of signal events in the signal region, the main result of the 2x2D sideband method:

$$N_{\gamma\gamma}^{\mathrm{TITI}} = N_{\gamma\gamma}\varepsilon_{T1}\varepsilon_{I1}\varepsilon_{T2}\varepsilon_{I2} \tag{5.4}$$

Example yields are shown in figure 5.1.

Data-driven isolation efficiency

The 2x2D sideband method relies on the photon isolation efficiencies as input. While it is possible to take them from simulation alone, a more model-independent estimate is possible using a combination of experimental data and simulation ("data-driven"). It is done independently for leading and subleading photons, the other photon candidate is always required to be tight and isolated, as this improves the photon purity of the other candidate and also reduces any potential influence of correlations between the photon candidates. The isolation efficiency is evaluated in 4 bins of pseudorapidity and 6 bins of transverse energy of the photon candidate, separately for the different jet categories.

In order to get a high purity jet background sample, photon candidates in an anti-isolation region of 10 GeV $< E_T^{\mathrm{isol}} <$ 25 GeV are considered. An additional requirement on track isolation, 10 GeV $< p_T^{\mathrm{isol}} <$ 25 GeV is added to further improve the purity in background.

The distribution of the isolation energy for tight and non-tight photon candidates is computed, the distribution of the non-tight candidates is then normalized

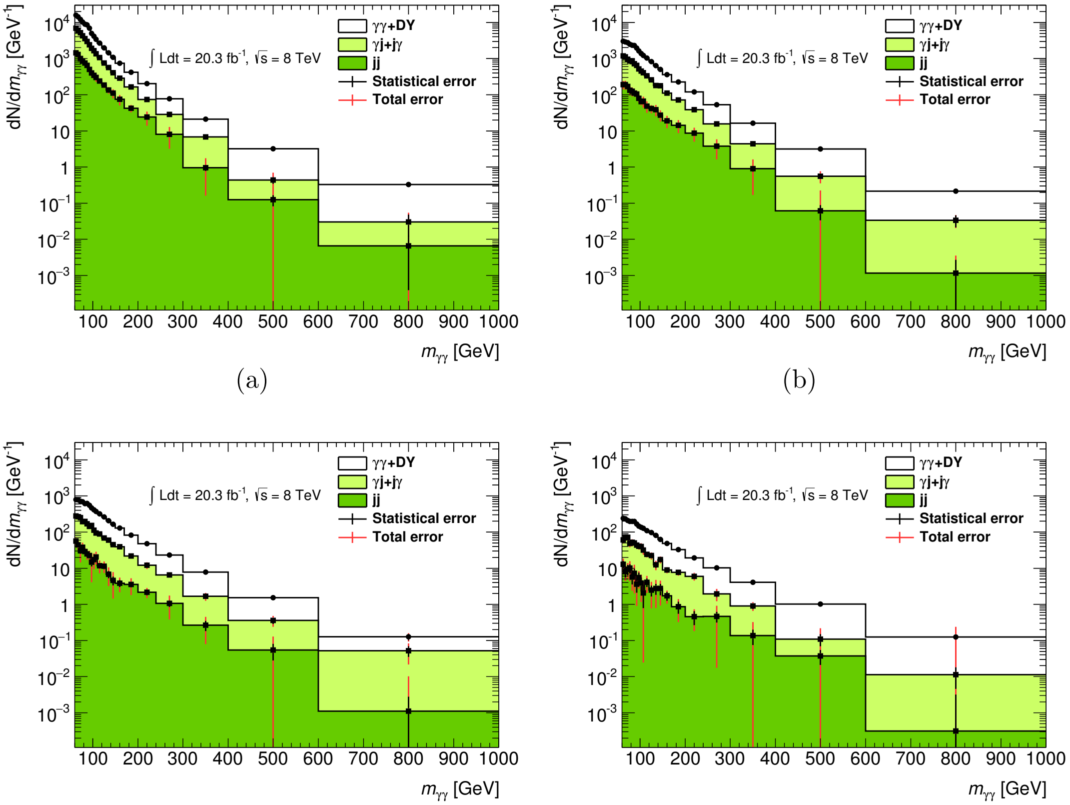

(a) (b) (c) (d)

Figure 5.1: *Yields of diphoton events, photon-jet and jet-photon events, and dijet events as a function of* $m_{\gamma\gamma}$ *for the different jet categories: 0 (a), 1 (b), 2 (c) and* ≥ 3 *(d) jets.*

to have the same number of events in the described anti-isolation region. It is then subtracted from the distribution obtained with the tight candidates. The difference is an estimate of the isolation distribution of true photons. The fraction of those events with an isolation of $E_T^{\mathrm{isol}} < 4$ GeV is the isolation efficiency.

The size of the analyzed dataset limits this method to $E_T^\gamma < 400$ GeV. For photons with a higher transverse energy, the efficiency of the highest transverse energy bin is used.

To be used in the 2x2D sideband method, the efficiencies in bins of the observable are needed. The propagation from bins in transverse momentum and pseudorapidity to bins of the observables is done using the Sherpa simulation: the data-driven isolation efficiencies are applied to all events in every bin in every observable and jet category, and the average efficiency in each bin is then calculated. The efficiencies for the 0-jet and 1-jet category are shown in figure 5.2.

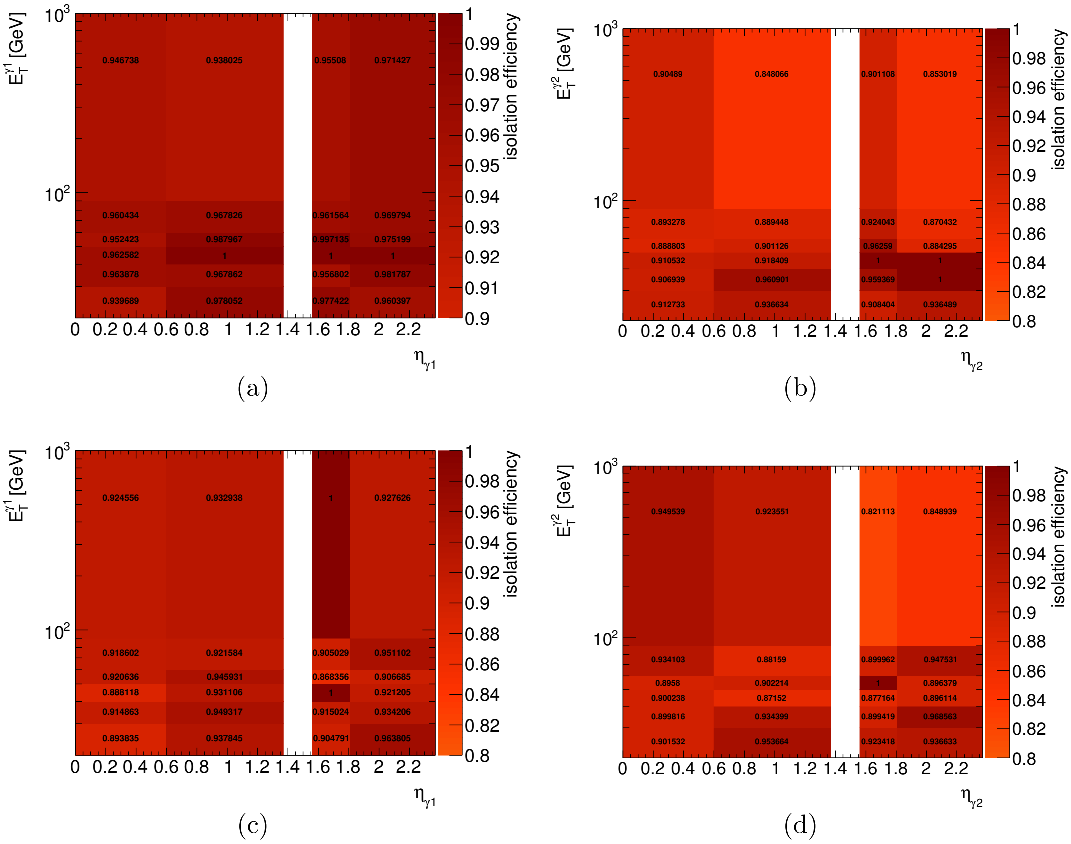

(a) (b)

(c) (d)

Figure 5.2: *Data-driven isolation efficiencies for photons as function of transverse momentum and pseudorapidity for the leading candidate (left) and subleading candidate (right) for the 0-jet (top) and 1-jet (bottom) category as a function of* η *and* $E_T = p_T$ *of the photon candidate. From [74] with adjusted scale.*

The data-driven isolation efficiency varies between 85% and 99%, depending on the observable and jet category. Table 5.7 summarizes the efficiencies as function of the number of jets in the event. It is usually lower than the Sherpa estimate. Running the background decomposition with the Sherpa estimates changes the signal yield by less than 2%.

Isol. eff.	0-jet	1-jet	2-jet	≥3-jet
ϵ_{I1}	0.9710±0.0006	0.9234±0.0011	0.9118±0.0017	0.8787±0.0026
ϵ_{I2}	0.9297±0.0006	0.9194±0.0011	0.9256±0.0018	0.9074±0.0027

Table 5.7: *Isolation efficiencies as function of the number of jets in the event, for leading and subleading photon. Uncertainties shown here are statistical only.*

Systematic uncertainties

Several assumptions go into the background subtraction, which leads to systematic uncertainties based on the uncertainties involved in those assumptions. Figure 5.3 shows the total systematic uncertainty for the diphoton invariant mass, figure 5.4 shows the different contributions to the systematic uncertainty in the 0-jet category.

Correlation between isolation and identification fake rate for jets This correlation can be described with the quotient $R = \frac{N_{\mathrm{TI}} N_{\tilde{\mathrm{T}}\tilde{\mathrm{I}}}}{N_{\mathrm{T}\tilde{\mathrm{I}}} N_{\tilde{\mathrm{T}}\mathrm{I}}}$, separately for leading and subleading photon. Studies done for the inclusive diphoton analysis [75] show that the ratio is close to one for both jets. It is allowed to vary between 0.9 and 1.1 as variations in simulations were shown to not exceed this. The corresponding change of the background subtracted yields is taken as uncertainty, it is negligible everywhere.

Choice of non-tight control region The non-tight control region plays a crucial part in the 2x2D sideband method. It is chosen to get photon-like jet background, with the actual photon contribution as small as possible. For the nominal background subtraction, photon candidates are required to fail at least one out of four selected shower shapes. This choice is arbitrary to some extent, so control regions with two, three and five shower shapes (see table 5.4) to fail are also considered. Including fewer shower shapes to possibly fail removes more photon candidates where just a few shower shapes fail the tight selection. It reduces the photon component, but it also removes more jet candidates that are similar to jets in the signal region. The tight identification and isolation efficiencies are re-derived with respect to the different control regions, and the fit to extract the signal yields is performed for each variant. The largest absolute

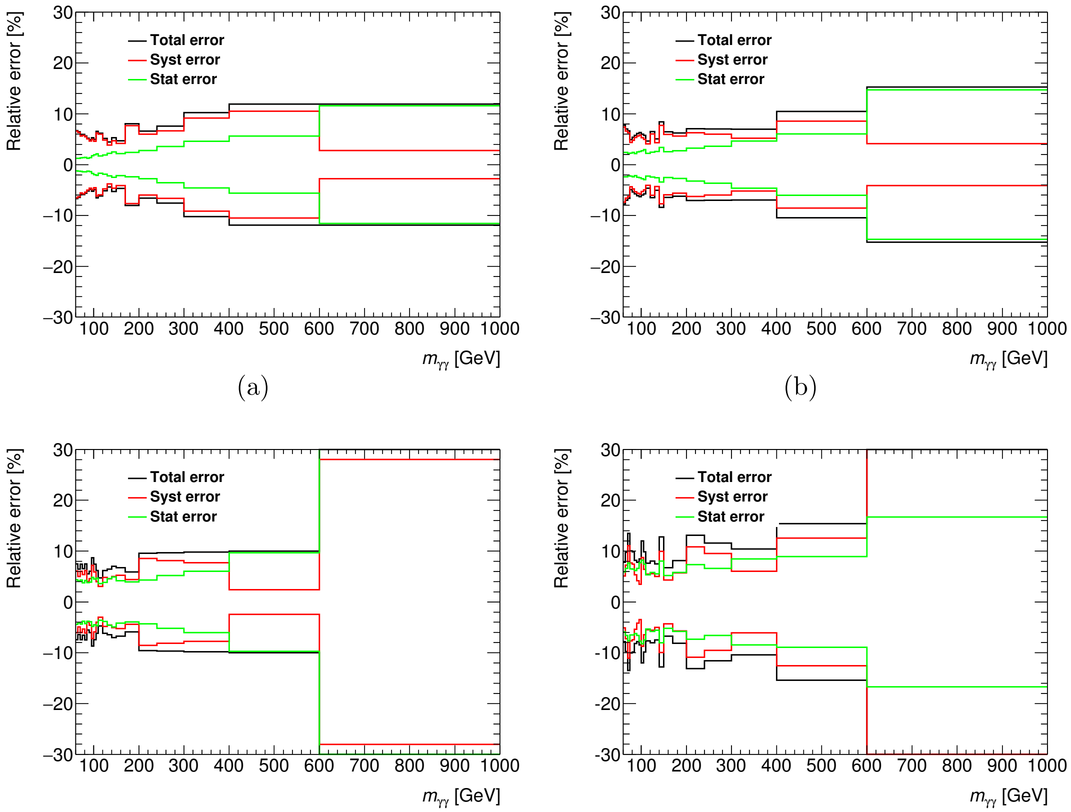

(a) (b)

(c) (d)

Figure 5.3: *Total relative systematic uncertainties of the* 2x2D *sideband method compared to the statistical uncertainty as a function of* $m_{\gamma\gamma}$ *for the different jet categories: 0 (a), 1 (b), 2 (c) and* $\geq$ *3 (d) jets. The choice of the "non-tight" control region is the largest uncertainty [74].*

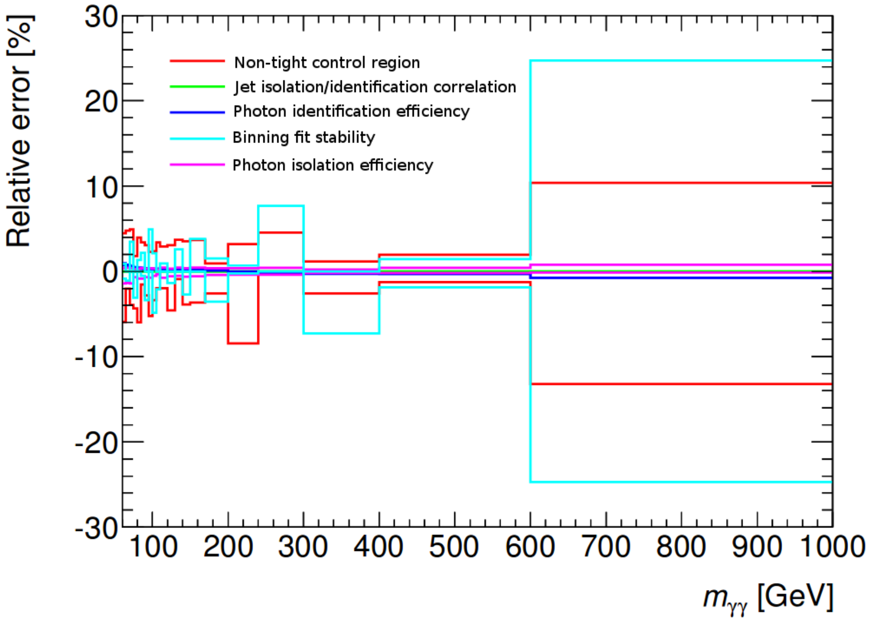

Figure 5.4: *Relative systematic uncertainties of the* 2x2D *sideband method as a function of* $m_{\gamma\gamma}$ *for the 0-jet category. The choice of the non-tight control region and the binning fit stability are the dominant uncertainties.*

deviation is taken as systematic uncertainty, separately for variations up and down in the yield. It is the largest systematic uncertainty of the background subtraction, typically leading to a relative uncertainty of a few percent.

Photon isolation efficiency To evaluate the isolation efficiency of photons in data, an "anti-isolation" was chosen. To evaluate the influence of this choice on the signal yield, the lower edge of the track isolation criterion (nominally 10 GeV) is lowered to 8 GeV or increased to 12 GeV. The impact on the signal yield is below 1%.

While the isolation efficiency of photons in bins of transverse energy and pseudorapidity is evaluated in data, the conversion to the efficiencies in bins of the observables relies on simulations. Nominally the Sherpa simulation is used, the isolation efficiency is also derived with the Pythia simulation and the difference is taken into account as systematic uncertainty. It is at the per mille level and therefore negligible.

Binning of efficiencies and fake rates - fit stability The low number of events in some bins can lead to large uncertainties in the 2x2D sideband method fit. In order to evaluate the fit stability and the dependence on the binning, the fit is performed in each bin using efficiencies and fake rates from the neighbor bins in the observables in both directions. The observed difference is used as systematic uncertainty, it is typically below 4%, but can reach up to 10% in some bins. Even larger uncertainties can occur in bins with very low event yields.

Photon identification efficiency To estimate the uncertainty coming from the description of the photon efficiency in MC, the scale factors are varied within their uncertainties, while taking correlations between the two photon candidates into account, as described in [47]. The uncertainty on the signal yields is below 0.5%. An exception are bins where the event yields are too small to properly evaluate this systematic uncertainty, but there the statistical uncertainty and other systematic uncertainties are larger.

5.4 Subtraction of hadronic background - method 2

The 4x4 matrix method mainly uses events where both photon candidates pass the tight identification. Similar to the 2x2D sideband method, efficiencies and fake rates are introduced, separately for leading ($k = 1$) and subleading ($k = 2$) photons and jets but limited to the isolation efficiency. They are listed in table 5.8. This allows to express the event yields in the four categories (based on isolation properties of the two photon candidates) as a function of the number of diphoton, leading photon and subleading jet, leading jet and subleading photon, and dijet events. The connection between these two is a 4-by-4 matrix, shown in equation 5.5, hence the name of the method.

Variable	#	Description
ε_k	2	Isolation efficiency for photons, assumed to be identical for diphoton and photon+jet events
$f_1^{j\gamma}$,$f_2^{\gamma j}$	2	Isolation fake rate for leading and subleading jet, respectively, where the other object is a photon
f_k^{jj}	2	Isolation fake rate for leading and subleading jet, where the other object is a jet as well
ξ	1	Correlation between the jet isolation fake rates in events with two jets.

Table 5.8: *Parameters used in the 4x4 matrix method.*

$$\begin{pmatrix} N_{\mathrm{II}} \\ N_{\mathrm{I\tilde{I}}} \\ N_{\mathrm{\tilde{I}I}} \\ N_{\mathrm{\tilde{I}\tilde{I}}} \end{pmatrix} = \begin{pmatrix} \varepsilon_1\varepsilon_2 & \varepsilon_1 f_2^{\gamma \mathrm{j}} & f_1^{\mathrm{j}\gamma}\varepsilon_2 & \xi f_1^{\mathrm{jj}} f_2^{\mathrm{jj}} \\ \varepsilon_1(1-\varepsilon_2) & \varepsilon_1(1-f_2^{\gamma \mathrm{j}}) & f_1^{\mathrm{j}\gamma}(1-\varepsilon_2) & f_1^{\mathrm{jj}}(1-\xi f_2^{\mathrm{jj}}) \\ (1-\varepsilon_1)\varepsilon_2 & (1-\varepsilon_1)f_2^{\gamma \mathrm{j}} & (1-f_1^{\mathrm{j}\gamma})\varepsilon_2 & (1-\xi f_1^{\mathrm{jj}})f_2^{\mathrm{jj}} \\ (1-\varepsilon_1)(1-\varepsilon_2) & (1-\varepsilon_1)(1-f_2^{\gamma \mathrm{j}}) & (1-f_1^{\mathrm{j}\gamma})(1-\varepsilon_2) & (1-f_1^{\mathrm{jj}}-f_2^{\mathrm{jj}}+\xi f_1^{\mathrm{jj}} f_2^{\mathrm{jj}}) \end{pmatrix} \begin{pmatrix} N_{\gamma\gamma} \\ N_{\gamma j} \\ N_{j\gamma} \\ N_{jj} \end{pmatrix} \tag{5.5}$$

The seven parameters in the matrix are evaluated in simulations or in a data-driven approach, as described in the following subsections. Inverting the matrix allows to determine $N_{\gamma\gamma}$ based on the observed event yields in the four categories. The final signal yield is then given by $N_{\gamma\gamma,\mathrm{II}} = \varepsilon_1\varepsilon_2 N_{\gamma\gamma}$. This is done for each bin in each jet category for each variable.

5.4.1 Data-driven estimate of photon isolation efficiencies

The isolation efficiency is the probability that a photon passing the tight selection also passes the isolation selection. To estimate photon isolation efficiencies, separately for the leading and subleading photon candidate, candidates that fail the tight identification are considered. Let $\alpha = \frac{n_\gamma^{\tilde{\mathrm{T}}}}{n_\gamma^{\mathrm{T}}}$ be the ratio of the number of photons that fail the tight identification and the photons that pass it. Let $\beta = \frac{n_j^{\mathrm{T}}}{n_j^{\tilde{\mathrm{T}}}}$

be the ratio of the number of jets that pass the tight identification and the jets that fail it.

It is assumed that those ratios are the same if they are limited to isolated photon candidates, as correlations between identification and isolation fake rates are very small. This assumption is also used in the 2x2D sideband method, see section 5.3.1 for a discussion. The number of photons that pass the tight identification can then be written as $n_\gamma^{\mathrm{T}} = n^{\mathrm{T}} - \beta(n^{\tilde{\mathrm{T}}} - \alpha n_\gamma^{\mathrm{T}})$. Solving for n_γ^T using the same equation limited to isolated photon candidates leads to the isolation efficiency:

$$\varepsilon = \frac{n_\gamma^{\mathrm{TI}}}{n_\gamma^{\mathrm{T}}} = \frac{n^{\mathrm{TI}} - \beta n^{\tilde{\mathrm{T}}\mathrm{I}}}{n^{\mathrm{T}} - \beta n^{\tilde{\mathrm{T}}}} \tag{5.6}$$

The parameter α cancels in the ratio. To evaluate β, an anti-isolation region $\tilde{\tilde{\mathrm{I}}}$ is defined, in this region the fraction of photons is negligible. Photon candidates are required to have track isolation $p_T^{\mathrm{isol}} > 10$ GeV and calorimeter isolation $E_T^{\mathrm{isol}} > 3$ GeV. Similar to above, it is assumed that the jet fake rate for the photon identification is the same in this isolation range. This leads to a direct estimate from data:

$$\beta = \frac{n^{\mathrm{T}\tilde{\tilde{\mathrm{I}}}}}{n^{\tilde{\mathrm{T}}\tilde{\tilde{\mathrm{I}}}}} \tag{5.7}$$

Plugging this into the equation from above, the isolation effiency is computed based on observed event yields in different regions only:

$$\varepsilon = \frac{n^{\mathrm{TI}} - \frac{n^{\mathrm{T}\tilde{\tilde{\mathrm{I}}}}}{n^{\tilde{\mathrm{T}}\tilde{\tilde{\mathrm{I}}}}} n^{\tilde{\mathrm{T}}\mathrm{I}}}{n^{\mathrm{T}} - \frac{n^{\mathrm{T}\tilde{\tilde{\mathrm{I}}}}}{n^{\tilde{\mathrm{T}}\tilde{\tilde{\mathrm{I}}}}} n^{\tilde{\mathrm{T}}}} \tag{5.8}$$

5.4.2 Data-driven estimate of f

Similar to the determination of the photon isolation efficiency, it is possible to evaluate the fake rate as ratio of event yields. In this case α remains in the equations and has to be evaluated in simulations.

$$f = \frac{n^{\tilde{\mathrm{T}}\mathrm{I}} - \alpha n^{\mathrm{TI}}}{n^{\tilde{\mathrm{T}}} - \alpha n^{\mathrm{T}}} \tag{5.9}$$

Taking into account the identity of the other object leads to two subcases described in the following subsections. Formulas shown and descriptions are always for the leading photon candidate, the subleading candidate is treated in the same way.

Estimate of f and ξ for dijet events

To evaluate the fake rate of the leading jet, f_1^{jj}, the subleading photon candidate is required to be non-tight.

$$f_1^{jj} = \frac{n^{\tilde{\mathrm{T}}\mathrm{I}\tilde{\mathrm{T}}} - \alpha n^{\mathrm{TI}\tilde{\mathrm{T}}}}{n^{\tilde{\mathrm{T}}\tilde{\mathrm{T}}} - \alpha n^{\mathrm{T}\tilde{\mathrm{T}}}} \tag{5.10}$$

Here, for each event yield, the first symbols are referring to the leading candidate (first identification, then isolation), the following symbols are for the subleading candidate. If the isolation status is not specified for one or both candidates, the yields of both isolation regions are added.

To evaluate the correlation between the isolation fake rates, conditional fake rates are defined, where the other candidate is required to be isolated or not isolated, respectively.

$$f_1^{jj}|\mathrm{I}_2 = \frac{n^{\tilde{\mathrm{T}}\mathrm{I}\tilde{\mathrm{T}}\mathrm{I}} - \alpha n^{\mathrm{TI}\tilde{\mathrm{T}}\mathrm{I}}}{n^{\tilde{\mathrm{T}}\tilde{\mathrm{T}}\mathrm{I}} - \alpha n^{\mathrm{T}\tilde{\mathrm{T}}\mathrm{I}}} = \xi f_1^{jj} \tag{5.11}$$

$$f_1^{jj}|\tilde{\mathrm{I}}_2 = \frac{n^{\tilde{\mathrm{T}}\mathrm{I}\tilde{\mathrm{T}}\tilde{\mathrm{I}}} - \alpha n^{\mathrm{TI}\tilde{\mathrm{T}}\tilde{\mathrm{I}}}}{n^{\tilde{\mathrm{T}}\tilde{\mathrm{T}}\tilde{\mathrm{I}}} - \alpha n^{\mathrm{T}\tilde{\mathrm{T}}\tilde{\mathrm{I}}}} = \frac{f_1^{jj}(1 - \xi f_2^{jj})}{1 - f_2^{jj}} \tag{5.12}$$

The conditional fake rates $f_2^{jj}|\mathrm{I}_1$ and $f_2^{jj}|\tilde{\mathrm{I}}_1$ are defined analogously. In total, four formulas allow to extract ξ, two from the leading and two from the subleading candidate. Ideally, all four would give the same value. Statistical fluctuations of the number of events in the control regions and possible small violations of the underlying assumptions of the method can lead to different values. The arithmetic average of all four values is used to reduce those effects.

Estimate of f and ξ for photon and jet events

Following the same approach as for events with two jets leads to the following formula, where the subleading candidate is required to be tight and isolated.

$$f_1^{j,\mathrm{TI}} = \frac{n^{\tilde{\mathrm{T}}\mathrm{ITI}} - \alpha n^{\mathrm{TITI}}}{n^{\tilde{\mathrm{T}}\mathrm{TI}} - \alpha n^{\mathrm{TTI}}} \tag{5.13}$$

Statistical uncertainty

Signal regions are used both in the extraction of efficiencies and fake rates and as input for solving the main matrix equation. To disentangle the statistical uncertainty, a bootstrap technique is used. Event counts in all regions are varied according to a Poisson distribution, where the expectation value is set to the observed value, and the signal yield is recomputed. This procedure is repeated 100 times, and the root mean square of the observed yield deviations from the nominal value is used as statistical uncertainty.

5.4.3 Systematic uncertainties

Similar to the 2x2D sideband method (see section 5.3.1), the dominant uncertainty arises from the choice of the non-tight control region. For the nominal control regions, photon candidates are required to fail at least one out of four selected shower shapes. Alternative control regions with two, three and five selected shower shapes (see table 5.4) are tested, the yields are recomputed in each case and the largest absolute deviation is taken as systematic uncertainty, separately for variations up and down in the yield.

The anti-isolation region chosen to calculate β uses a track isolation requirement of $p_T^{\mathrm{isol}} > 10$ GeV and calorimeter isolation $E_T^{\mathrm{isol}} > 3$ GeV. Monte Carlo simulations show that the fraction of photons in this region is 1% or lower. To investigate the dependency of the event yields on the chosen isolation criteria, the analysis is repeated with a requirement of $p_T^{\mathrm{isol}} > 5$ GeV instead of 10 GeV. The resulting difference in event yields is taken as systematic uncertainty.

The largest uncertainty is the choice of the non-tight control region, as discussed in section 5.9.1. It is typically a few percent, it can exceed 10% in bins with low event yields.

5.5 Subtraction of background from electrons

In addition to the background from jets reconstructed as photons, there is a background from electrons getting reconstructed as photons. Unless noted otherwise, "electrons" always refers to electrons and positrons as their charge sign is not taken into account. This contribution is much smaller, but still too large to be neglected. The contribution is particularly large (around 30%) in the diphoton invariant mass spectrum around 90 GeV due to the large number of Z decays to two electrons. There are two types of background processes leading to those events.

- Production of a photon and an electron, in particular $\gamma W^{\pm}(\rightarrow e^{\pm}\nu)$ and $\gamma Z(\rightarrow e^{+}e^{-})$
- Production of two electrons, mainly $\gamma, Z \rightarrow e^{+}e^{-}$ but also $W^{+}W^{-} \rightarrow e^{+}\nu e^{-}\bar{\nu}$

In order to subtract this background, it is necessary to evaluate the electron fake rate (the probability that an electron passes the photon reconstruction and selection) and the relative abundance of ee and γe events. The leading and subleading candidates are treated equally for the electron background, therefore there is no separate $e\gamma$ class. The electron background subtraction described here is used together with the 4x4 matrix method for jet background subtraction. A modified version of it can also be applied to the 2x2D sideband method, this is discussed in [74].

The $Z \rightarrow e^{+}e^{-}$ process is frequent enough to be notable as a feature in the invariant mass spectrum of the two photon candidates. Using the number of events in its peak in three mutually exclusive event categories is the key idea for the electron background subtraction. Both photon candidates are required to be isolated.

- $\gamma\gamma$: Events with two reconstructed photons that pass the tight selection.
- γe: Events with exactly one reconstructed photon that passes the tight selection, and at least one reconstructed electron that passes the "Medium++" selection.
- ee: Events with zero reconstructed photons passing the tight selection, where at least two electrons pass the Medium++ selection.

The electron reconstruction and selection in ATLAS is similar to the photon reconstruction and selection, but uses different shower shapes and different tracking information, the selection is discussed in [76]. Medium++ was chosen as it is similar to the photon tight selection in terms of selection criteria. The kinematic selection is identical for photons and electrons. Electrons are discarded if they are closer than $\Delta R = 0.4$ to any tight photon candidate.

Two ratios of fake rates to identification efficiencies are introduced. Here identification also includes the reconstruction process.

$$f_{e\to\gamma} = \frac{p(e\to\gamma)}{p(e\to e)} \qquad \text{and} \qquad f_{\gamma\to e} = \frac{p(\gamma\to e)}{p(\gamma\to\gamma)} \tag{5.14}$$

In these ratios, the numerator is the probability of a wrong identification, while the denominator is the probability of a correct identification. The electron selection requires a well-reconstructed track, this makes the photon to electron misidentification rate much smaller than the electron to photon misidentification rate: $f_{e\to\gamma} \gg f_{\gamma\to e}$. The photon to electron misidentification is neglected.

Using the fake rates, the number of observed events in each category N^{obs} can then be expressed as function of the number of true events $\hat{N}$ that get reconstructed correctly. As an example, $\hat{N}_{ee}$ is the number of ee events that get reconstructed as ee. These events are not in the other two categories, but their event yields can be used to calculate the ee contribution to those.

$$\begin{aligned} N^{obs}_{\gamma\gamma} &= \hat{N}_{\gamma\gamma} + f_{e\to\gamma}\cdot\hat{N}_{\gamma e} + (f_{e\to\gamma})^2\cdot\hat{N}_{ee} \\ N^{obs}_{\gamma e} &= \hat{N}_{\gamma e} + 2\,f_{e\to\gamma}\cdot\hat{N}_{ee} \\ N^{obs}_{ee} &= \hat{N}_{ee} \end{aligned} \tag{5.15}$$

This equation can be solved for $\hat{N}_{\gamma\gamma}$. Once $f_{e\to\gamma}$ has been evaluated, $\hat{N}_{\gamma\gamma}$ can be calculated as:

$$\hat{N}_{\gamma\gamma} = N^{obs}_{\gamma\gamma} - \left[f_{e\to\gamma}\cdot\hat{N}_{\gamma e} + (f_{e\to\gamma})^2\cdot\hat{N}_{ee}\right] \tag{5.16}$$

The right bracket represents the electron background.

5.5.1 Determination of $f_{e\to\gamma}$

Both in the ee and in the γe category the event yields show a peak in the invariant mass at the Z boson mass, this is shown in figure 5.5. As the decay $Z\to\gamma e$ is impossible and the radiative decay $Z\to ee\gamma$ is rare and does not lead to a peaking structure in $m_{\gamma e}$, both peaks are exclusively from Z boson decays $Z\to ee$.

The contribution from Z decays in the ee and γe categories is obtained via a fit to the invariant mass spectrum. As signal shape, a two-sided Crystal Ball function is used [77], the background is modeled with a hyperbolic tangent function multiplied by the exponential of a polynomial.

The ratio of the fitted yields in the peak leads to the fake rate:

$$f_{e\to\gamma} = \frac{N^{obs,Z}_{\gamma e}}{2N^{obs,Z}_{ee}} \tag{5.17}$$

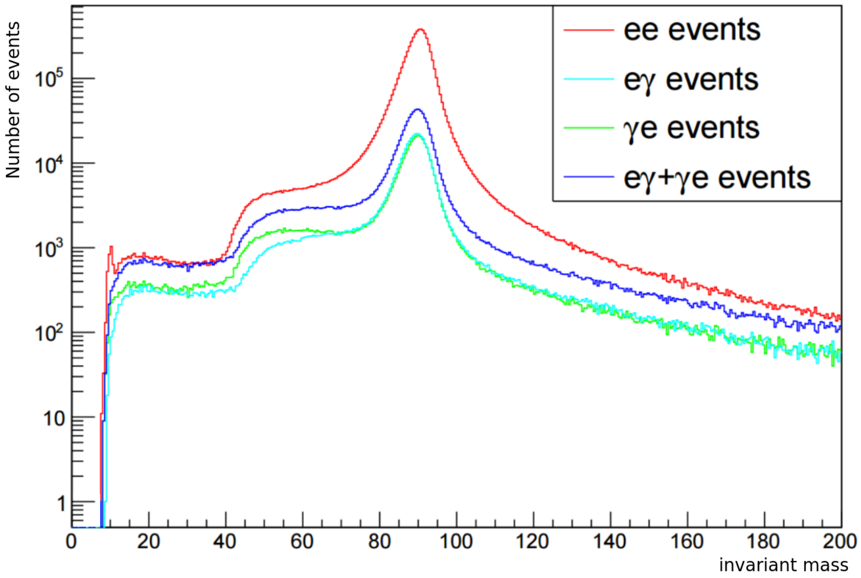

Figure 5.5: *The invariant mass distribution of ee and γe pairs. Z boson decays dominate around the Z mass. The structure at low invariant masses comes from the p_T requirements in the event selection, it is irrelevant for the electron background subtraction.*

The factor of 2 takes into account that the γe reconstruction of events with two electrons comes from a misidentification of either the leading (γe) or subleading ($e\gamma$) electron.

The fake rate is evaluated for isolated and for all photon candidates separately. Averaged over the whole phase space in this analysis, $f^{\text{isol}}_{e\to\gamma} = 0.078$ and $f^{\text{all}}_{e\to\gamma} = 0.065$. Z boson decays have a different kinematic distribution than the diphoton events studied. Simulations show a dependence of $f_{e\to\gamma}$ on the transverse momentum of the electron. This is taken into account as systematic uncertainty by increasing $f_{e\to\gamma}$ by 20% or decreasing it by 30%, to cover the whole range observed in simulations.

5.5.2 Differential evaluation of electron background

As this analysis measures the cross section in bins of several observables, the electron contribution in each bin of each observable has to be evaluated. Equation 5.16 could be evaluated in every bin. Limited statistics makes this approach problematic, however. The fraction of electrons in the signal region shows a strong dependence on the diphoton candidate invariant mass, but not on other variables. Each event is assigned a probability f_e to be background from electrons, based on the invariant mass of the diphoton candidate and a bin-by-bin evaluation of the fraction of electron background. This probability is evaluated for pairs of isolated photon candidates and other pairs of photon candidates separately, where the evaluation of the fake rates is repeated for these other pairs.

It is assumed that the probabilities based on the invariant mass are sufficient to describe the background. This assumption is tested on the other diphoton variables, $p_{\mathrm{T}}^{\gamma\gamma}$, $\Delta\phi_{\gamma\gamma}$ and $\cos\theta^*_{\gamma\gamma}$, and compared to the bin-by-bin approach. A good agreement is observed, with less than 1% deviation between the obtained diphoton yields.

5.5.3 Combination of electron and jet background subtraction

Electron and jet background cannot done in sequence, as the control regions for the electron background contain jets and the control regions for the jet background contain electrons. With the probabilities f_e described in the previous subsection, it is straightforward to subtract the electron background in each control region of the jet background subtraction: Each event in each region is taken into account with a weight of $(1 - f_e)$ where f_e depends on the invariant mass of the photon candidates in the event. This subtraction is done for regions with two tight photon candidates only, as the contribution of electrons in other regions is negligible.

As can be seen in the spectra shown in section 5.10, there is no Z-boson peak remaining at an invariant mass of 90 GeV.

5.6 Contribution from Higgs decays

While the recently discovered Higgs boson is not in the focus of this analysis, Higgs bosons can decay to two photons, leading to events in the fiducial phase space of this measurement. In addition, there is interference between processes involving a Higgs boson and processes without. This interference is difficult to predict theoretically, although it is known to be small compared to the Higgs contribution [78]. The contribution from the Higgs boson is considered as part of the signal. MC samples for a Standard Model Higgs boson at a mass of 125 GeV were produced to study it. Its distribution peaks in the diphoton invariant mass spectrum at around 125 GeV, where it contributes about 1% to the cross section in the bin from 120 to 130 GeV. This is smaller than the systematic uncertainties in the bin. The contribution is completely negligible everywhere else.

5.7 Efficiency of the event selection

5.7.1 Trigger efficiency

The trigger used for the analysis is `2g20vh_medium`. It selects events with two photons with at least 20 GeV transverse momentum each, with a "medium" photon identification, see section 4.4 for details. The efficiency of this trigger has been studied in [79]. In this analysis, the efficiency is 98.66%0.19%. It is taken into account in the unfolding, as the reconstructed events in the MC-based response matrix are required to pass the (simulated) trigger.

5.7.2 Detector efficiency

To allow comparisons to theoretical predictions and between experiments, it is not sufficient to measure event yields, the analysis has to evaluate the cross sections of the studied processes. Several effects lead to observed event yields that do not directly match the number of collisions producing the particles studied. They have to be estimated and taken into account:

- Reconstruction efficiency: photons or jets can be misreconstructed as different objects, or not getting reconstructed as individual objects at all.
- Selection efficiency: This mainly applies to the photon identification, as some photons fail the selection criteria. The jet selection criteria influence the selection efficiency as well, especially the requirement of a minimal transverse momentum.
- Pile-up: Jets coming from the same primary vertex as the photons can be misreconstructed as coming from a different primary vertex, while jets coming from a different primary vertex can be reconstructed as coming

from the same vertex as the photons. The primary vertex as origin of the photons can be misreconstructed as well.

All these effects are studied via simulations, with data-driven corrections where possible. The fraction of background events in data, f_{bg}, is calculated in each bin in each observable. This background does not include the jet and electron backgrounds as these have been subtracted before, it only includes events that are outside the fiducial phase space, but pass the selection cuts of the analysis. The number of signal events in a bin is then given by $N_{\text{signal}} = N_{\text{obs}}(1 - f_{\text{bg}})$ with the observed event yield (after jet and electron background subtraction) N_{obs}. This correction is typically of the order of a few percent.

Even for events that are in the fiducial phase space and selected in the analysis, the reconstructed event can end up in a wrong bin. This is taken into account via the unfolding procedure, described in the next section. As a very simplified description, it transforms N_{signal} via a matrix multiplication with a matrix M describing the bin migration: $N_{\text{afterunfolding}} = MN_{\text{signal}}$.

The efficiency ϵ is computed in each bin, and the event yields are estimated as $N_{\text{phys}} = \frac{N_{\text{afterunfolding}}}{\epsilon}$. The efficiency is typically about 2/3, it increases with increasing photon and jet energy as the photon identification gets more efficient and the jets are more likely to pass the selection criteria.

Finally, the event yields are divided by the integrated luminosity to get cross sections for each bin: $\sigma = \frac{N_{\text{phys}}}{\int \mathcal{L}\ \mathrm{d}t}$.

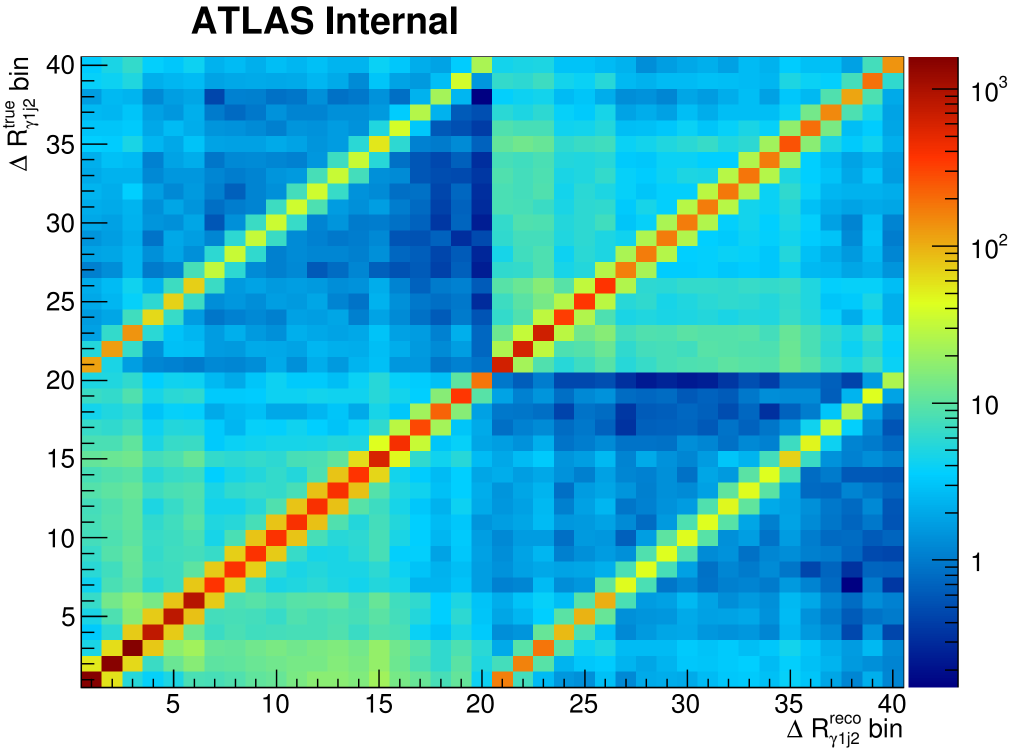

Figure 5.6: *An example bin migration matrix, here for $\Delta R_{\gamma 1 j2}$. The first 20 bins correspond to the 2-jet category, the second 20 bins correspond to the ≥ 3-jet category.*

5.8 Unfolding

Many analyses study distributions of observables in multiple bins. As detectors are not perfect, events that should be in one bin can get reconstructed in a different bin. This effect is called bin migration. Other events might not get reconstructed at all, or events get reconstructed that are not in the phase space considered. All three effects lead to deviations between measured distributions and true physical distributions. They have to be reversed to estimate the true distribution based on the reconstructed events. This procedure is called unfolding.

MC simulations of events and of the corresponding detector response allow to estimate bin migration. A bin migration matrix is formed, where one axis corresponds to the “true” (simulated) distribution and the other one to the reconstructed distribution, the entries are the probabilities that events within a given “truth” bin are reconstructed in a given reconstruction bin. Figure 5.6 shows an example from this analysis. The bin migration matrix M, applied to the simulated true distribution T, gives the simulated distribution R of reconstructed events. The inverse matrix M^{-1} allows to transform this reconstructed distribution back to the true distribution.

$$\sum_j M_{ij} T_j = R_i$$

$$\sum_i (M^{-1})_{ji} R_i = T_j$$

In data, R_i corresponds to the measurement in bin i, the bin migration matrix entries M_{ij} are typically estimated via MC simulations, T is unknown. The most naive approach for unfolding is a multiplication of the reconstructed distribution in data with the inverse of the bin migration matrix as shown above. Mathematically, this is the correct approach and gives the smallest variance among all unbiased estimators. In applications in particle physics and other fields, however, this often leads to large statistical uncertainties and spurious oscillations between neighboring bins.

Based on experience, physical distributions are rarely oscillating (for distributions where oscillations are expected, different analysis methods have to be used). This knowledge can be used as regularization in the unfolding procedure to avoid inflating the uncertainties.

If a minimization procedure is used to find the optimal T, regularization adds an additional term to this minimization procedure, based on deviations between unfolded data spectrum and MC distribution, or based on the relations between bins.

5.8.1 SVD Unfolding

Singular Value Decomposition (SVD) unfolding [80] normalizes data to the expected number of events in each bin, as this improves the statistical properties of the equations. The description here follows the notation used in the reference. A vector w is defined based on the vector x of the (unknown) true distribution in data and the vector x_{ini} of the known true distribution in MC.

$$w_j = \frac{x_j}{x_j^{\text{ini}}}$$

If the MC description is accurate, the ratio is 1 in every bin.

Instead of using the bin migration matrix, the unfolding problem for an observed distribution b in data can now be written with a matrix A containing the number of events in each bin.

$$\sum_{j=1}^{n} A_{ij} w_j = b_i$$

Each equation is then divided by the uncertainty of b_i to give all equations equal weight. This is denoted by a tilde above the rescaled entries.

$$\sum_{j=1}^{n} \tilde{A}_{ij} w_j = \tilde{b}_i$$

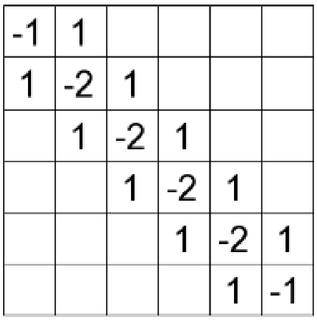

-1	1				
1	-2	1			
	1	-2	1		
		1	-2	1	
			1	-2	1
				1	-1

Figure 5.7: *The SVD curvature matrix for one-dimensional distributions*

To find w, the expression $(\tilde{A}w - \tilde{b})^T(\tilde{A}w - \tilde{b})$ can be minimized. This approach can still lead to the large fluctuations mentioned in the previous section, where w changes significantly between adjacent bins. To avoid this, an additional regularization term is introduced in the minimization.

$$(\tilde{A}w - \tilde{b})^T(\tilde{A}w - \tilde{b}) + \tau(Cw)^T Cw = \min$$

C is a matrix related to the expected behavior of w. τ, the strength of the regularization, is a free parameter.

For SVD unfolding, a curvature matrix is used for regularization (figure 5.7). The curvature matrix compares the ratios w_i in neighboring bins. In particular, it is assumed that the ratio w_i is approximately linear within bins nearby. SVD unfolding and its implementation in ROOT compares three bins next to each other to determine the curvature, which becomes part of the minimization function. A curvature leads to a penalty in the minimization. This minimization is implemented as a linear algorithm.

To choose the regularization strength, the rescaled bin migration matrix is examined. It can be written as product of a diagonal matrix S and two orthogonal matrices U and V^T: $\tilde{A} = USV^T$. The diagonal entries of S are called singular values of $\tilde{A}$. Small singular values, typically associated to large bin migration, lead to large entries in S^{-1} and therefore large entries in $(\tilde{A})^{-1} = VS^{-1}U^T$. This leads to the unwanted large fluctuations between neighboring bins, leading to a large curvature. The regularization suppresses the effect of small singular values. The parameter τ is set to the value of the kth singular value, where k is a free parameter of the method.

5.8.2 SVD Unfolding in multiple dimensions

SVD unfolding has been used successfully in many analyses. In the current implementation, it is limited to unfolding of one-dimensional distributions. Mimicking a one-dimensional distribution by rearranging bins (figure 5.8) leads to new and unphysical neighbor relations (e. g. between bins C and D) where a curvature

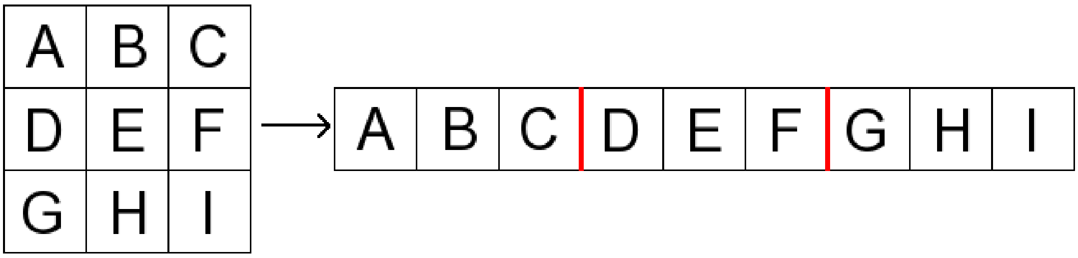

Figure 5.8: *Linearization of the binning scheme*

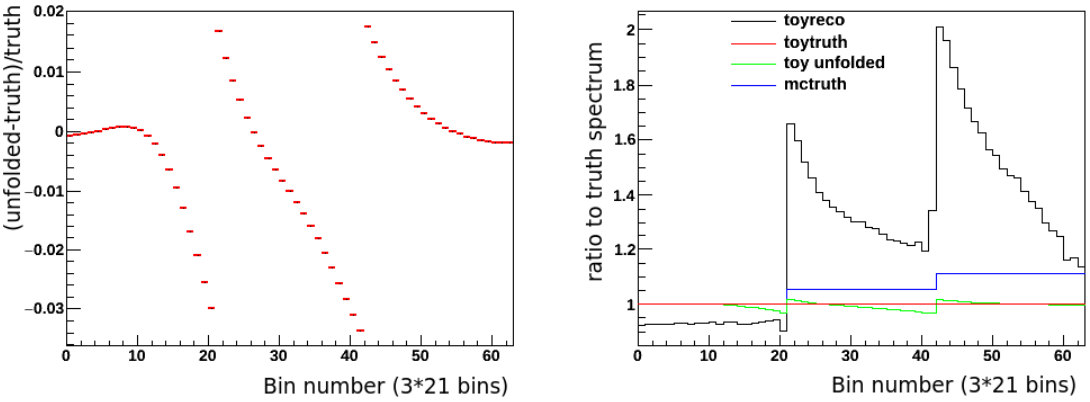

Figure 5.9: *An example plot of a relative bias with* $3{\cdot}21$ *bins, where the simulated MC truth distribution in the smaller dimension has been modified: The event yields in the first 21 bins are unchanged, the event yields in the middle 21 bins have been increased by 5%, the event yields in the last 21 bins have been increased by 10% ("mctruth" in the right plot). The unfolding has been overregularized (k too small) to make the effect more pronounced. "toyreco" is the simulated reconstructed spectrum in the simulated sample, "toy unfolded" the result of unfolding this sample with the bin migration matrix derived from the modified mctruth spectrum. Clearly visible is a large bias close to the category boundaries between bins 21 and 22 and between 42 and 43.*

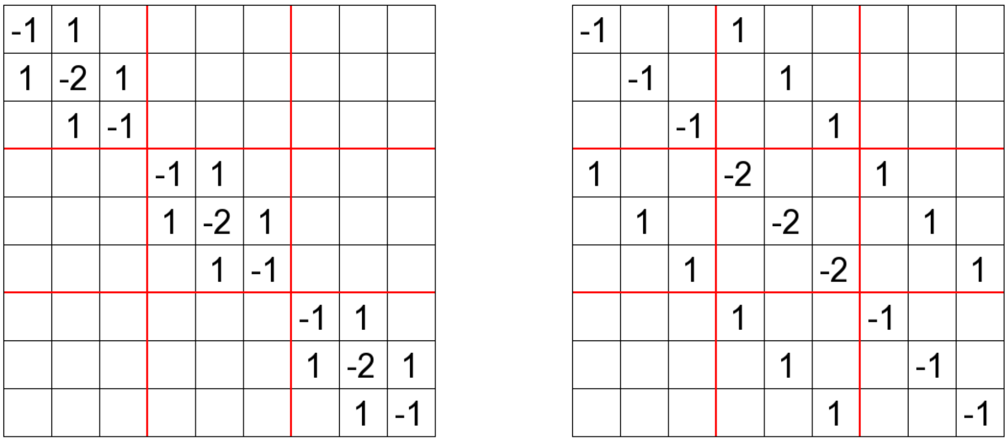

$$\left(\begin{array}{ccc|ccc|ccc}
-1 & 1 & & & & & & & \\
1 & -2 & 1 & & & & & & \\
 & 1 & -1 & & & & & & \\
\hline
 & & & -1 & 1 & & & & \\
 & & & 1 & -2 & 1 & & & \\
 & & & & 1 & -1 & & & \\
\hline
 & & & & & & -1 & 1 & \\
 & & & & & & 1 & -2 & 1 \\
 & & & & & & & 1 & -1
\end{array}\right)
\qquad
\left(\begin{array}{ccc|ccc|ccc}
-1 & & & 1 & & & & & \\
 & -1 & & & 1 & & & & \\
 & & -1 & & & 1 & & & \\
\hline
1 & & & -2 & & & 1 & & \\
 & 1 & & & -2 & & & 1 & \\
 & & 1 & & & -2 & & & 1 \\
\hline
 & & & 1 & & & -1 & & \\
 & & & & 1 & & & -1 & \\
 & & & & & 1 & & & -1
\end{array}\right)$$

Figure 5.10: *Curvature matrices for two-dimensional unfolding, A left, B right. The weighted sum yields the total curvature matrix*

calculation is not meaningful. Therefore, the approach leads to a wrong regularization if data and MC do not agree. This is demonstrated with a toy model with an overregularized example in figure 5.9, where the distribution in the smaller dimension has been changed to mimic possible deviations between data and MC. In addition, this approach does not take into account neighbor relations in the second dimension. In order to use SVD unfolding for multi-dimensional distributions, it is necessary to adjust the curvature matrix. This is shown for two dimensions here, extensions to more dimensions can be done in the same way. The new curvature matrix has to consider curvature in dimension 1 and curvature in dimension 2. In general, one of them will require more regularization, therefore it is advisable to assign a weight to the different curvatures. The matrix is used together with the rearranged binning as shown in figure 5.8.

The "one-dimensional" curvature matrix C for n bins can be described as

- $C_{ij} = 1$ for $|i - j| = 1$
- $C_{ij} = -1$ for $i = j$ and $(i = 0$ or $i = n - 1)$
- $C_{ij} = -2$ for $i = j$ and $i \neq 0$ and $i \neq n - 1$
- $C_{ij} = 0$ otherwise

where the indices i and j run from 0 to $n - 1$.

The "two-dimensional" curvature matrix C for $n \cdot m$ bins is the sum of two "one-dimensional" matrices.

- $B_{ij} = 1$ for $|i - j| = 1$, $\lfloor \frac{i}{m} \rfloor = \lfloor \frac{j}{m} \rfloor$
- $B_{ij} = -1$ for i=j, $i \bmod m = 0$ or $i \bmod m = m - 1$
- $B_{ij} = -2$ for i=j, $i \bmod m \neq 0$ and $i \bmod m \neq m - 1$

- $B_{ij} = 0$ otherwise

Here $\lfloor x \rfloor$ is the floor function.

- $D_{ij} = 1$ for $|i - j| = m$
- $D_{ij} = -1$ for $i = j$, $i < m$ or $i \geq m(n-1)$
- $D_{ij} = -2$ for $i = j$, $i \geq m$ and $i < m(n-1)$
- $D_{ij} = 0$ otherwise

To allow a different regularization strength for different dimensions, a weighted sum is used with the weight v: $C = vB + (1-v)D$. The ideal weight depends on the analysis, as discussed below. Assigning two separate weights to the individual matrices is not necessary as the regularization strength provides an overall scaling of the sum.

5.8.3 Application to the analysis

The analysis presented in this thesis evaluates the doubly-differential cross sections in the number of jets and one additional variable, for several choices of the additional variable. Observables that require two jets are also studied, but only in the inclusive category of at least two jets which does not require a two-dimensional unfolding procedure. Only the two-dimensional unfolding is considered in the following paragraph.

The binning (see table 5.3) has 11 to 25 bins for the different observables. Each observable is studied in the exclusive 0 jet, 1 jet and 2 jet categories (if applicable – as an example, p_T of the first jet cannot be studied in the 0 jet category) and in the inclusive 3 jet categories. This leads to 11 to 100 bins for the observables. For unfolding, the bins are linearized in the scheme "[all bins with 0 jets][all bins with 1 jet][all bins with 2 jets][all bins with $\geq$3 jets]". Toy studies show that a regularization in the number of jets is not advisable as it leads to a bias without avoiding larger statistical uncertainties after unfolding. This is also motivated by physics, as the MC description of the number of jets is not expected to be very accurate. Therefore, the weight v is chosen to be 1, regularization is used in the distribution of the other variable only.

Estimating biases

The regularization leads to a bias that depends on the discrepancy between MC shape and true distribution. This has to be taken into account as systematic uncertainty.

Several steps are performed to estimate the bias, based on the original MC sample: First, a distorted sample with a different "true" spectrum is produced, using one of the 11 variations described below. The sample is then scaled to the expected number of events in data, and statistical fluctuations are added in the way they are expected in data with its smaller sample size. Based on this, a (simulated) reconstructed spectrum is generated, using the bin migration from the original MC sample. This simulated sample is then unfolded with the original MC sample, and the difference between the unfolding result and the underlying “true” spectrum is calculated. An unfolding bias leads to a systematic difference between the two spectra, while statistical fluctuations added in the production of the simulated reconstructed spectrum are random. Therefore, this procedure is repeated 100 times with different random seeds for the added statistical fluctuations. For each bin the average difference is taken as estimate of the unfolding bias for the tested variation.

As the disagreement between the data and MC distributions is not known in advance, different variations are tested. They mimic realistic possible differences between simulation and data. A simulation-to-data ratio that varies significantly from bin to bin can lead to larger biases, but with the spectra measured in the analysis this is not expected. The main expected deviation is a steeper or flatter spectrum in most variables. Other deviations considered are parabolic (the bins close to the center have the largest deviation) or a wrong distribution in the number of jets. All those deviations are simulated with a bin-by-bin variation of toy data.

List of tested variations:

1. For each jet category, keep the first bin content (in the variable considered) the same, increase the last bin content by +100%, increase all bins in between linearly based on the bin number (e. g. +0%, +5%, +10%, ..., +100% for the diphoton mass).
2. Same as above, but only up to +75% for the last bin
3. Same as above, but only up to +50%
4. Same as above, but only up to +25%. These weaker deviations test the linearity of the biases with the size of the MC to data differences.
5. No modification at all, as cross-check
6. Same as (1), but with a decrease in bin contents, up to -25% for the last bin
7. Same as (6), but up to -50%. This is a reduction by a factor of up to 2, similar to the increase by a factor of 2 by variation (1).
8. A variation in the Njet distribution only. All bins in the first jet category are unchanged, all bins in the last jet category are increased by 50%, in between (if more than two categories are present) the interpolation is linear. As an

example, for diphoton variables the 1 and 2 jet bins are increased by $\frac{1}{3}50\%$ and $\frac{2}{3}50\%$ respectively.

9. Similar to (8), but the last jet category is reduced by 30%, and those in between (if present) are reduced accordingly.

10. The distorted truth distribution divided by the original MC truth distribution follows a parabola, where the central bin (e.g. the 11th for $m_{\gamma\gamma}$) gets increased by 50%, while the outermost bins stay unchanged, and everything in between follows the parabolic shape.

11. Similar to (10), but the central bin is reduced by 30%, and the other bins correspondingly.

An overall scaling of toy data does not change the bias of the unfolding result, therefore it is not necessary to modify the first bins (outer bins for parabolic bias) stronger while leaving the last bin (central bins) unchanged.

Comparisons of unfolded spectra with MC predictions showed significant deviations, sometimes with notable differences between neighbor bins. The ratio between MC prediction and unfolded spectra was also tested as toy variation, and the resulting bias was added to the biases discussed above. The deviations are shown in section 5.10, the resulting bias is shown in appendix A.3 and A.4.

Choice of regularization strength

SVD unfolding has a free parameter k that determines the strength of regularization: the regularization strength τ is set to the magnitude of the k'th singular value. Therefore, k can range from 1 to the number of bins, where smaller values lead to a stronger regularization on the unfolded distribution, which leads to smaller statistical uncertainties but (in general) larger biases. In order to choose the ideal k, the statistical uncertainties and the expected bias in all bins is combined to a single figure of merit (FoM). This FoM is then evaluated for different values of k.

The FoM should reflect the goals of the analysis to get small overall uncertainties in most bins. The event numbers in different bins can vary by orders of magnitude. Correspondingly, the size of the uncertainties is different. In order to avoid undue weight from bins with low statistics, the cubic root of the relative uncertainty in toy studies is used, and summed over all bins. As the choice of the cubic root is arbitrary, the square root and the fourth root have been tested, this does not change the results. Similarly, the cubic root of the magnitude of the expected bias for the tested deviations between MC and toy (see 5.8.3) is evaluated in each bin and summed over all bins. The FoM is then a weighted sum of those two numbers. While statistical uncertainties get a weight of 1, the bias gets a weight of 4 to be conservative.

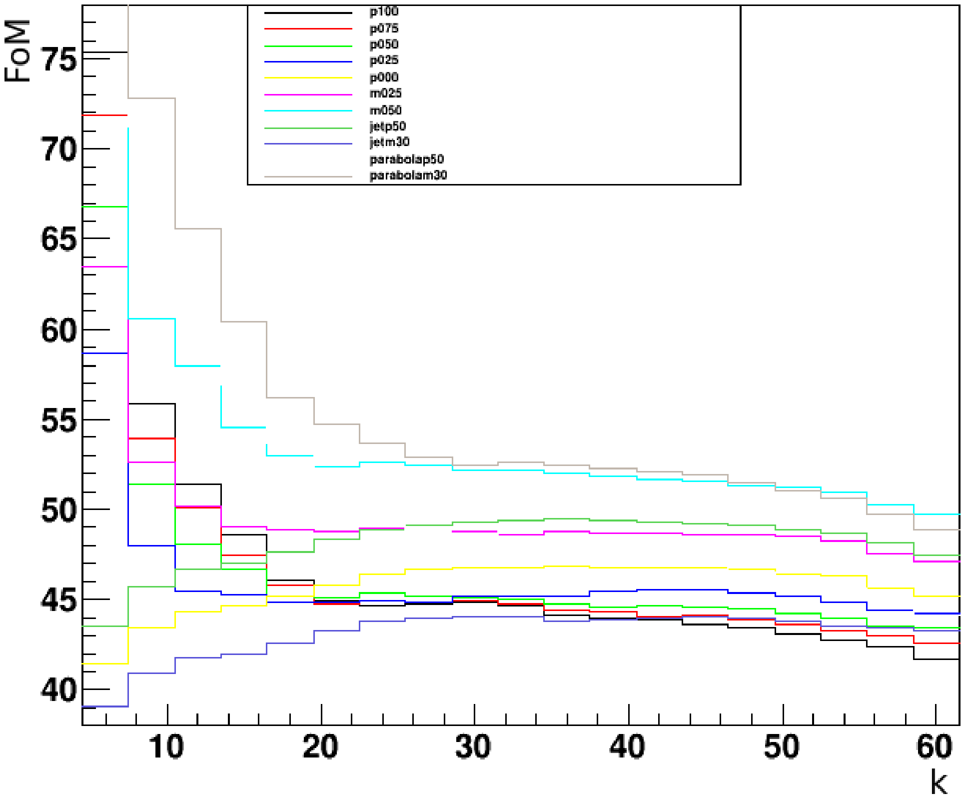

Figure 5.11: *Figure of merit for $\Delta R_{\gamma 1 j1}$ unfolding for different choices of regularization strength k, for all 11 tested MC to data deviations. $k = 45$ was chosen as 3/4 the number of bins.*

The FoM is plotted for all tested deviations between MC and toy, and the largest FoM (the worst case among the tested deviations) is evaluated for each regularization strength. For variables that show a clear minimum in the worst-case FoM, a regularization strength close to this minimum was chosen, but with the additional requirement that the estimated unfolding bias uncertainty has to be small compared to other systematic uncertainties (see A.3 and A.4). For variables where the worst-case FoM does not depend strongly on the regularization strength, k is chosen to be 3/4 of the number of bins, as this avoids the k range with a large bias, while still providing some regularization.

Figure 5.11 shows how the FoM depends on the regularization strength and the 11 tested biases for $\Delta R_{\gamma 1 j1}$.

Variable	Bins	Min jets	Max jets	Total bins	k
$m_{\gamma\gamma}$	21	0	3	84	63
$p_{\mathrm{T}}^{\gamma\gamma}$	21	0	3	84	63
$\Delta\phi_{\gamma\gamma}$	25	0	3	100	75
$\cos\theta^*_{\gamma\gamma}$	25	0	3	100	75
m_{jj}	23	2	3	46	21
$p_{\mathrm{T},jj}$	16	2	3	32	15
$\Delta\phi_{jj}$	18	2	3	36	24
Δy_{jj}	16	2	3	32	28
$\Delta S_{\gamma\gamma jj}$	20	2	3	40	16
$\Delta R_{\gamma 1 j1}$	20	1	3	60	45
$\Delta R_{\gamma 1 j2}$	20	2	3	40	30
$\Delta R_{\gamma 2 j1}$	20	1	3	60	45
$\Delta R_{\gamma 2 j2}$	20	2	3	40	30
p_{T}^{j1}	13	1	3	39	27
p_{T}^{j2}	12	2	3	24	13
p_{T}^{j3}	11	3	3	11	7

Table 5.9: *A list of all variables, with the number of bins in this variable and the jet categories considered for it, together with the regularization strength k. In general, the values for k are roughly half to three quarters the number of bins, smaller numbers indicate a benefit from a stronger regularization, the larger numbers for the diphoton variables indicate that regularization can be weaker as photons are measured with a better precision than jets.*

5.8.4 Derivation of inclusive jet categories

All the analysis steps described use exclusive jet categories, apart from the 3-jet category, which is inclusive (≥ 3 jets). To reduce the impact of jet-related uncertainties, and to improve comparisons with some theoretical predictions, it can be interesting to measure inclusive jet categories. The unfolding method described does not work with inclusive categories, as it assumes that the individual bins are disjoint. The measurement of the exclusive categories allows a derivation of inclusive categories. The central cross section values can be added directly. For the uncertainties, the covariance matrix Σ provided by the unfolding contains the necessary information to take correlations between bins into account. As an example, to get the uncertainty on the sum of bins i and j into bin a of a new covariance matrix, the four relevant matrix entries are added: $\Sigma'_{a,a} = \Sigma_{i,i} + \Sigma_{i,j} + \Sigma_{j,i} + \Sigma_{j,j}$. The uncertainty is the square root of the diagonal entries of the covariance matrix. This procedure is done for every individual uncertainty to keep the information about the relative importance of the individual uncertainties.

The jet-related uncertainties, described in the following section, show a strong anticorrelation between the jet bins. As a result, their influence on the total uncertainty in inclusive jet categories is much smaller than for exclusive jet categories.

5.9 Systematic uncertainties

Many systematic uncertainties have to be considered in the analysis. They are described in the following subsections. Unless indicated otherwise, all individual uncertainties are estimated by varying a parameter up and down, and considering the corresponding up- and downwards deviation of the cross section separately. If both upwards and downwards variation change the cross section in the same direction, the larger change is used as single-sided uncertainty. All uncertainty components are then added in quadrature, separately for up and down.

The breakdown of the systematic uncertainties, the statistical and the total uncertainty bin-by-bin is shown in appendix A.3 (exclusive jet categories) and A.4 (inclusive jet categories) for all observables, examples are shown in figure 5.12.

In most cases, the dominant uncertainty comes from the jet background subtraction in the 0 and 1 jet categories, while the jet energy scale is the dominant uncertainty for the 2 and at least 3 jet categories. The systematic uncertainty on the JVF selection is dominant where low-energetic jets have a large impact on the observable, for example for the $\Delta S_{\gamma\gamma jj}$ observable at low separation between diphoton and dijet system. A different MC description of the JVF selection changes the estimate of the number of pile-up jets that would get selected and the number of signal jets being rejected, moving events between the 0- and 1-jet category. The uncertainty from the electron background subtraction is important in the diphoton invariant mass spectrum around the Z peak.

5.9.1 Background subtraction

The systematic uncertainties arising from the background subtraction are described in more detail in sections 5.3 and 5.4. For both background subtraction methods, the main systematic uncertainty arises from the definition of the “non-tight” control region in the photon identification. Three alternatives to the default choice are tested. The whole background subtraction is repeated with the different options, and the resulting spectra are unfolded to produce cross-section estimates for the different choices of control regions. The maximum of the deviations is taken as a systematic uncertainty, separately for changes up and down in the unfolded spectra. This uncertainty is taken to be fully correlated between the different bins.

2x2DSB method

Apart from the definition of the non-tight control region, uncertainties arise from the photon isolation shape and the determination of the data-driven isolation efficiencies, as described in section 5.3.1.

For the electron background subtraction, an uncertainty on the fake rates has to be considered.

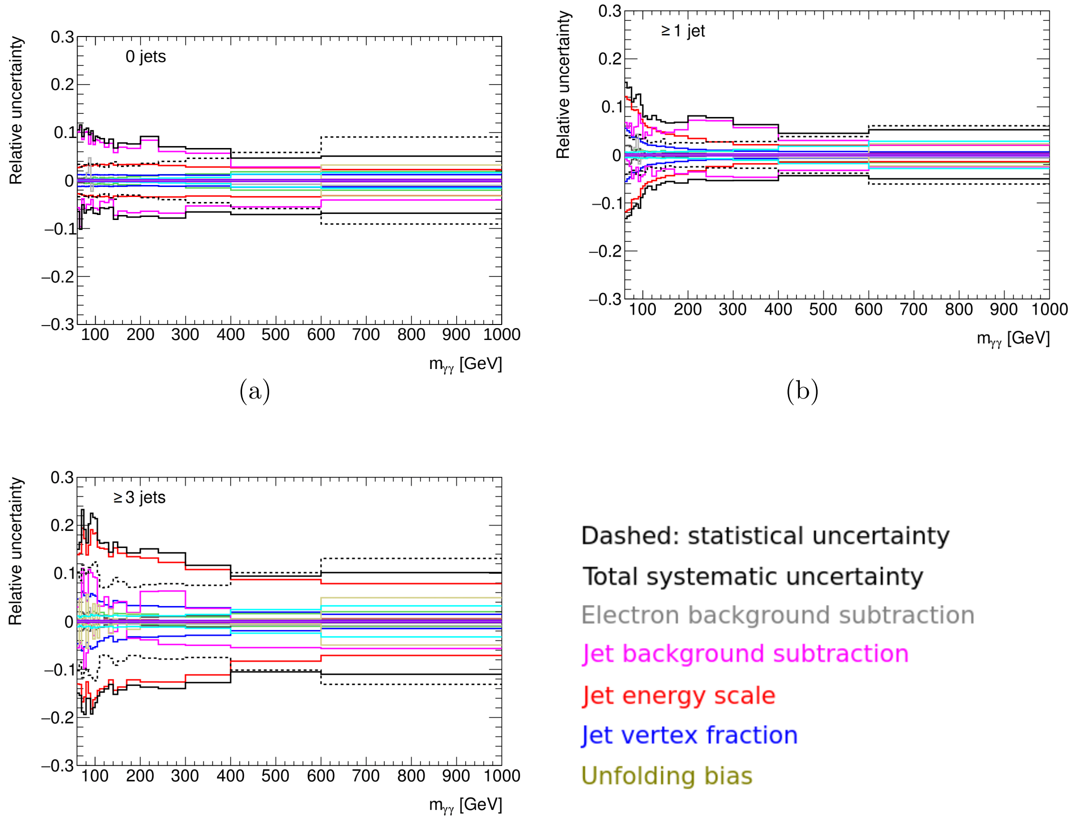

(a) (b)

(c) (d)

Figure 5.12: *Breakdown of all systematic uncertainties for the* $m_{\gamma\gamma}$ *spectrum in the exclusive 0-jet category (a), the inclusive* ≥ 1*-jet category (b), and the inclusive* ≥ 3*-jet category (c). Clearly visible is the different impact of the jet energy scale (in red). The statistical uncertainty is significant in the* ≥ 3*-jet category. Only the main uncertainties are included in the legend (d).*

4x4 matrix method

Apart from the definition of the non-tight control region, the definition of the anti-isolation region leads to a systematic uncertainty, as described in section 5.4.3. The electron background contribution is varied up and down within its uncertainty.

Type	dominant?
Background subtraction	
Definition of “non-tight”	yes
Photon anti-isolation region	no
Electron background subtraction	at Z peak
Unfolding procedure	
MC statistics	no
Unfolding bias	no
Monte Carlo detector description	
Photon energy scale	no
Photon energy resolution	no
Photon tight ID scale factors	no
Jet energy scale	with 2-3 jets
Jet energy resolution	no
JVF signal efficiency uncertainty	For low jet p_T
Jet definition and pileup	at $\Delta\phi_{\gamma\gamma} \approx \pi$
Trigger efficiency	no
Luminosity	
Luminosity	no

Table 5.10: *Overview of systematic uncertainties in the analysis.*

5.9.2 Unfolding procedure

Regularization in the unfolding avoids inflating statistical uncertainties, but the result then depends on the quality of the Monte Carlo samples: deviations in the shape between MC and data lead to a bias in the unfolding procedure.

As described in section 5.8.3, 11 different deviations between MC and data are tested, plus a deviation describing the difference between the observed unfolded spectra and the MC prediction. For every deviation, the unfolding result is compared to the simulated data input for 100 simulations, and the average over the simulation results is taken. As conservative estimate, the largest (out of 12) average (over the 100 simulations) deviation in any direction is used as systematic uncertainty both up and down.

5.9.3 Monte Carlo detector description

As the observed distributions in data are unfolded via Monte Carlo, an inaccurate MC description of the detector leads to deviations in the unfolded distribution. Those possible deviations are encoded in several different parameters. To account for those, the bin migration matrices are rederived with the parameters varied up and down, respectively, within their uncertainty.

Photon energy scale and resolution

The ATLAS e/gamma group derived the calibration and resolution corrections and assessed the uncertainties on the photon energy scale and resolution [46].

The model used in this analysis includes 29 parameters, summarized in table 5.11. Each parameter is varied up and down. The full correlation model, which is not used for this analysis, contains 56 parameters and decorrelates more of the material uncertainties and the E_1/E_2 scale uncertainty in 0.2 bins in η.

Source of systematic uncertainty	Simplified model	Parameters
Method	fully correlated	1
LAr HG/MG miscalibration	fully correlated	1
L1 gain	fully correlated	1
E_1/E_2 scale	decorrelated barrel/end-cap	2
LAr E_1/E_2 calibration	decorrelated barrel/end-cap	2
PS scale	decorrelated barrel/end-cap	2
LAr E_1/E_2 modeling for $e/\ \gamma_{\mathrm{unconv}}$	decorrelated barrel/end-cap	2
Material in inner detector	decorrelated in four η bins	4
Material in cryostat	decorrelated barrel/end-cap	2
Material in calorimeter	decorrelated barrel/end-cap	2
LAr E_1/E_2 modeling for γ_{unconv}	decorrelated barrel/end-cap	2
LAr E_1/E_2 modeling for e	fully correlated in end-cap	1
Lateral leakage γ_{unconv}	fully correlated	1
Lateral leakage γ_{conv}	fully correlated	1
Conversion inefficiency	fully correlated	1
Conversion fake rate	fully correlated	1
Conversion radius	fully correlated	1
Pedestal	fully correlated	1
GEANT4 simulation	fully correlated	1
Total number of parameters		29

Table 5.11: *Simplified correlation model of the photon energy scale uncertainties for two photons.*

In addition to the photon energy scale, the energy resolution has corresponding uncertainties as well [46]. There are seven variations, each varied up and down:

- uncertainty associated to the measured Z boson peak, evaluated by smearing of the Z peak;
- uncertainty on the stochastic term in the detector resolution (see section 2.4.1);
- uncertainty on the material budget in the inner detector, liquid argon calorimeter, the transition region between the barrel and end-cap and the cryogenic services;

- uncertainty associated to the modeling of pile-up.

Photon tight ID scale factors

To improve the description of photons in MC, the simulated shower shapes are shifted to match those observed in data, as described in section 4.4.3. This alone does not give a full agreement between photon identification efficiency in MC and data. The photon identification efficiency in data is measured with three different methods, described in [51]. Efficiency scale factors as function of p_T and η are introduced to adjust the simulated efficiency to the measured values. These scale factors are applied to all MC simulations. They have systematic uncertainties from the efficiency measurements which have to be taken into account. The unfolding was repeated with samples where the scale factors were varied up and down according to their uncertainties.

Jet energy scale and resolution

To account for uncertainties on the jet energy scale and resolution calibration, a model with 65 parameters was developed for the jet energy calibration in ATLAS. This analysis is using a simplified jet calibration with a reduced set of parameters, according to the recommendations of the jet/E_T^{miss} group. It contains 14 parameters for the jet energy scale [81]:

- six parameters coming from the reduction of the in-situ analyses parameters;
- two parameters from η intercalibration, depending on the MC modeling and statistics;
- one parameter from the behavior of high-p_T jets in the propagation of single hadron uncertainties to jet uncertainties;
- one parameter from the MC non-closure between the different MC samples used for calibration, with the main change being the amount of material in the detectors;
- four parameters from pile-up, three of these are dependent on the number of primary vertices and μ (number of interactions per bunch crossing).

In addition to the energy scale, the jet energy resolution estimate in MC could deviate from the resolution in data. The data is unfolded with a sample where the resolution was made worse by one standard deviation of the uncertainty, the difference between the unfolded nominal spectra and the spectra from this test is symmetrized and used as systematic uncertainty.

JVF signal efficiency uncertainty

The efficiency of the JVF selection criterion of JVF > 0.5 for signal jets was studied in [72], the MC response matrices are re-calculated with the efficiency varied up and down within its uncertainty given there.

Jet definition and pile-up

Despite the JVF selection and the minimal transverse energy requirements, about 10% of the selected jets come from a different primary vertex than the remaining objects in the event. Following the approach used in [82], at the reconstruction level in MC 35% of pileup jets are randomly removed. The unfolding is repeated with the derived response matrices. As there is no meaningful way to add pileup jets to explore the effect of an underestimate of the contribution of pileup jets, the uncertainty from removing the jets is symmetrized: The observed absolute difference is taken as systematic uncertainty in both directions.

Trigger efficiency

The trigger efficiency has been determined as $98.66\% \pm 0.19\%$. It is considered as constant and fully correlated uncertainty in all bins. The influence on the total systematic uncertainty is negligible everywhere.

5.9.4 Luminosity

The exact central value for the luminosity used to obtain the cross sections is 20246.2 pb^{-1}. The integrated luminosity was measured by the luminosity group as 20.25 fb^{-1} with an uncertainty of ±1.9% [83]. The luminosity uncertainty is fully correlated across all measured cross-sections.

5.10 Results

Spectra after background subtraction and unfolding are shown in this section. Data is shown in black, red error bars are the statistical uncertainty, the black error bars are the statistical and systematic uncertainties added in quadrature, excluding the luminosity uncertainty. The systematic uncertainty is larger than the statistical uncertainty everywhere apart from a few bins with a very low number of events.

All measured spectra are compared to SHERPA (blue histograms) and PYTHIA (red histograms) predictions. The exclusive 1-jet and 2-jet spectra are compared to GOSAM (green histograms) as well. For the ratio plots, the same y-axis scale is used for both SHERPA and PYTHIA for all jet categories of a given observable. As PYTHIA underestimates the event yields in the 2-jet and $\geq$ 3-jet category significantly, this can lead to empty ratio histograms in these jet categories.

The 16 observables with all jet categories lead to 34 exclusive ($= n$ jets) and 42 inclusive ($\geq n$ jets) spectra. Due to the large number of histograms, only a few representative histograms are shown here, they are discussed in the image captions. A full list of all results can be found in appendix A.1 for exclusive jet categories and appendix A.2 for inclusive jet categories.

In general, the PYTHIA sample underestimates the number and transverse momentum of jets, and their distance to other jets and photons. This is expected, as the sample does not include jets in the matrix element. Jets from parton showers tend to be low-energetic and close to other objects in the events. Despite an underestimated overall event yield, in the shape of spectra of the diphoton observables PYTHIA has a similar or better agreement with data compared to SHERPA.

Both SHERPA and PYTHIA show larger deviations for very low-energetic events, where a leading order calculation does not accurately describe the dynamics of the collision process and details of the parton showering process become important.

In general, GOSAM predicts the shape of the distributions well, but overestimates the total cross section. A notable exception is $\Delta R_{\gamma 1 j1}$ in the 1-jet region for small separations between leading photon and leading jet. A fixed-order calculation has a very small phase space for this region due to momentum conservation. SHERPA and PYTHIA can provide a more accurate prediction here, as low-energetic parton showers can contribute to the momentum balance. In the 2-jet category, momentum conservation is not limiting the phase space any more, and GOSAM provides an accurate description of the observable.

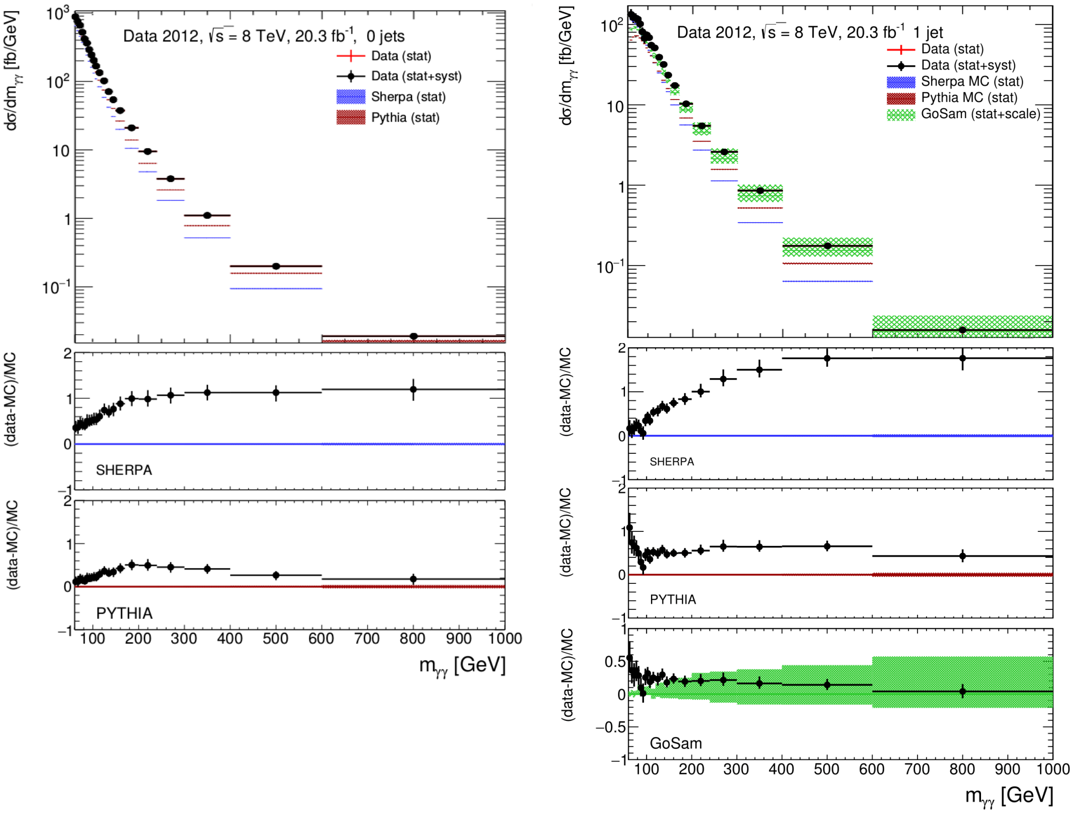

(a) (b)

Figure 5.13: *Measured spectrum of $m_{\gamma\gamma}$ in the 0-jet and 1-jet category. Experimentally, the diphoton mass leads to small relative uncertainties, while previous studies show that the steeply falling spectrum makes theoretical predictions challenging.* Sherpa *underestimates the signal yield for large $m_{\gamma\gamma}$.* Pythia *shows a better agreement, especially in the 0-jet category.* GoSam *has the best prediction for large $m_{\gamma\gamma}$, but shows a reasonable agreement for low values as well.*

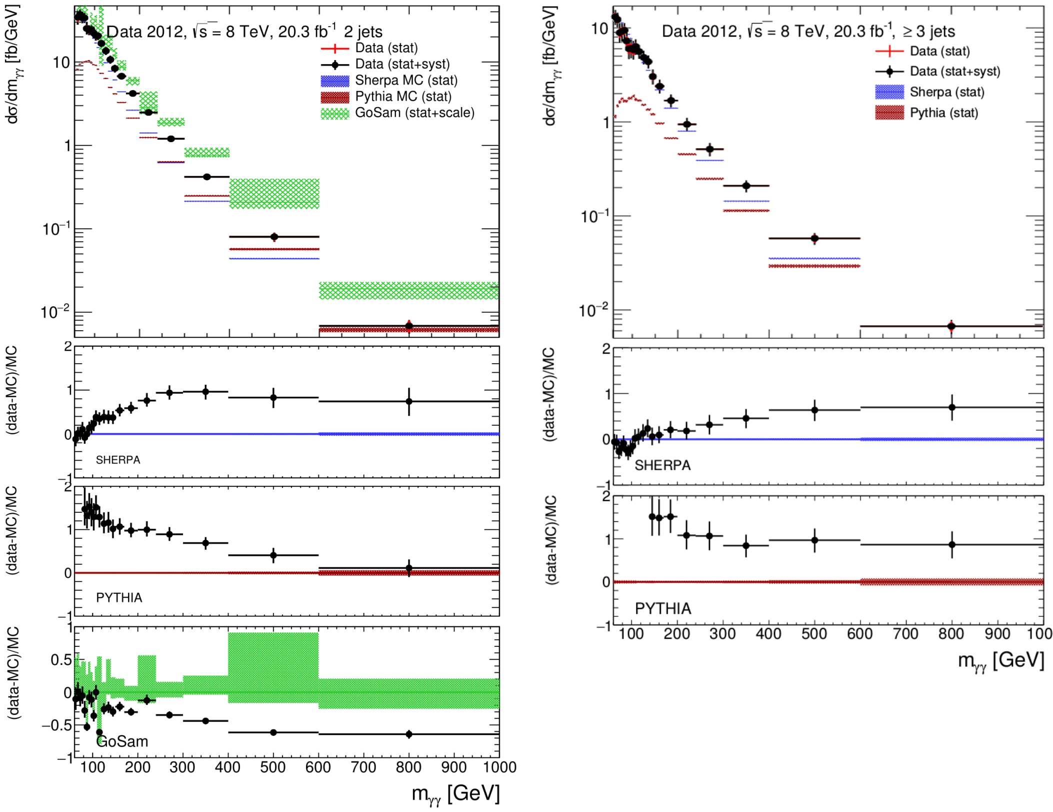

(a) (b)

Figure 5.14: *Measured spectrum of $m_{\gamma\gamma}$ in the 2-jet and $\geq$ 3-jet category. As expected,* PYTHIA *underestimates the number of jets, especially for low-energetic events where parton showers do not lead to jets of sufficient energy to pass the selection.* SHERPA *describes the low $m_{\gamma\gamma}$ region well, but again underestimates the cross section for large $m_{\gamma\gamma}$ in the 2-jet category.* GOSAM *overestimates the cross section in the 2-jet category, but describes the shape accurately.*

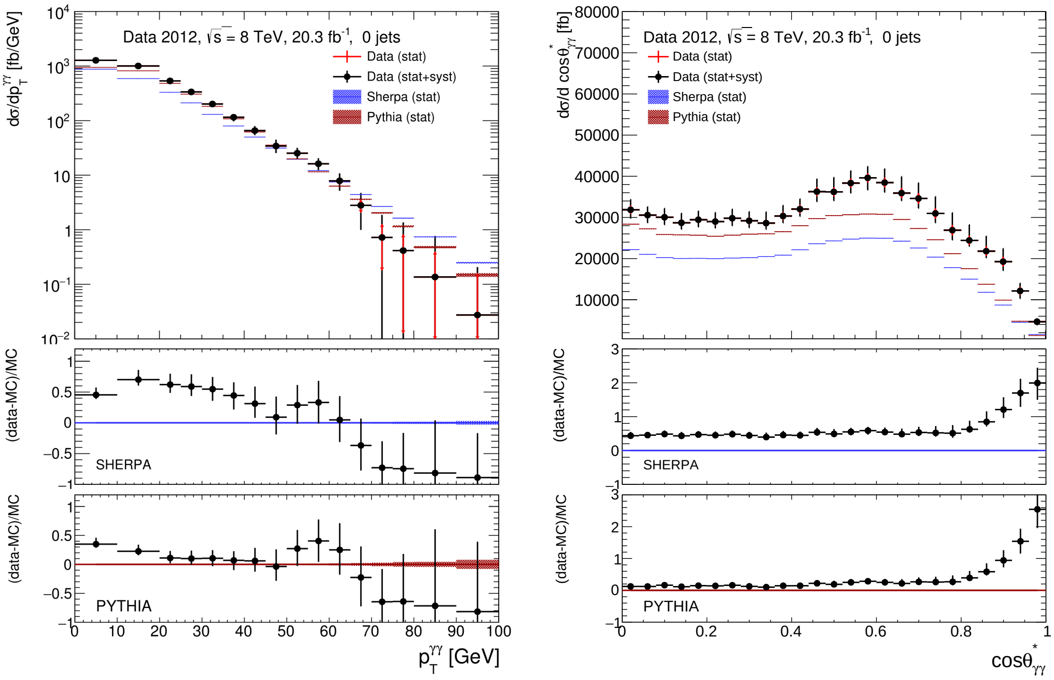

(a) (b)

Figure 5.15: *Measured spectrum of* $p_{\mathrm{T}}^{\gamma\gamma}$ *in the 0-jet category (a). Conservation of momentum does not allow large* $p_{\mathrm{T}}^{\gamma\gamma}$ *values without a jet going in the opposite direction. Only the first few bins have events, empty bins are not shown.* Sherpa *and* Pythia *have a similar description, underestimating the cross section at low* $p_{\mathrm{T}}^{\gamma\gamma}$*. This can be understood with subfigure (b), showing* $\cos\theta^*_{\gamma\gamma}$ *in the 0-jet category, where* $\cos\theta^*_{\gamma\gamma} \approx 1$ *is associated to a low* $p_{\mathrm{T}}^{\gamma\gamma}$*.*

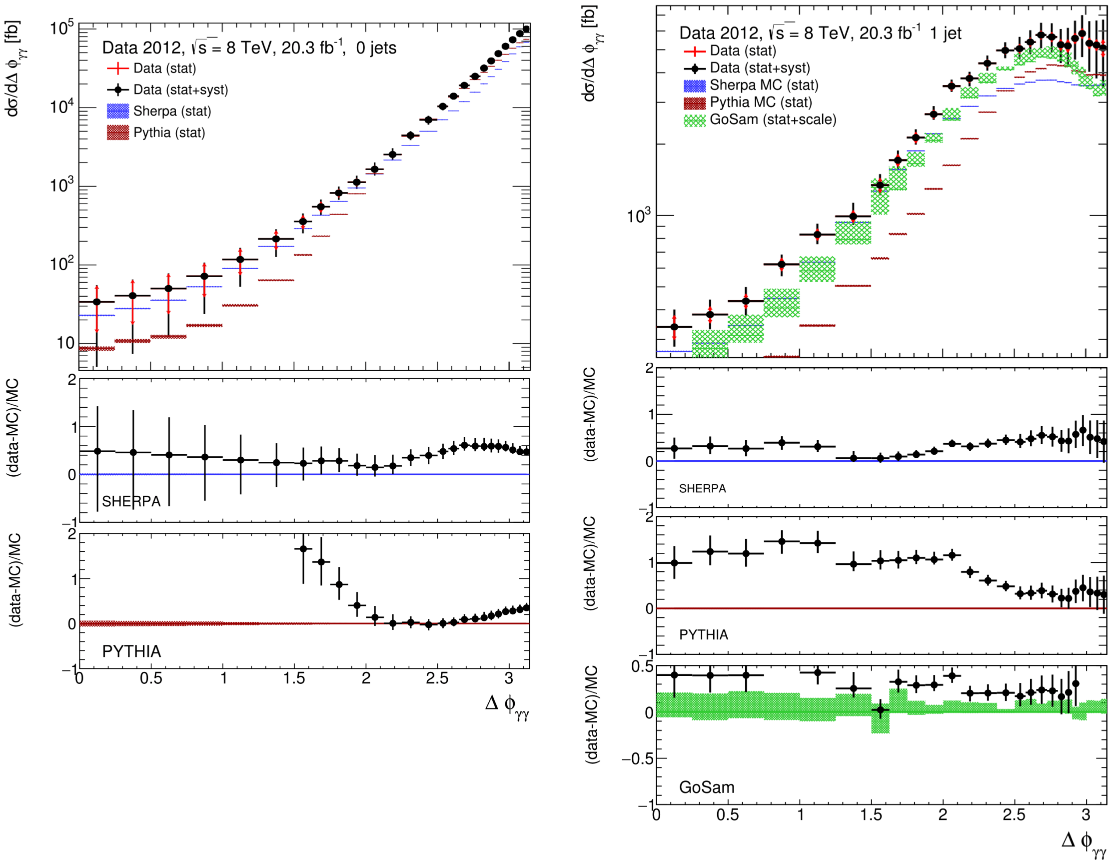

(a) (b)

Figure 5.16: *Measured spectrum of $\Delta\phi_{\gamma\gamma}$ in the 0-jet category (a). Here large differences between* Sherpa *and* Pythia *are visible.* Sherpa *describes the spectrum of the polar angle difference between the photons well, while* Pythia *with only photons in the hard process tends to have more back-to-back photons. In the 1-jet category (b), both* Sherpa *and* Pythia *describe the shape correctly,* Pythia *underestimates the total cross section.* GoSam *describes the shape well, but underestimates the number of back-to-back photons with an additional jet. This is an effect of the momentum balance in a fixed-order calculation, as a single additional jet requires that the photons cannot be exactly back-to-back.*

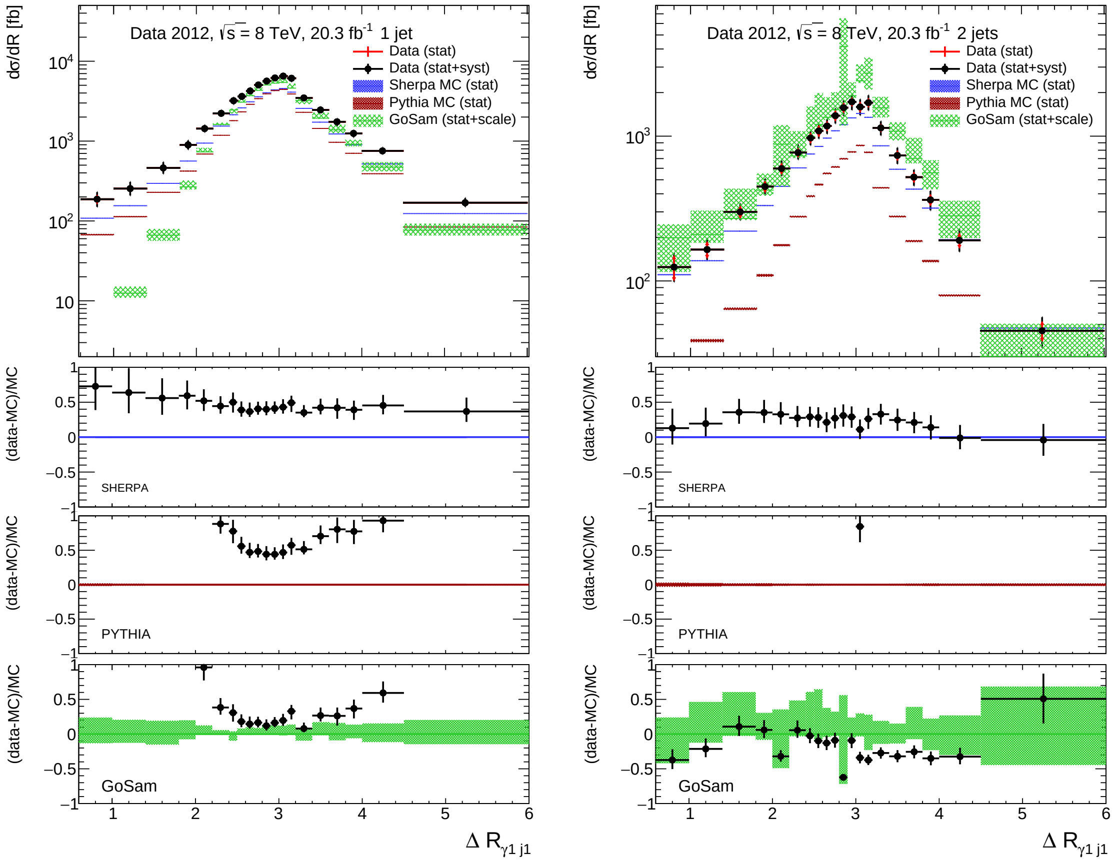

(a) (b)

Figure 5.17: *Measured spectrum of* $\Delta R_{\gamma 1 j1}$ *in the 1-jet category (a) and 2-jet category(2).* Sherpa *provides an accurate description in both cases. The limitations of fixed-order calculations like* GoSam *are visible in the 1-jet category. A small separation between leading photon and leading jet gives a very small phase space for conservation of transverse momentum, as the subleading photon and the subleading jet (going in the opposite direction) both have lower energies and there are no other objects in the event. In the 2-jet category, momentum balance is not a problem any more, and the description gets much more accurate.*

Chapter 6

Summary

6.1 Summary

The ATLAS experiment at the Large Hadron Collider has a broad physics program covering all aspects of nuclear and particle physics accessible at the LHC. Proton-proton collision data has been collected from 2010 to 2012 (Run 1) and since 2015 (Run 2). This thesis focuses on physics with photons. Their reconstruction and identification is discussed, and the re-optimization of the photon identification criteria for Run 2 is shown. A new set of selection cuts for the identification is developed. The re-optimization keeps a photon identification performance similar to Run 1 under the more challenging running conditions of Run 2.

The main part of the thesis presents the measurement of 16 differential cross sections in events with two photons as function of the number of jets in the event, based on $\sqrt{s} = 8$ TeV collisions in 2012 corresponding to an integrated luminosity of 20.3 fb^{-1}. The observables are sensitive to the dynamics of the diphoton system, the jet properties (especially with 2 jets), and the separations between photons and jets in the event. After selecting the photons and jets, the main background from jets getting reconstructed as photons is subtracted. A smaller background arising from electrons getting identified as photons is subtracted as well. The resulting event yields are unfolded to account for bin migration. To work with two-dimensional distributions, SVD unfolding originally designed for one-dimensional distributions, is generalized. It uses assumptions about the smoothness of the measured distributions relative to theoretical predictions to avoid artificial increases in statistical uncertainties. The efficiency of the event selection is evaluated and taken into account to estimate the cross section in each bin. All systematic uncertainties are evaluated. The largest uncertainties are the choice of a control region for the background subtraction and the uncertainty in the jet energy scale. Inclusive jet categories ($\geq n$ jets) are derived from the exclusive categories. This leads to large cancellations of jet uncertainties.

The measured cross sections are compared to predictions by Sherpa, Pythia and GoSam. The quality of the predictions differs significantly between the observables studied and the type of prediction, with no prediction leading to better results than others everywhere. Some of the observed discrepancies could be linked to the model used for the prediction: The Pythia sample studied did not have jets in the matrix element, as result the jet description is not very accurate. Both Sherpa and Pythia tend to underestimate the cross sections at high photon energies. GoSam predictions often match in the shape of the distribution, but have a constant offset in the predicted cross section. GoSam cannot describe the low $\Delta R_{\gamma 1 j1}$ region in the 1-jet category accurately, as expected for fixed-order calculations. Further work is necessary to study the origin of the other observed discrepancies.

Appendix A

Appendix

A.1 All measured distributions - exclusive categories

All distributions are compared to Sherpa and Pythia predictions. Spectra with 1 and 2 jets are compared to GoSam as well. As the 3-jet category is always inclusive, it is only shown in appendix A.2.

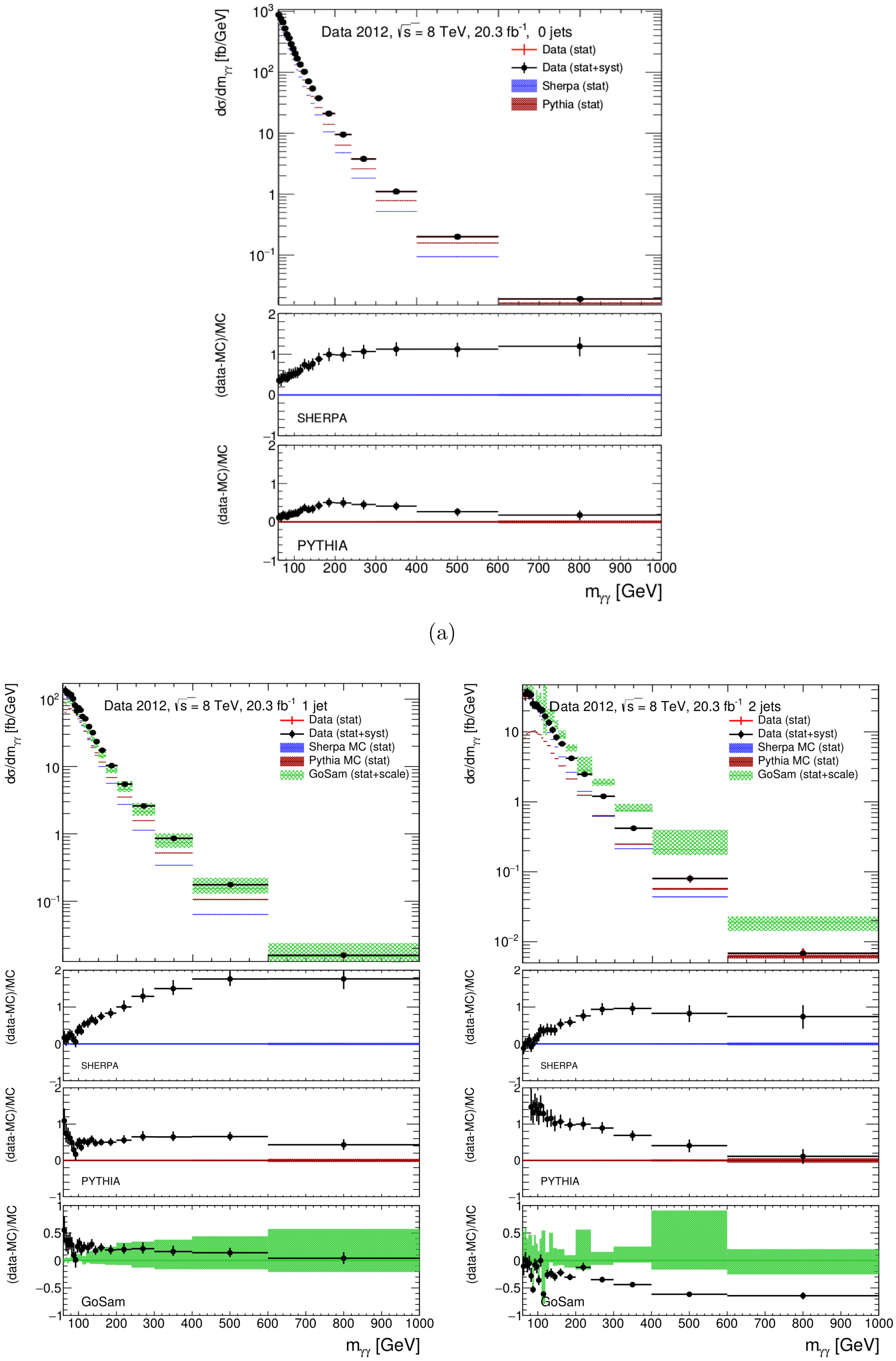

(a)

(b)

(c)

Figure A.1: *Cross sections as a function of the diphoton invariant mass for the 0-jet, 1-jet and 2-jet categories.*

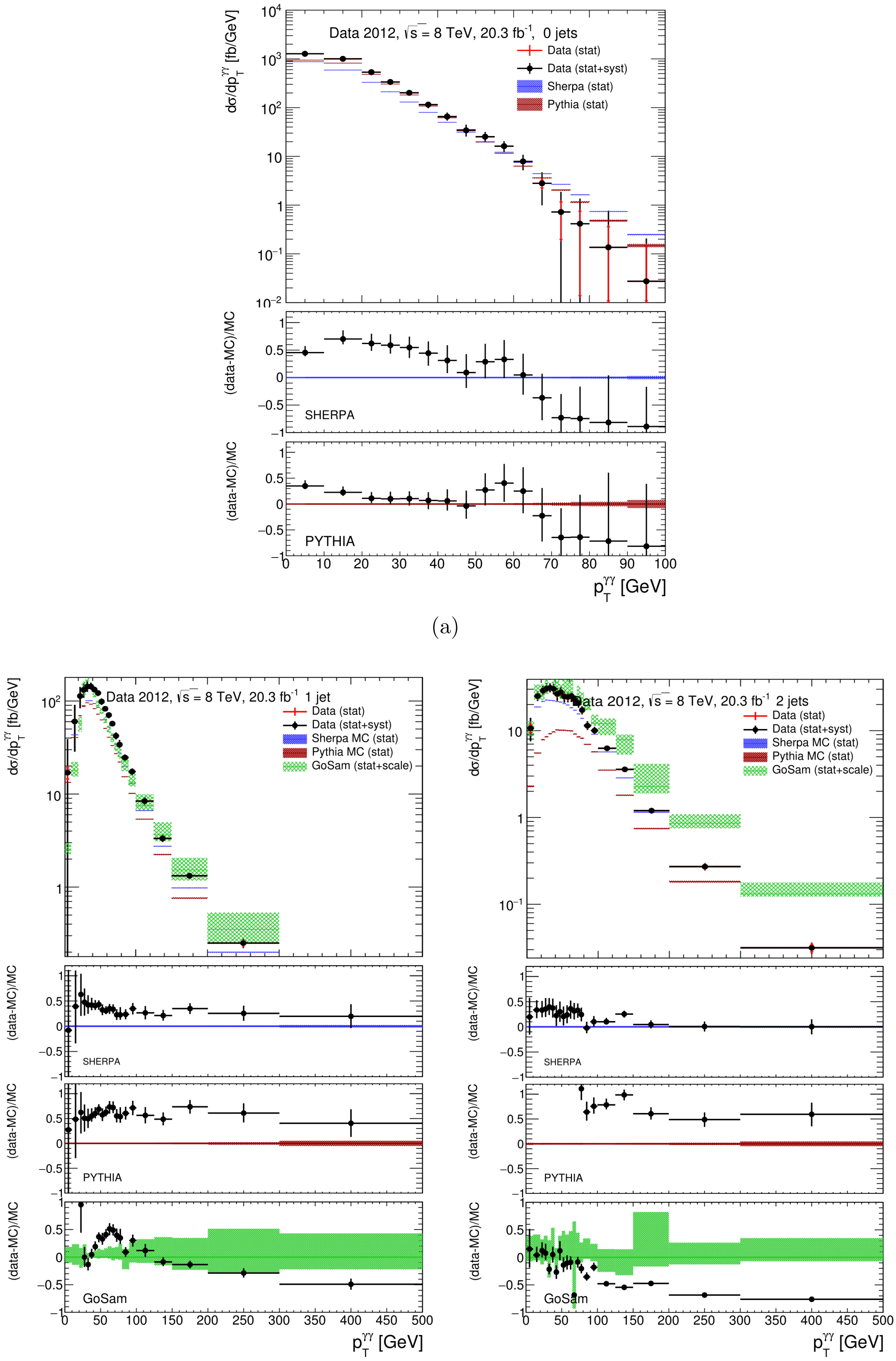

(a)

(b)

(c)

Figure A.2: *Cross sections as a function of the diphoton transverse momentum for the 0-jet, 1-jet and 2-jet categories.*

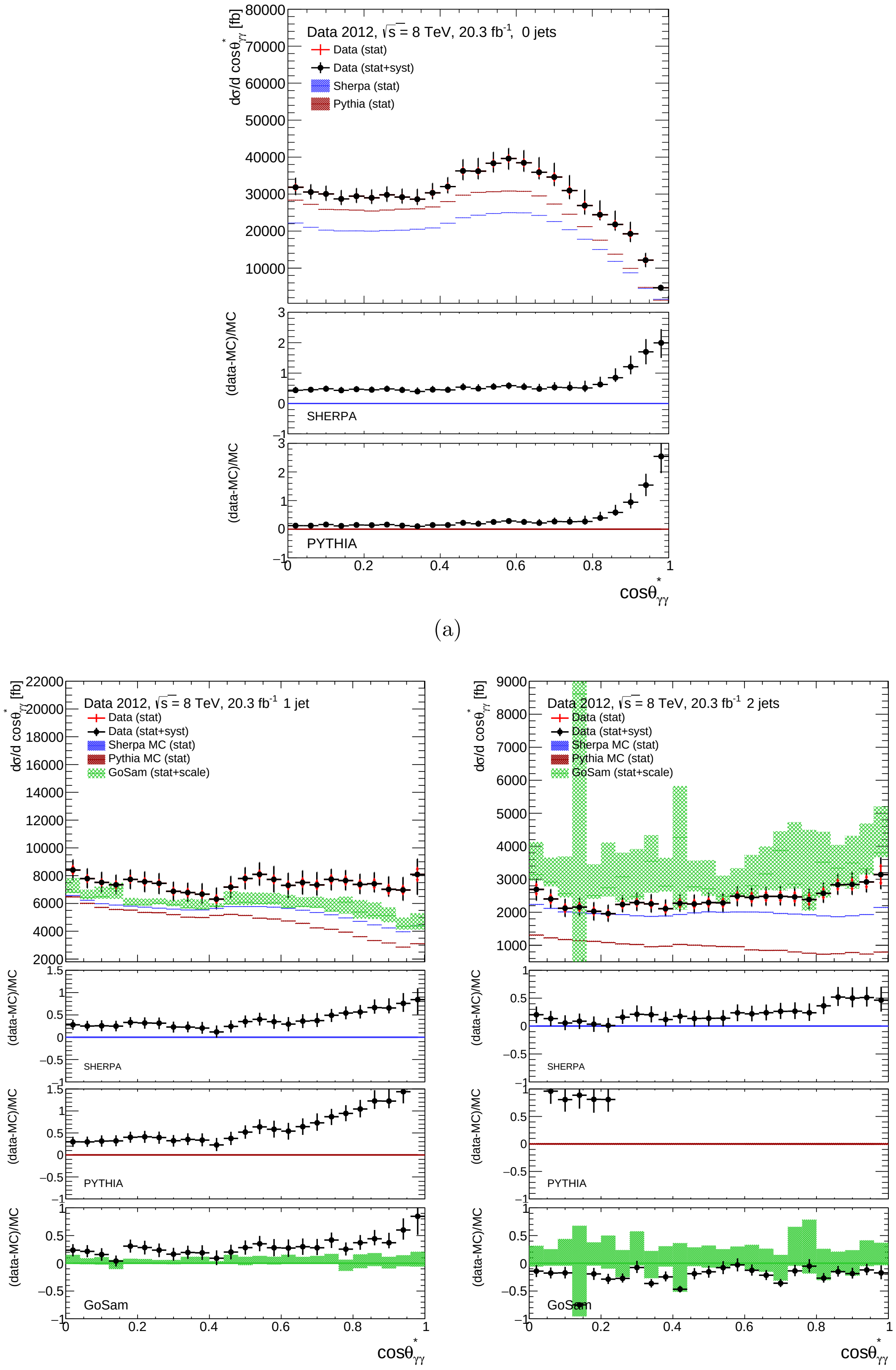

(a)

(b)

(c)

Figure A.3: *Cross sections as a function of the cosine of the polar angle in the Collins-Soper frame for the 0-jet, 1-jet and 2-jet categories.*

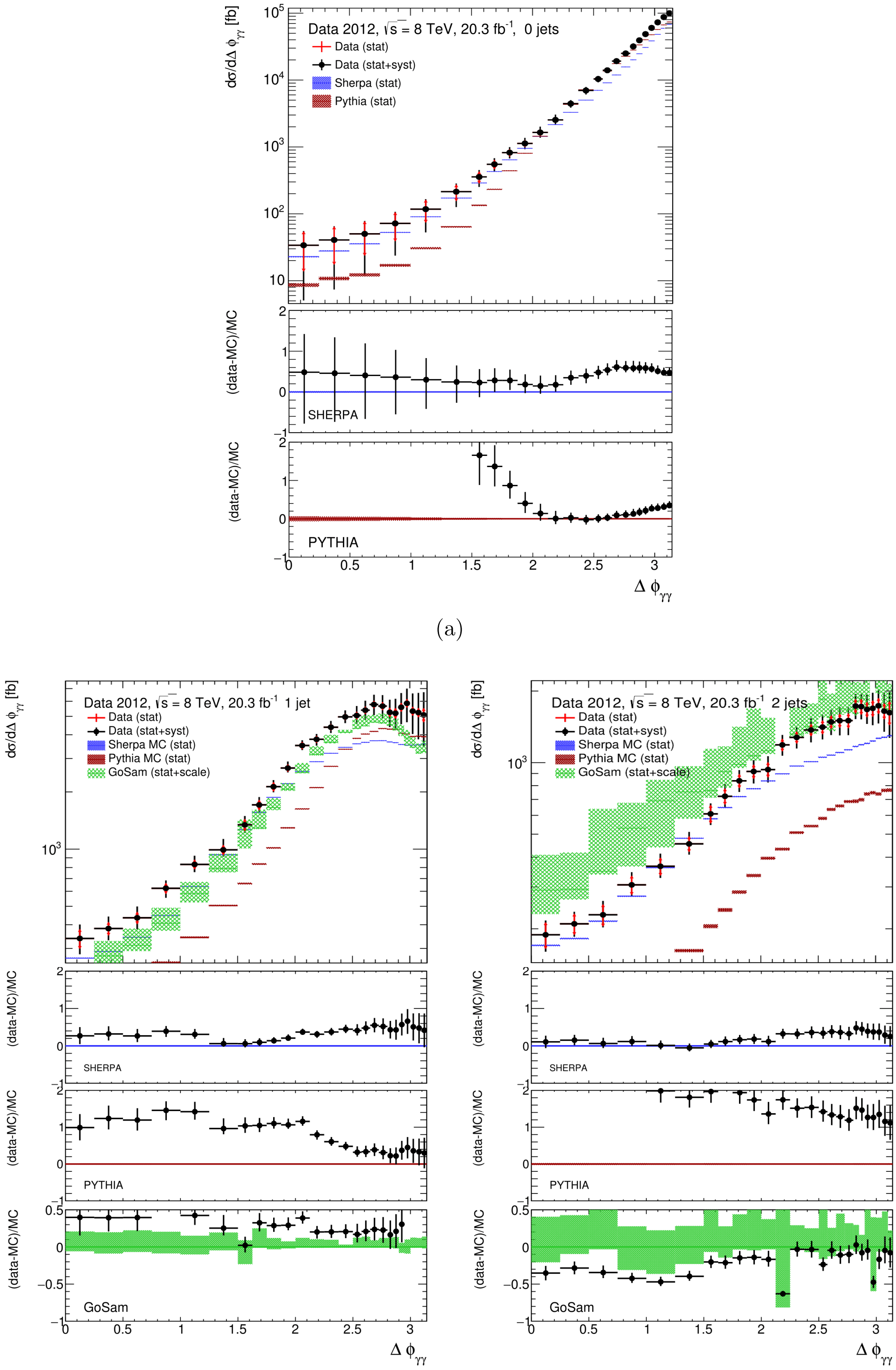

(a)

(b)

(c)

Figure A.4: *Cross sections as a function of the azimuthal angle difference between the photons for the 0-jet, 1-jet and 2-jet categories.*

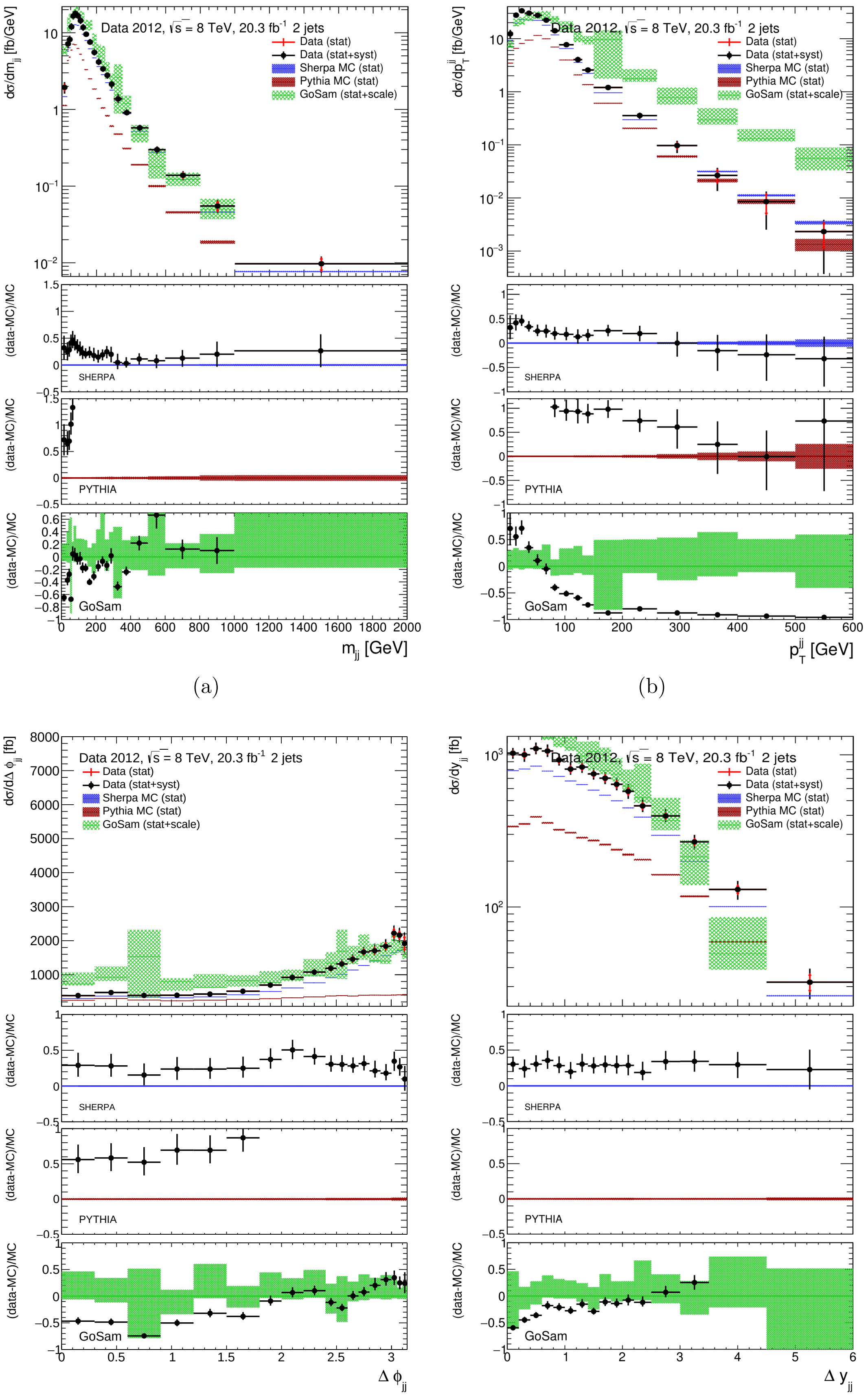

(a) (b)

(c) (d)

Figure A.5: *Cross sections as a function of the four dijet observables for the 2-jet category.*

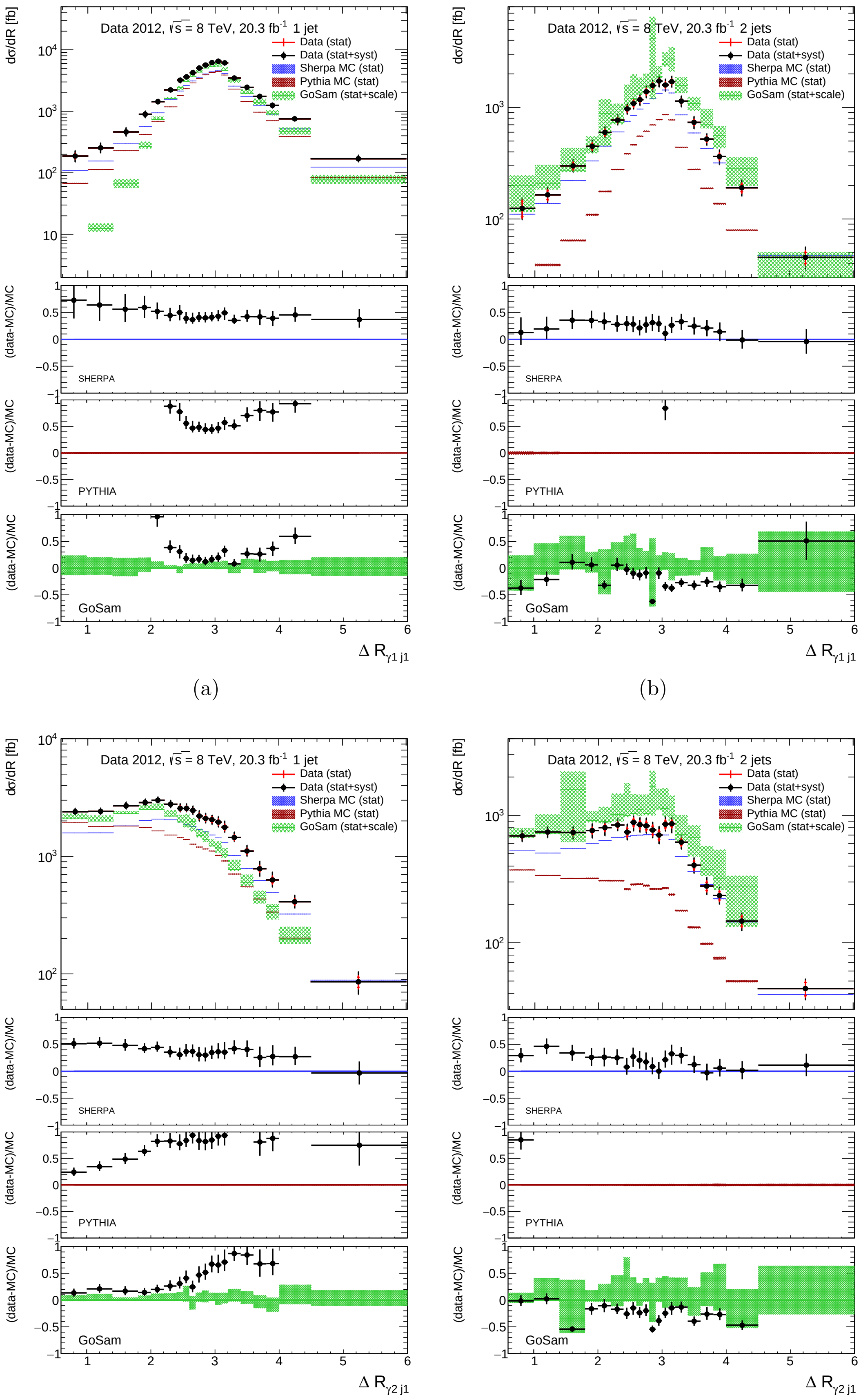

(a) (b)

(c) (d)

Figure A.6: *Cross sections as a function of the distance between leading (subleading) photon and leading jet for the 1-jet and 2-jet categories.*

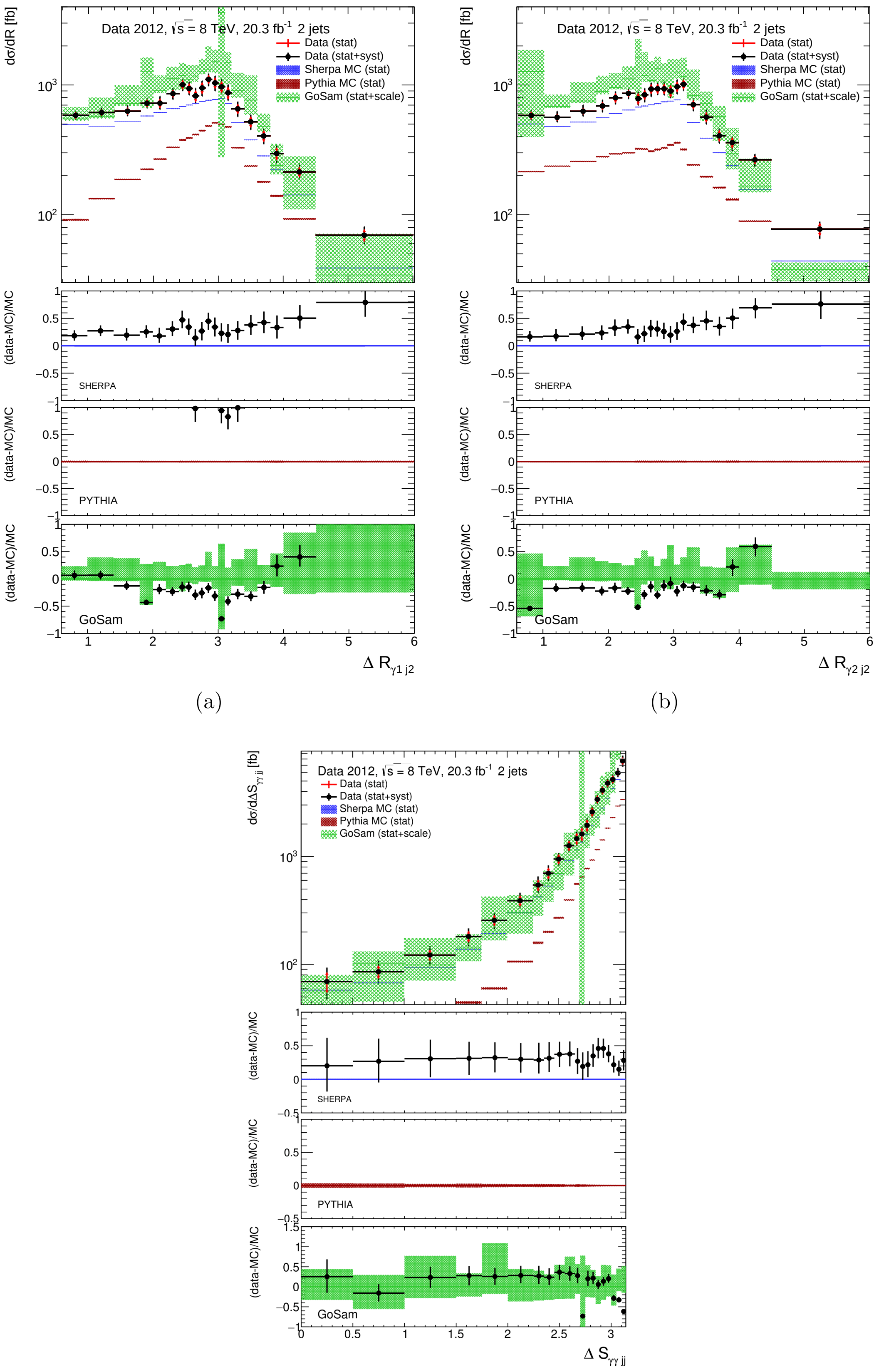

(a) (b)

(c)

Figure A.7: *Cross sections as a function of the distance between leading photon and subleading jet (a), between subleading photon and subleading jet (b), and the difference in azimuthal angle between the diphoton and the dijet system (c), all measured in the 2-jet category.*

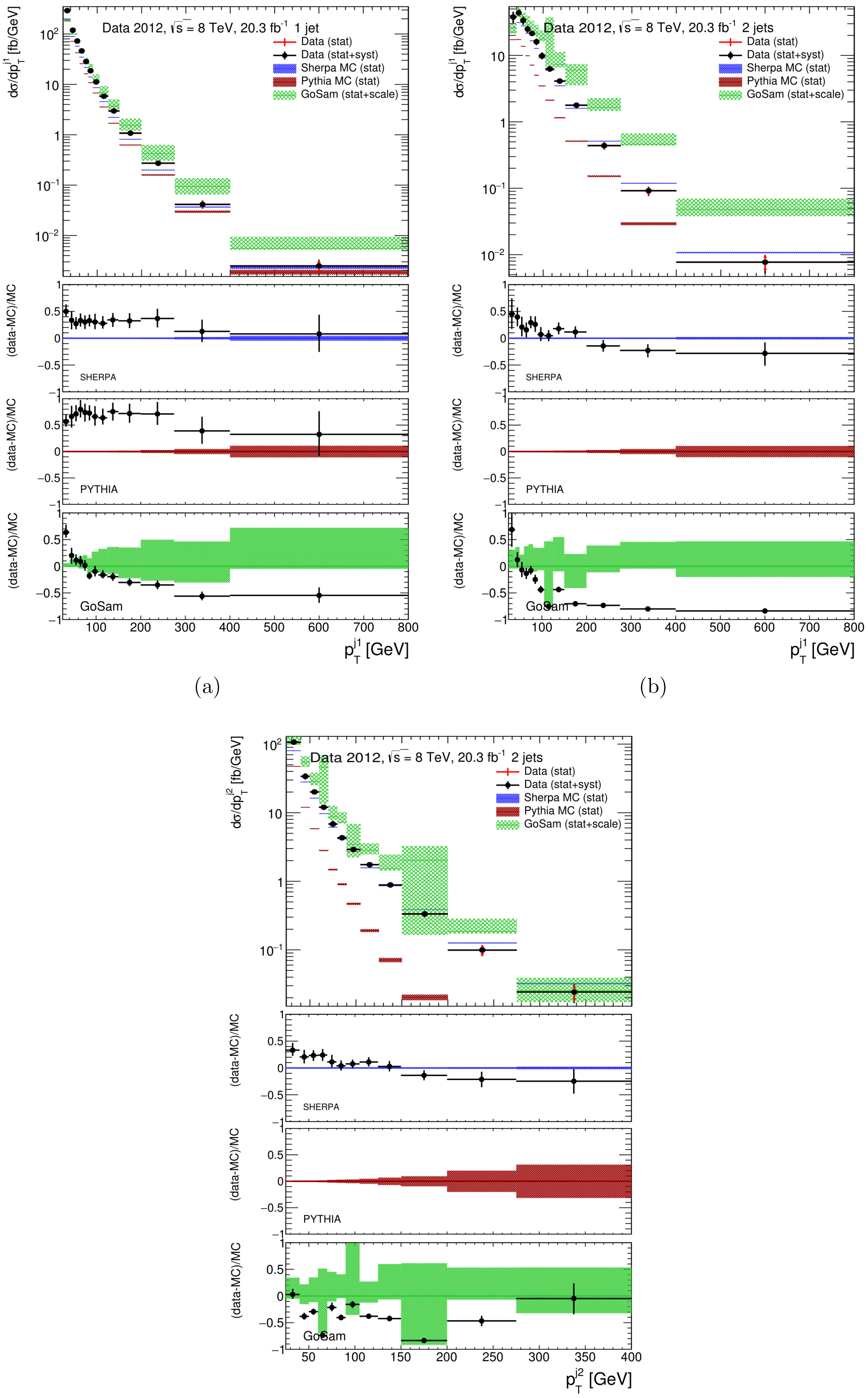

(a)

(b)

(c)

Figure A.8: *Cross sections as a function of the transverse momentum of the leading jet in the 1-jet and 2-jet categories (a,b) and the subleading jet in the 2-jet category (c).*

A.2 All measured distributions - inclusive categories

All distributions are compared to SHERPA and PYTHIA predictions. GOSAM predictions are not available for inclusive categories.

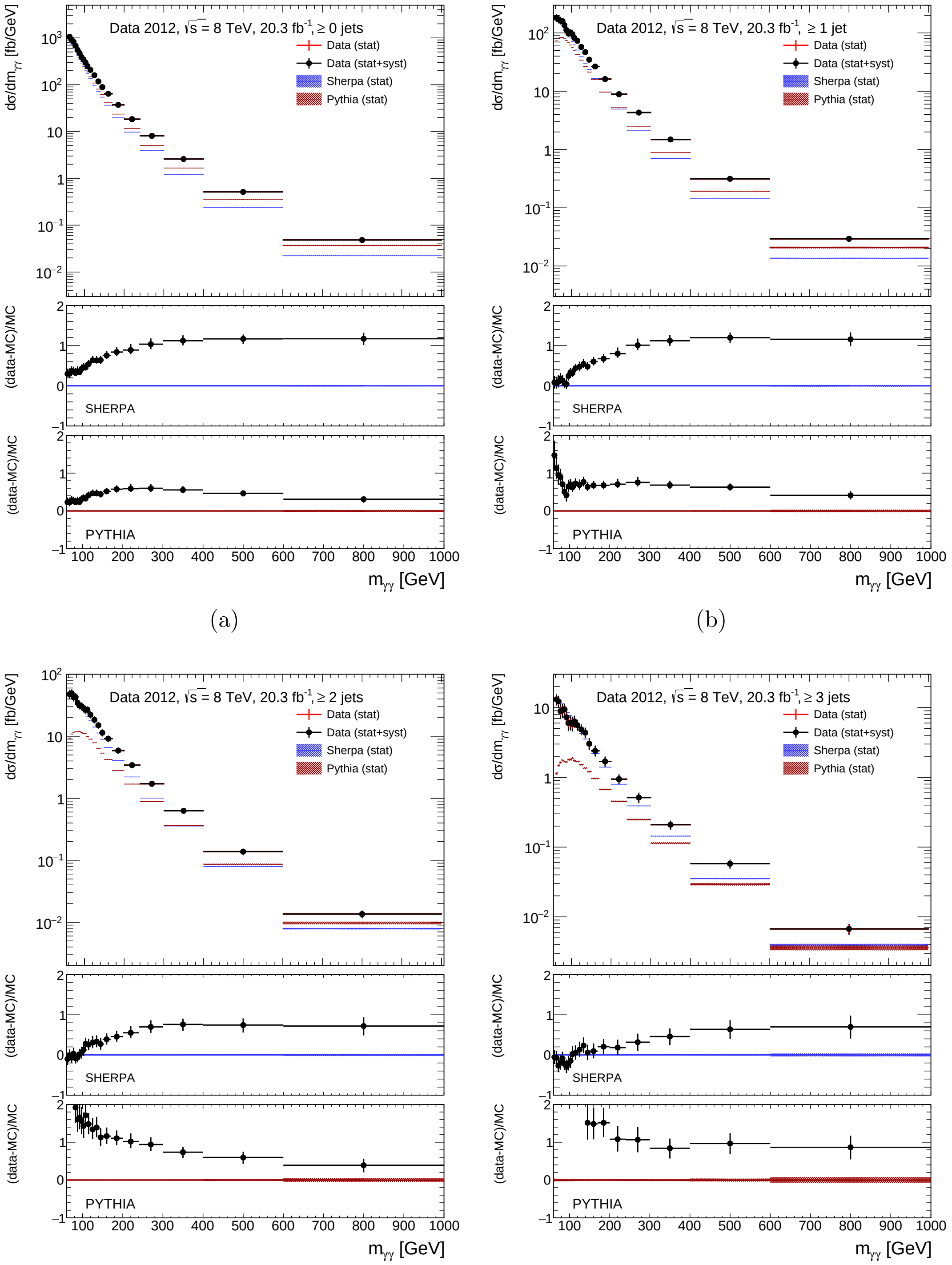

(a) (b)

(c) (d)

Figure A.9: *Cross sections as a function of the diphoton invariant mass for all inclusive jet categories.*

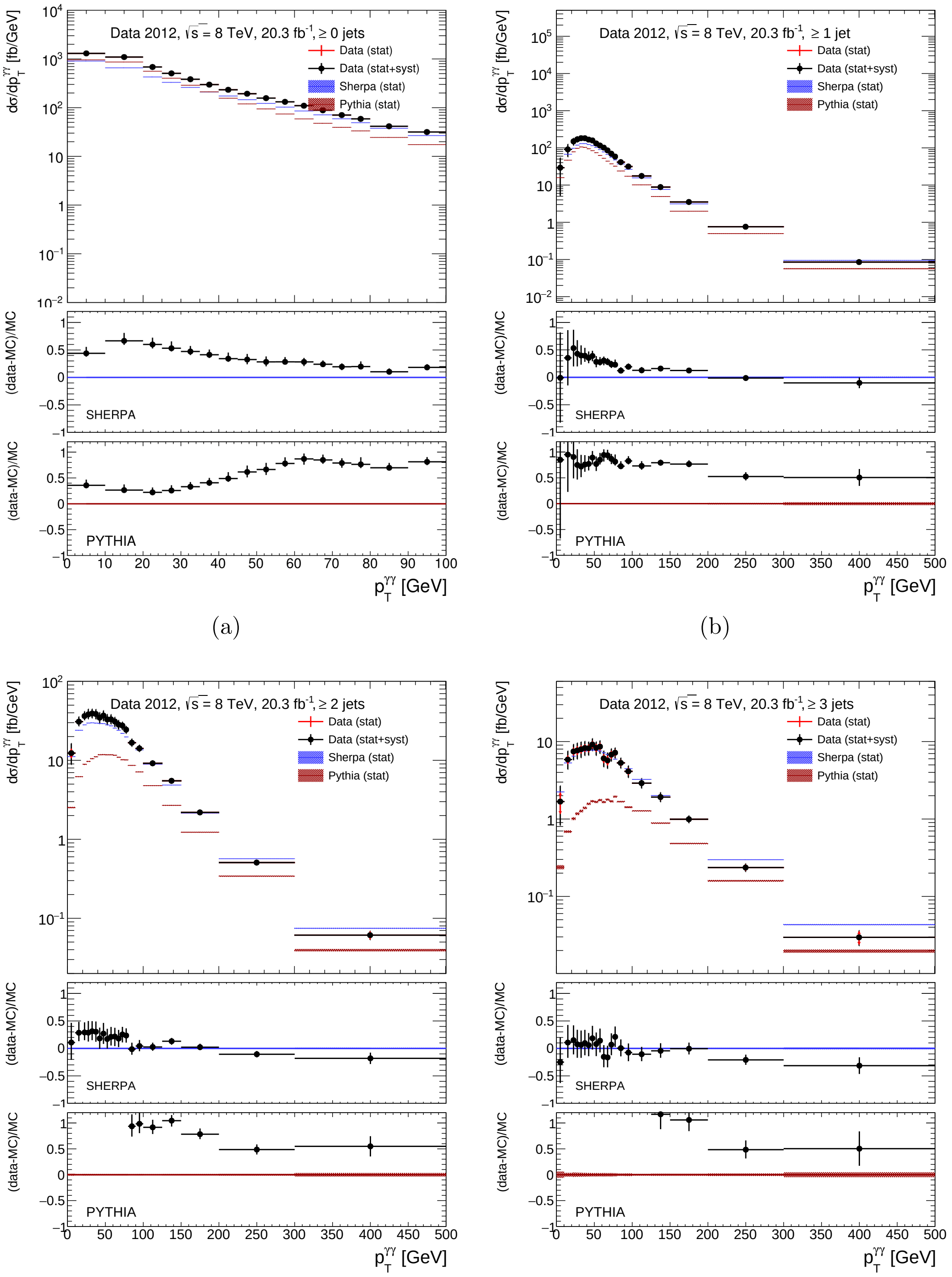

(a)

(b)

(c)

(d)

Figure A.10: *Cross sections as a function of the diphoton transverse momentum for all inclusive jet categories.*

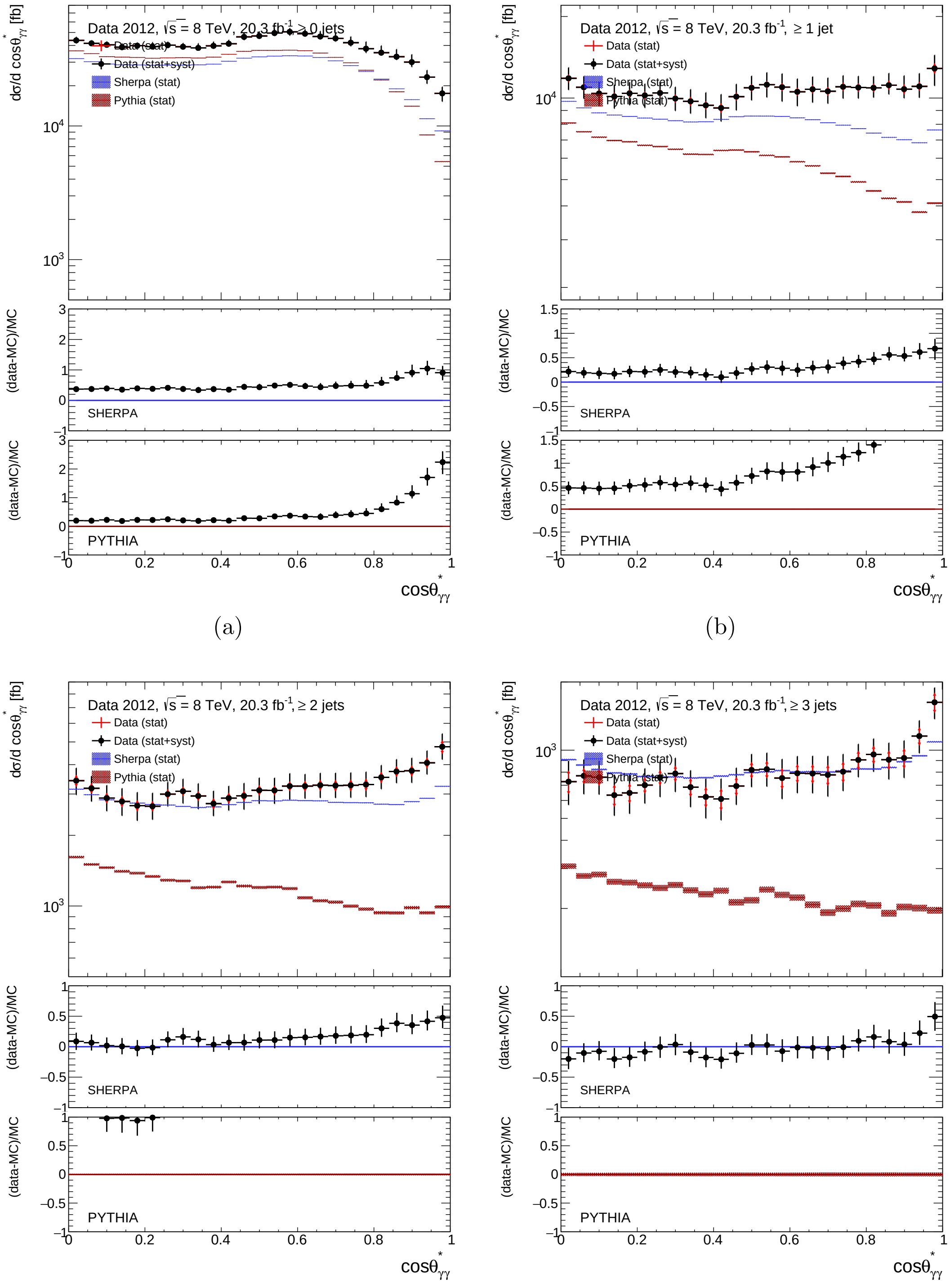

(a) (b)

(c) (d)

Figure A.11: *Cross sections as a function of the cosine of the polar angle in the Collins-Soper frame for all inclusive jet categories.*

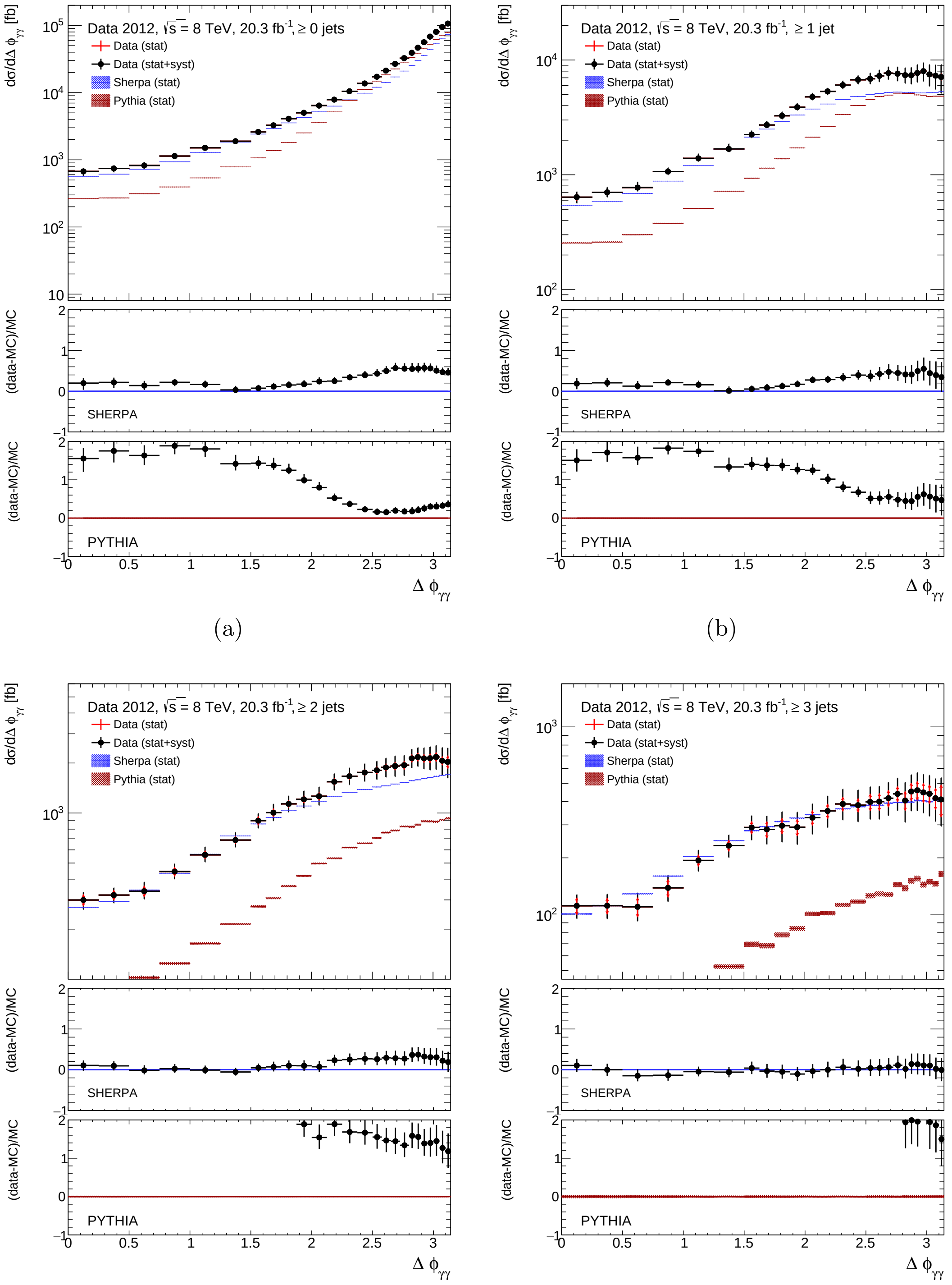

(a) (b)

(c) (d)

Figure A.12: *Cross sections as a function of the azimuthal angle difference between the photons for all inclusive jet categories.*

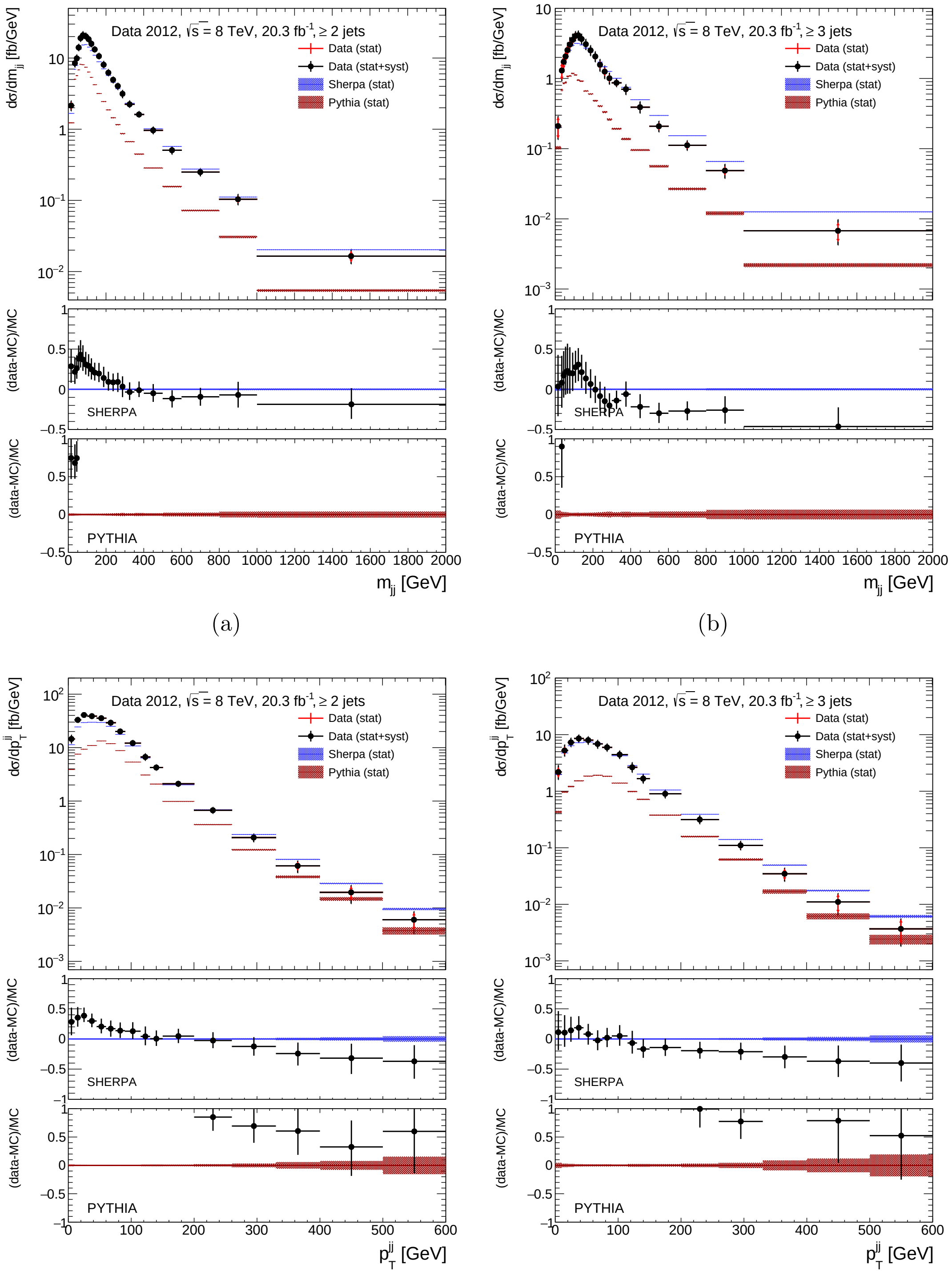

(a)

(b)

(c)

(d)

Figure A.13: *Cross sections as a function of the dijet mass and transverse momentum for all inclusive jet categories.*

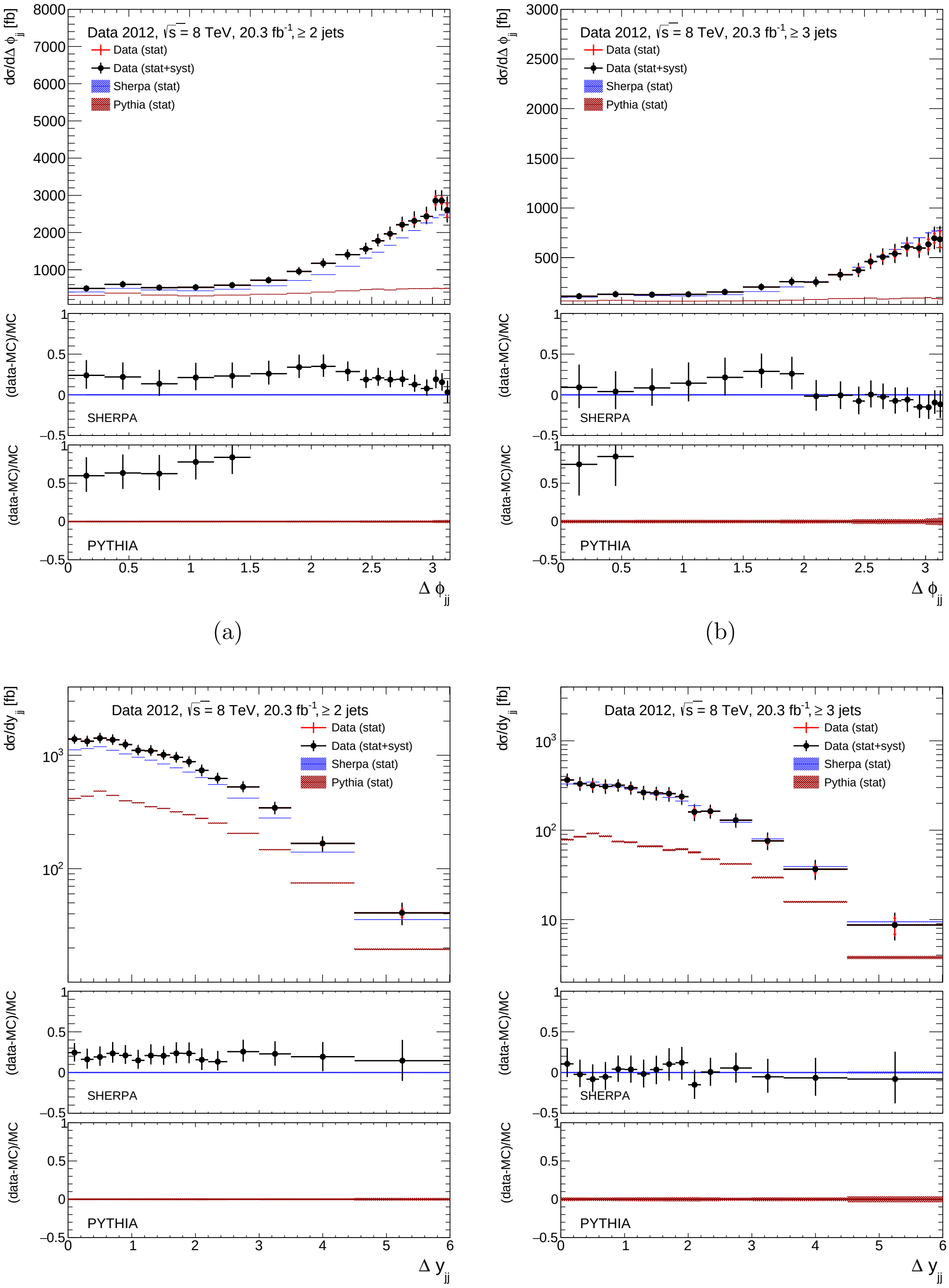

(a) (b) (c) (d)

Figure A.14: *Cross sections as a function of the polar angle and rapidity differences for all inclusive jet categories.*

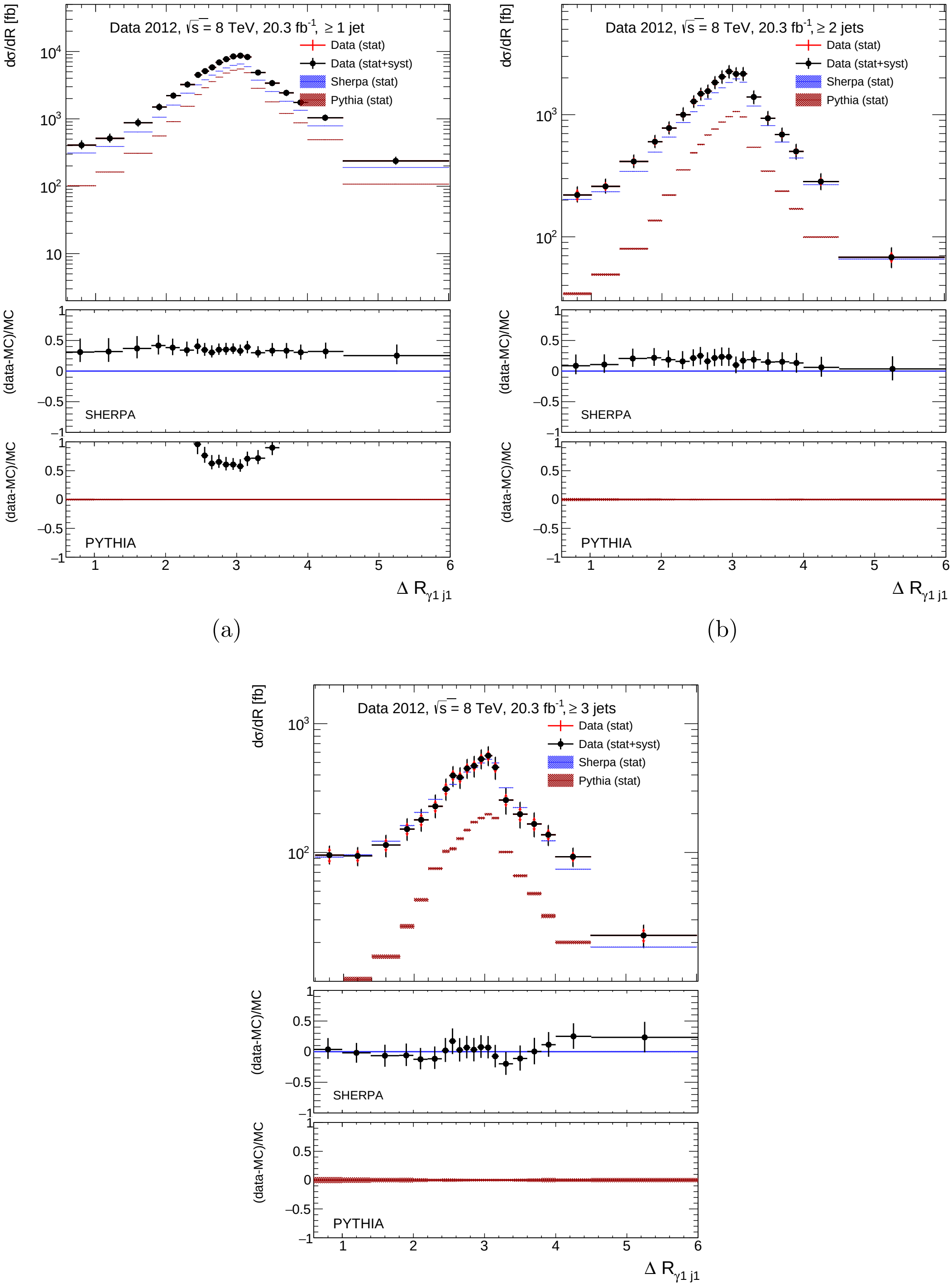

(a)

(b)

(c)

Figure A.15: *Cross sections as a function of the distance between leading photon and leading jet for all inclusive jet categories.*

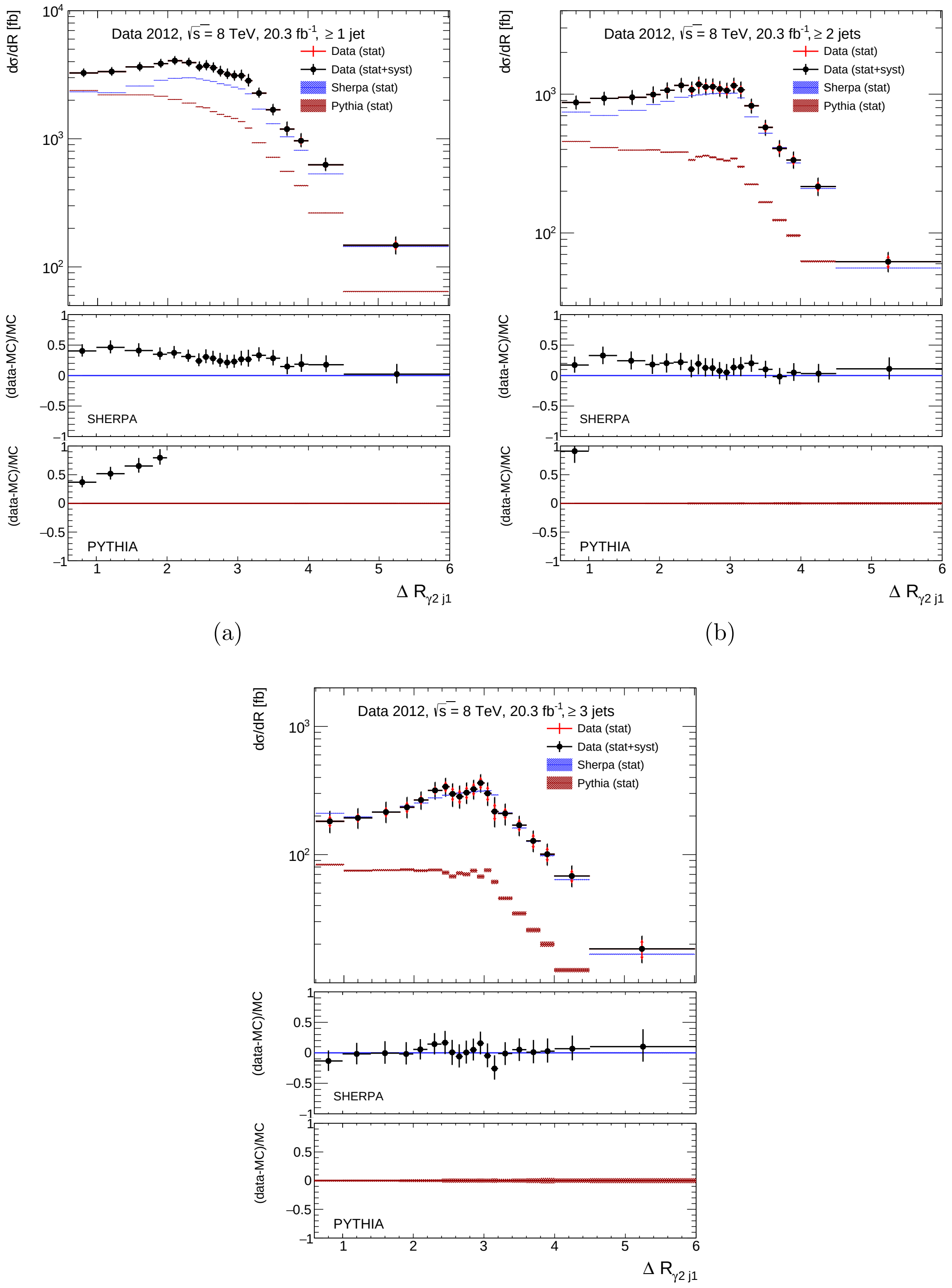

(a) (b) (c)

Figure A.16: *Cross sections as a function of the distance between subleading photon and leading jet for all inclusive jet categories.*

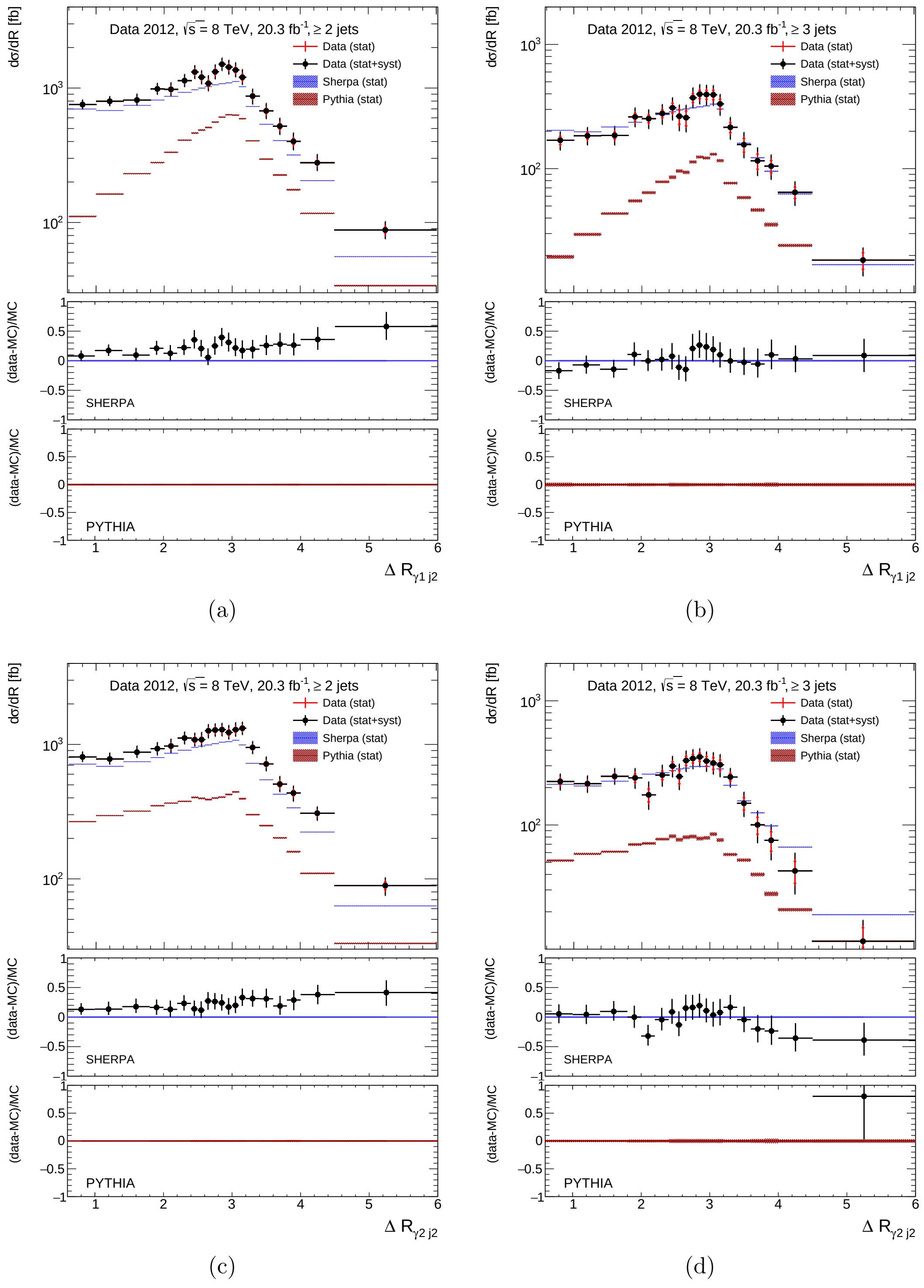

(a) (b)

(c) (d)

Figure A.17: *Cross sections as a function of the distance between leading photon and subleading jet (a,b) and between subleading photon and subleading jet (c,d) for all inclusive jet categories.*

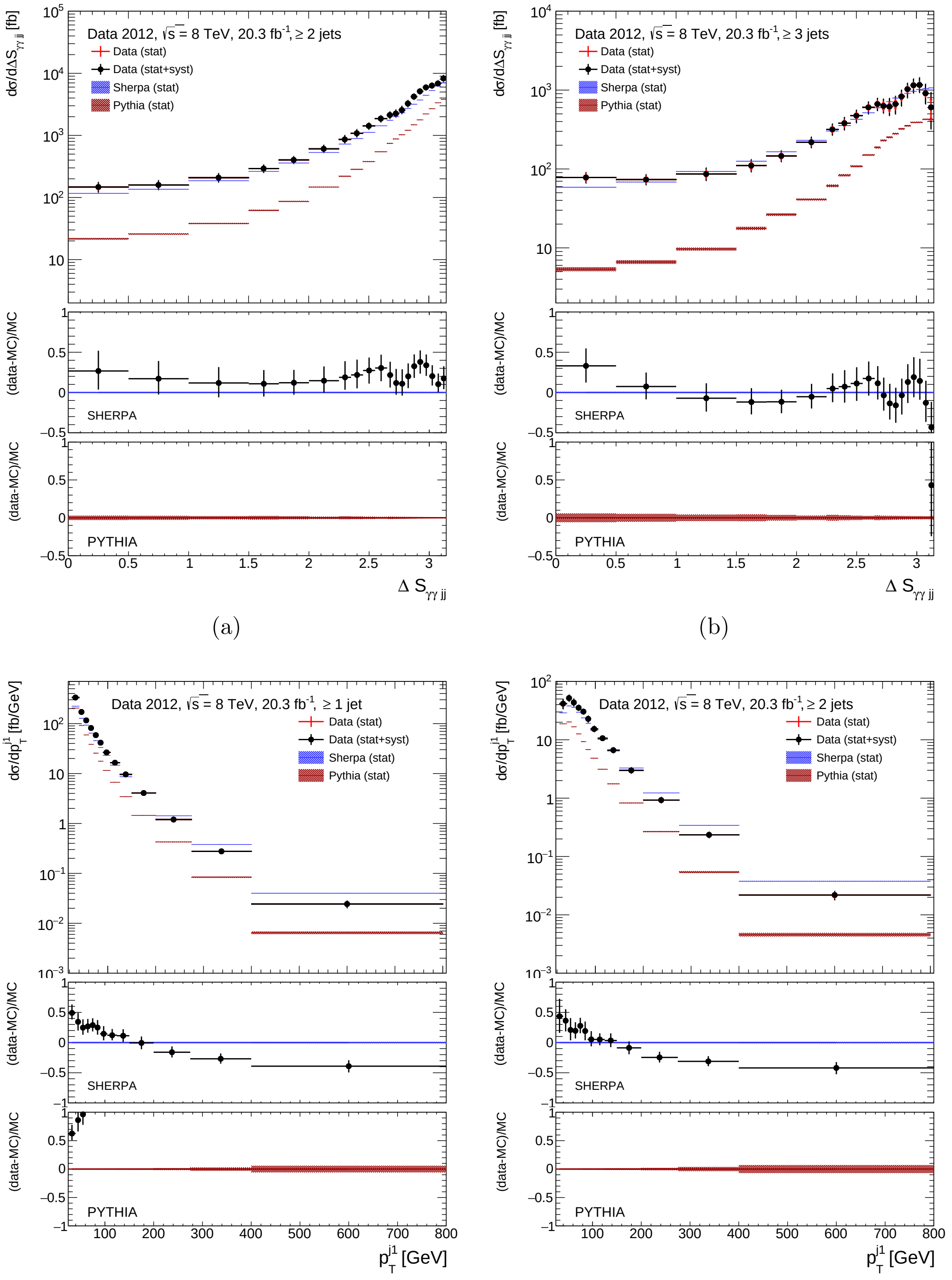

(a) (b)

(c) (d)

Figure A.18: *Cross sections as a function of the difference in azimuthal angle between the diphoton and the dijet system in the ≥ 2-jet and ≥ 3-jet categories (a,b) and the transverse momentum of the leading photon in the ≥ 1-jet and ≥ 2-jet categories (c,d).*

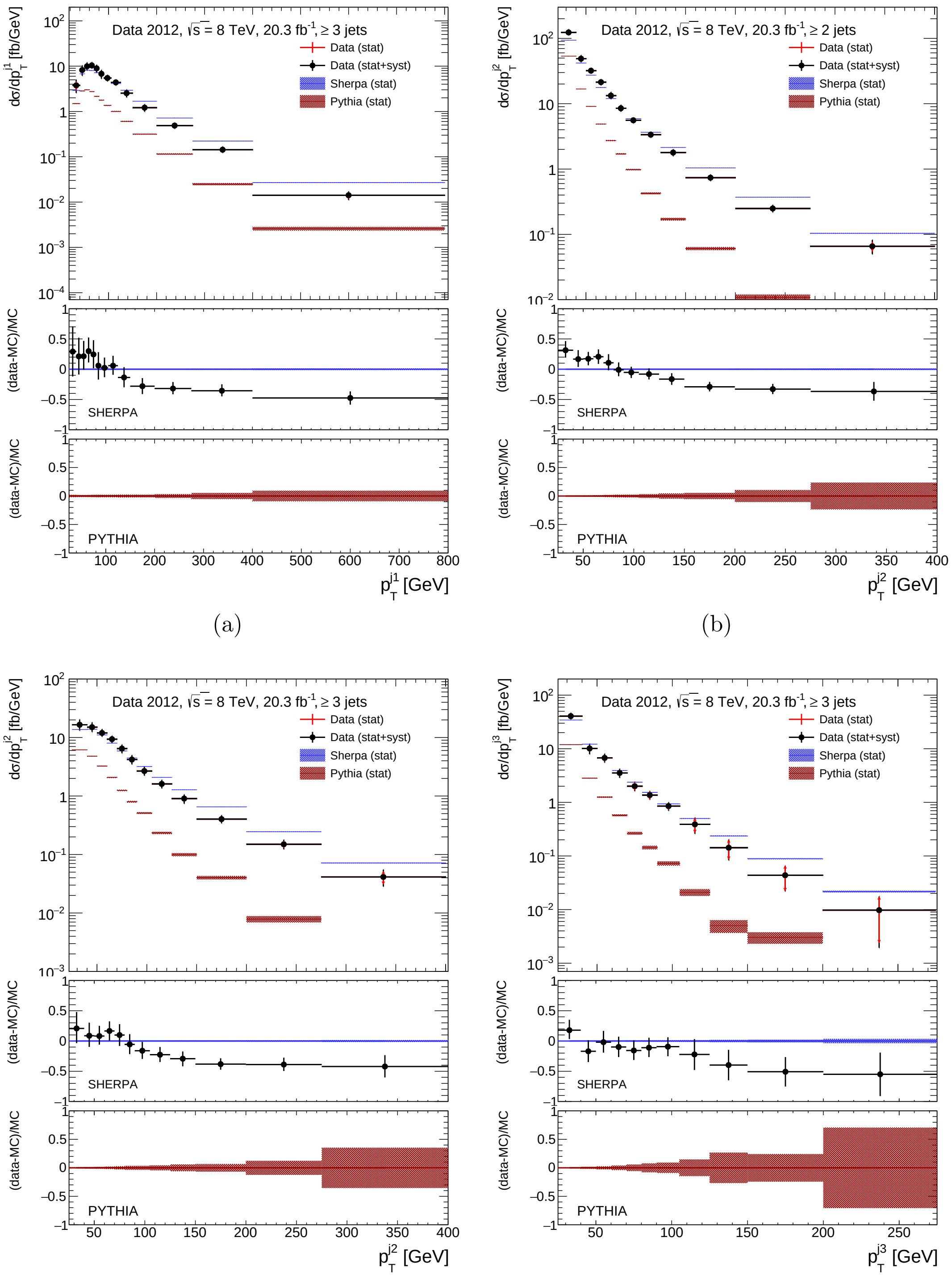

(a) (b)

(c) (d)

Figure A.19: *Cross sections as a function of the transverse momentum of the leading jet in the $\geq$ 3-jet category (a), the transverse momentum of the subleading jet in the $\geq$ 2-jet (b) and $\geq$ 3-jet categories (c) and the transverse momentum of the third jet in the $\geq$ 3-jet category (d).*

A.3 Breakdown of systematic uncertainties in all observables - exclusive categories

The following plots show the individual relative systematic uncertainties in all measured exclusive jet categories, together with the statistical uncertainty as comparison. The color scheme is the same for all plots, to improve the visibility the legend is not included everywhere.

- Dashed: statistical uncertainty
- Total systematic uncertainty
- Photon energy scale
- Photon energy resolution
- Jet energy scale
- Jet energy resolution
- Jet vertex fraction
- Scale factors
- Jet background subtraction
- Electron background subtraction
- Unfolding bias
- MC statistics in unfolding

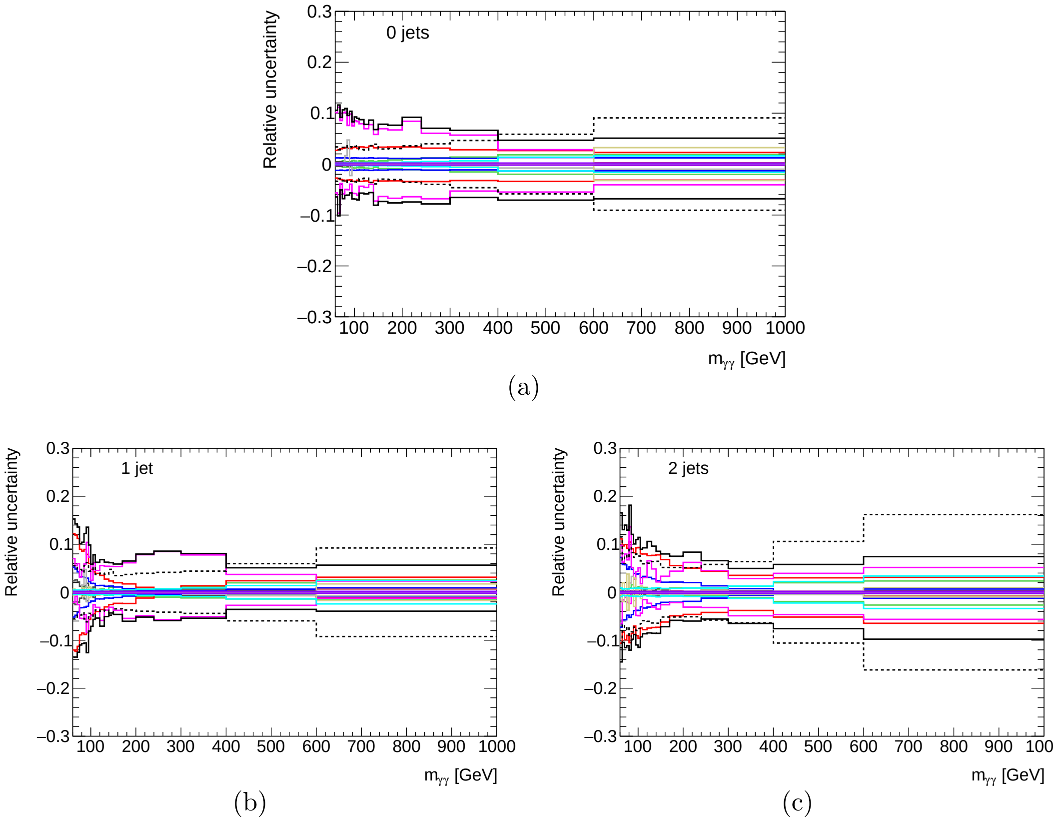

(a)

(b)

(c)

Figure A.20: *Relative systematic uncertainties as a function of the diphoton invariant mass for the 0-jet, 1-jet and 2-jet categories.*

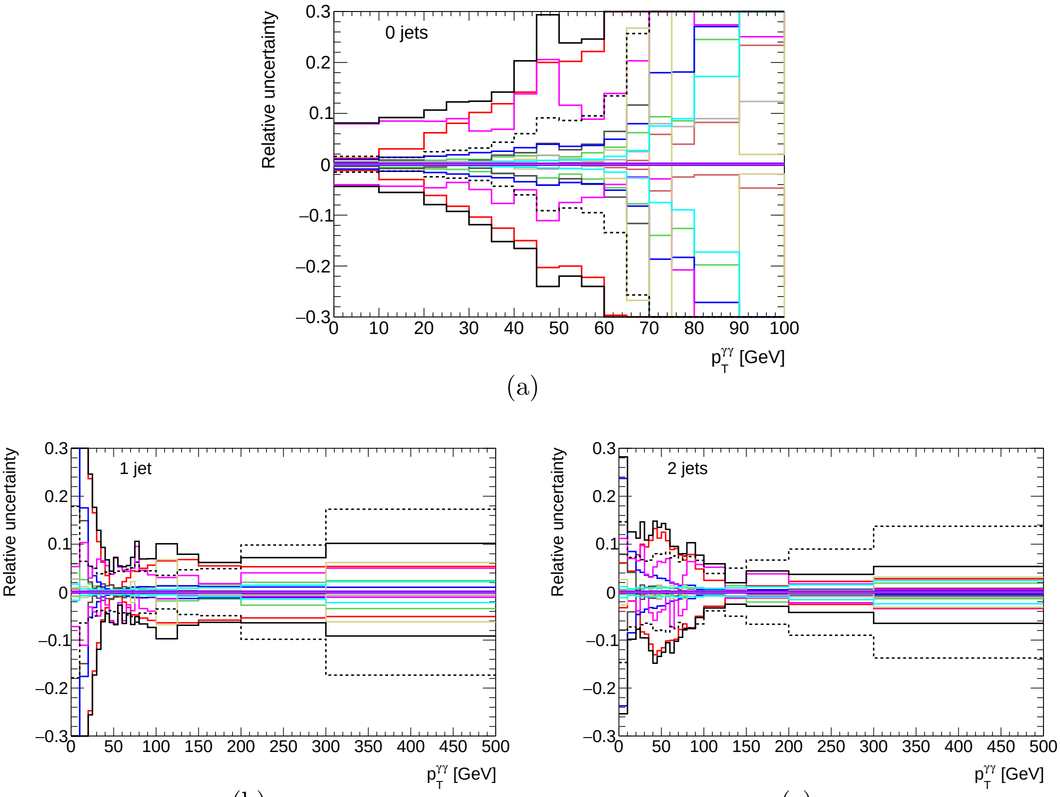

(a)

(b)

(c)

Figure A.21: *Relative systematic uncertainties as a function of the diphoton transverse momentum for the 0-jet, 1-jet and 2-jet categories.*

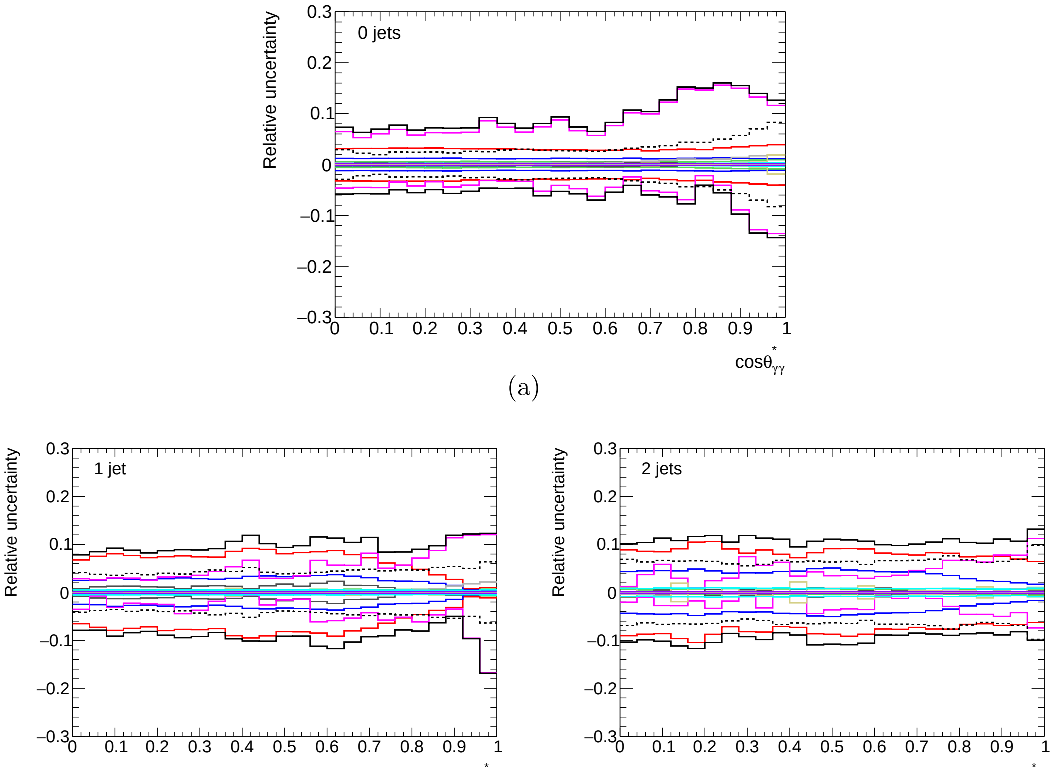

(a)

(b)

(c)

Figure A.22: *Relative systematic uncertainties as a function of the cosine of the polar angle in the Collins-Soper frame for the 0-jet, 1-jet and 2-jet categories.*

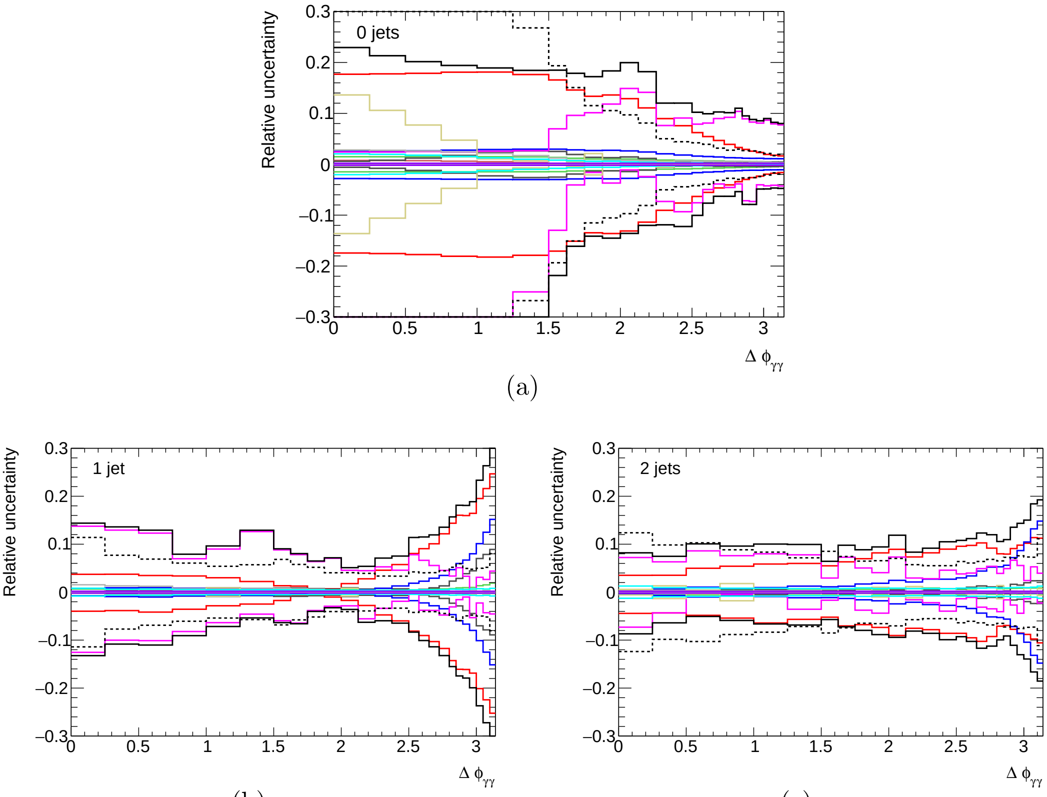

(a)

(b)

(c)

Figure A.23: *Relative systematic uncertainties as a function of the azimuthal angle difference between the photons for the 0-jet, 1-jet and 2-jet categories.*

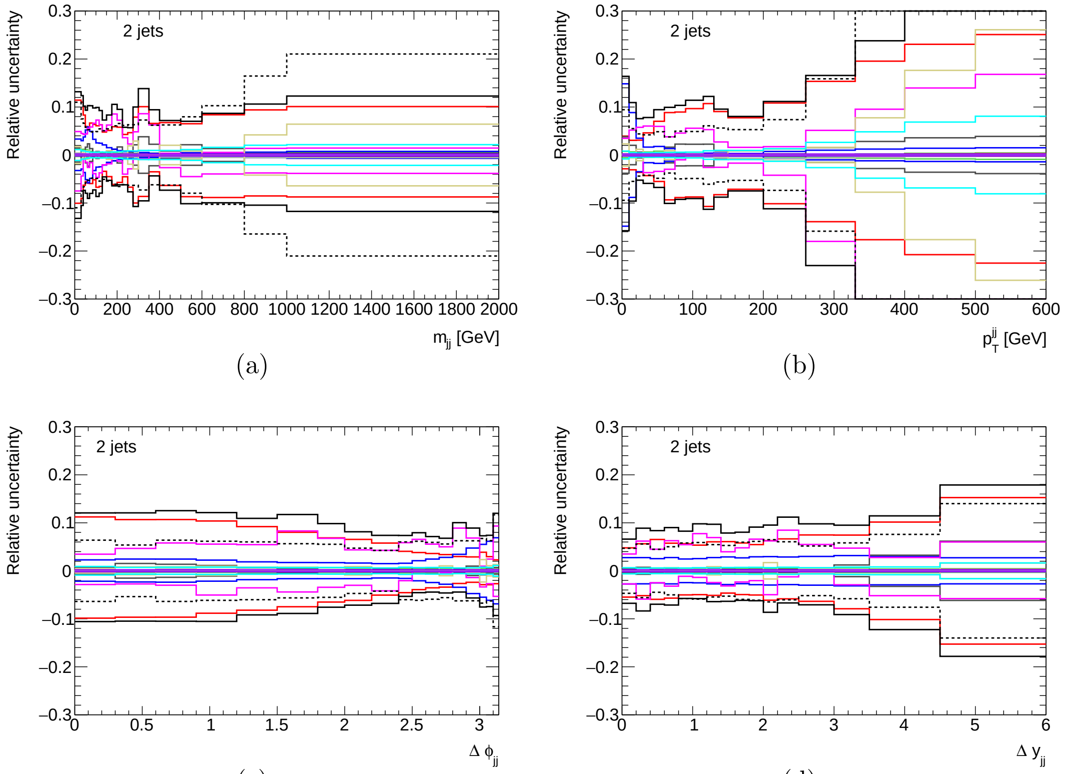

(a) (b)

(c) (d)

Figure A.24: *Relative systematic uncertainties as a function of the four dijet observables for the 2-jet category.*

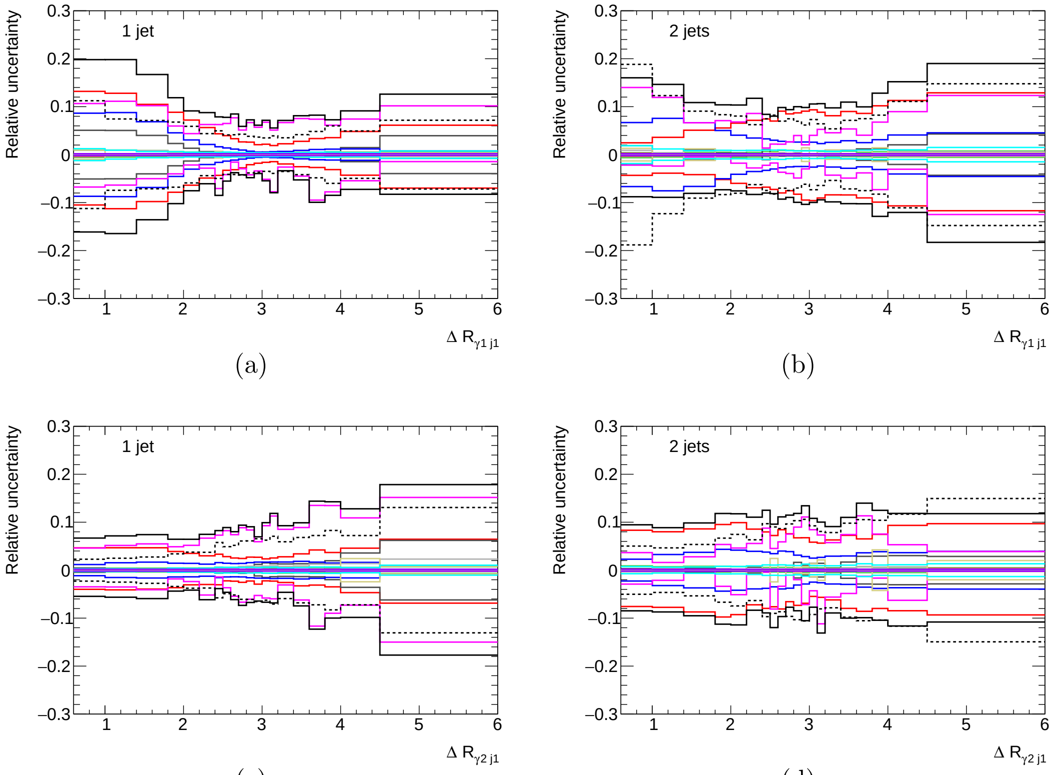

(a) (b)

(c) (d)

Figure A.25: *Relative systematic uncertainties as a function of the distance between leading (subleading) photon and leading jet for the 1-jet and 2-jet categories.*

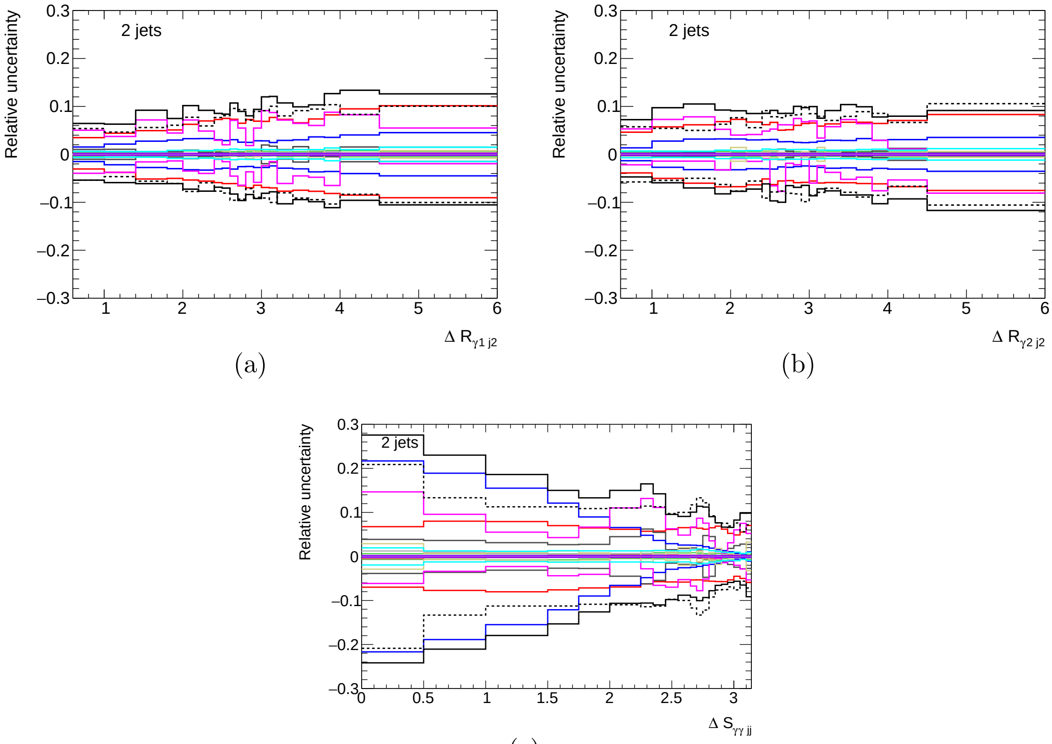

(a)

(b)

(c)

Figure A.26: *Relative systematic uncertainties as a function of the distance between leading photon and subleading jet (a), between subleading photon and subleading jet (b), and the difference in azimuthal angle between the diphoton and the dijet system (c), all measured in the 2-jet category.*

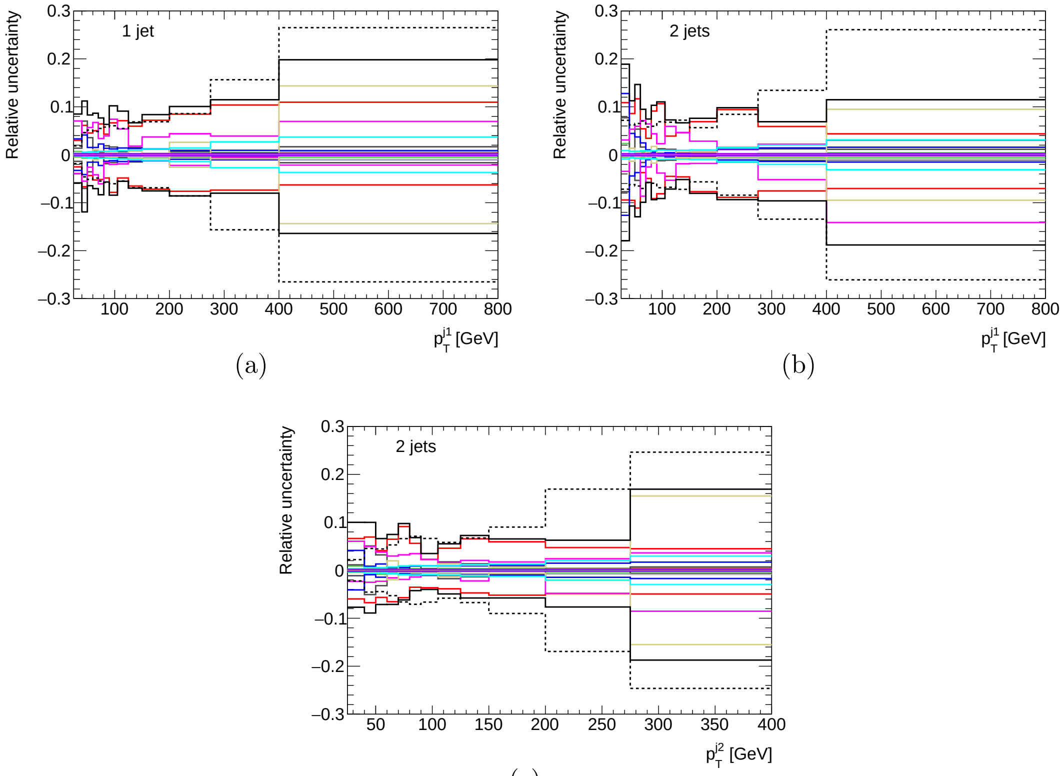

(a) (b)

(c)

Figure A.27: *Relative systematic uncertainties as a function of the transverse momentum of the leading jet in the 1-jet and 2-jet categories (a,b) and the subleading jet in the 2-jet category (c).*

A.4 Breakdown of systematic uncertainties in all observables - inclusive categories

The following plots show the individual relative systematic uncertainties in all measured inclusive jet categories, together with the statistical uncertainty as comparison. The color scheme is the same for all plots, to improve the visibility the legend is not included everywhere.

As notable difference to the exclusive spectra, the jet-related uncertainties are generally smaller, especially in the ≥ 0-jet category.

- Dashed: statistical uncertainty
- Total systematic uncertainty
- Photon energy scale
- Photon energy resolution
- Jet energy scale
- Jet energy resolution
- Jet vertex fraction
- Scale factors
- Jet background subtraction
- Electron background subtraction
- Unfolding bias
- MC statistics in unfolding

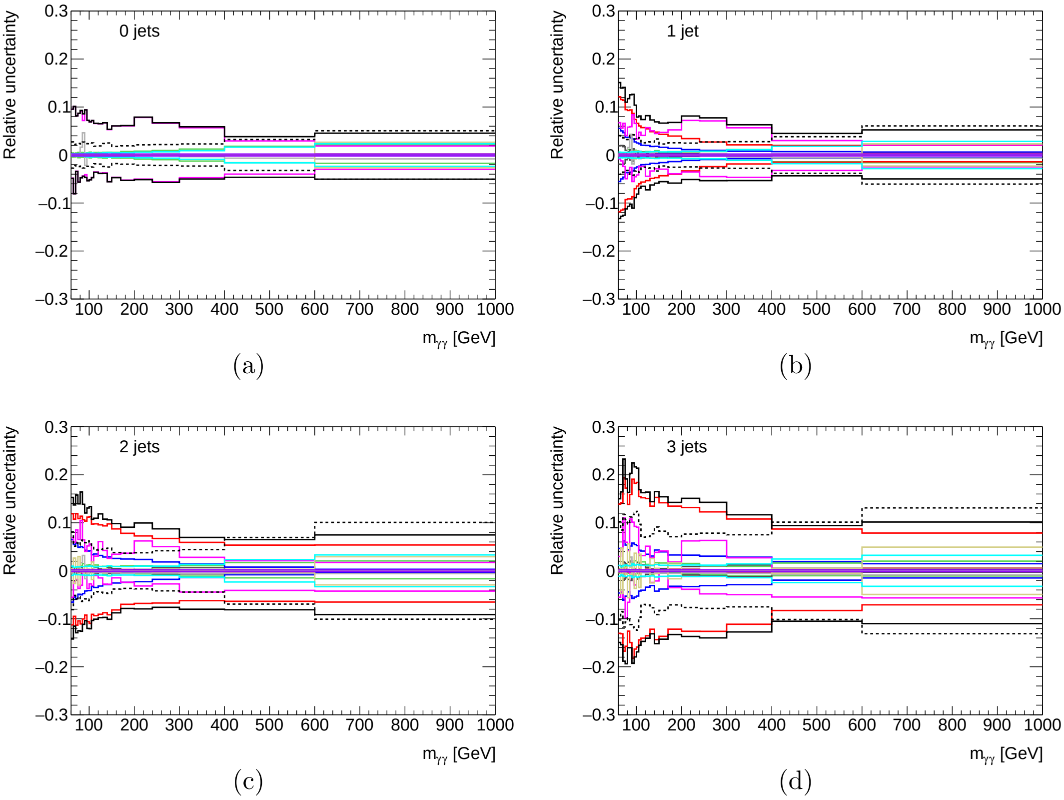

(a) (b) (c) (d)

Figure A.28: *Relative systematic uncertainties as a function of the diphoton invariant mass for all inclusive jet categories.*

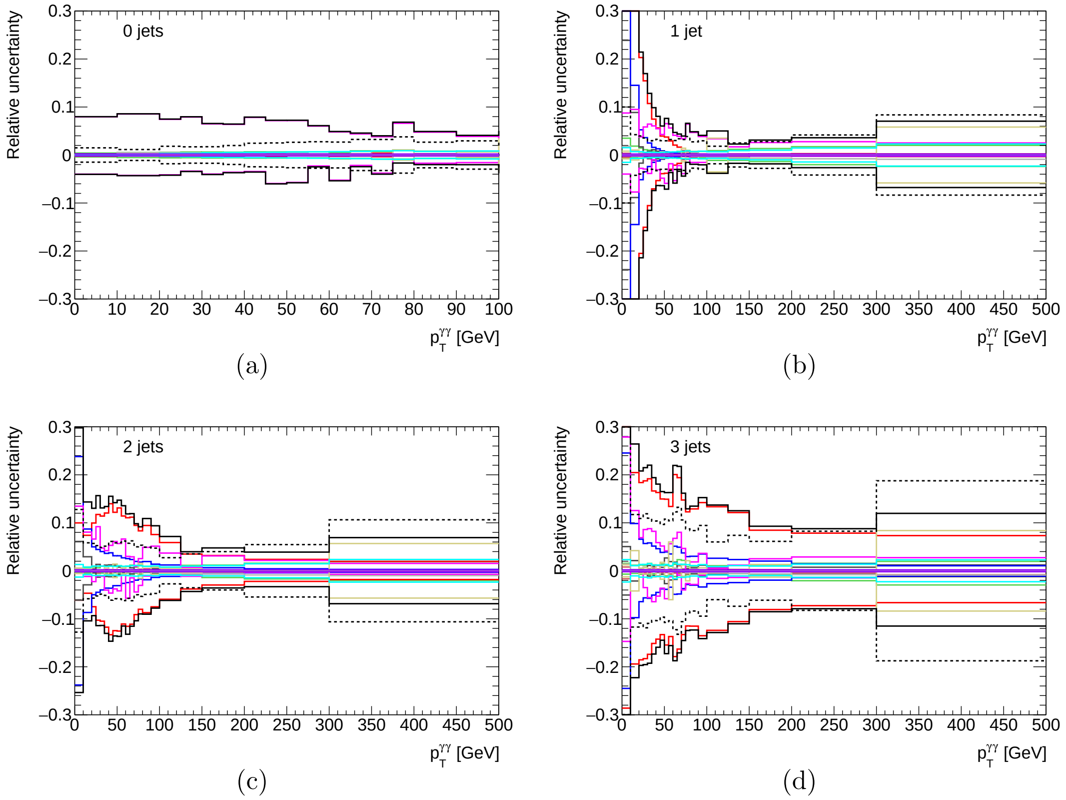

(a) (b)

(c) (d)

Figure A.29: *Relative systematic uncertainties as a function of the diphoton transverse momentum for all inclusive jet categories.*

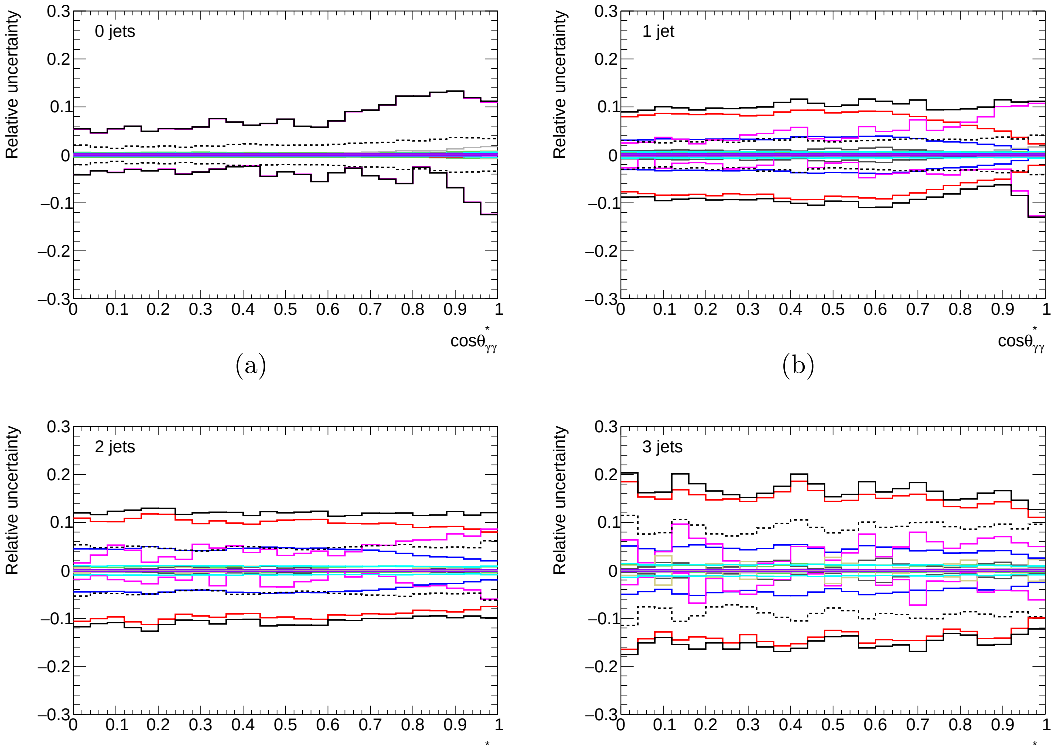

(a) (b)

(c) (d)

Figure A.30: *Relative systematic uncertainties as a function of the cosine of the polar angle in the Collins-Soper frame for all inclusive jet categories.*

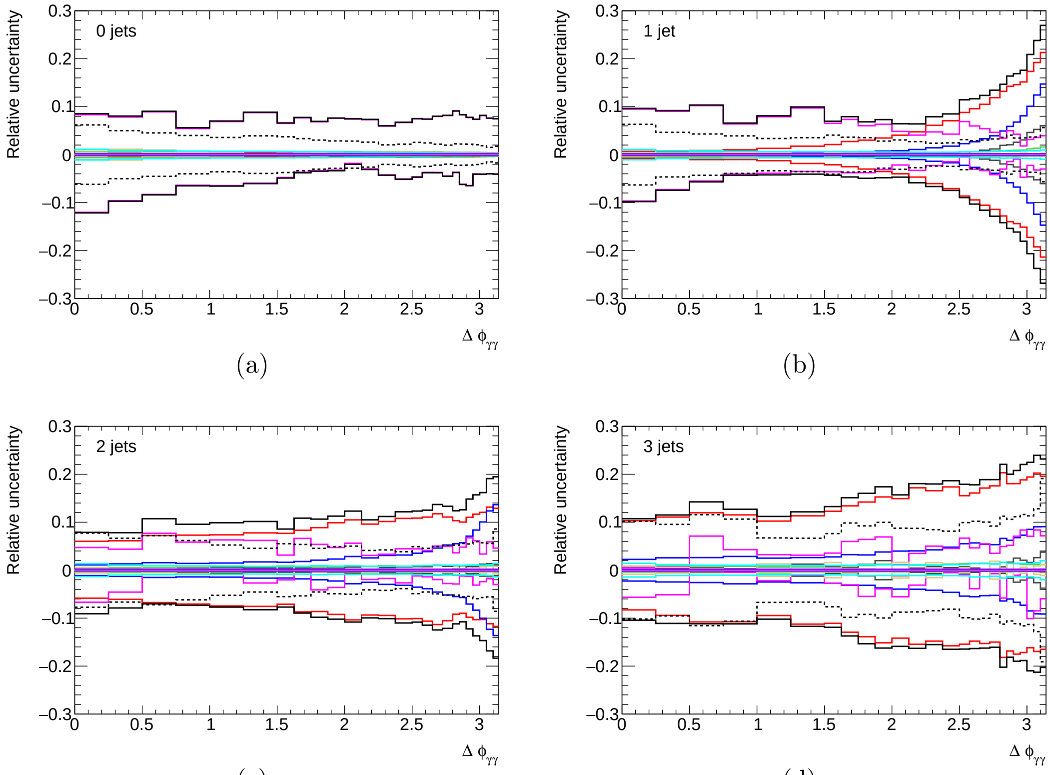

(a) (b)

(c) (d)

Figure A.31: *Relative systematic uncertainties as a function of the azimuthal angle difference between the photons for all inclusive jet categories.*

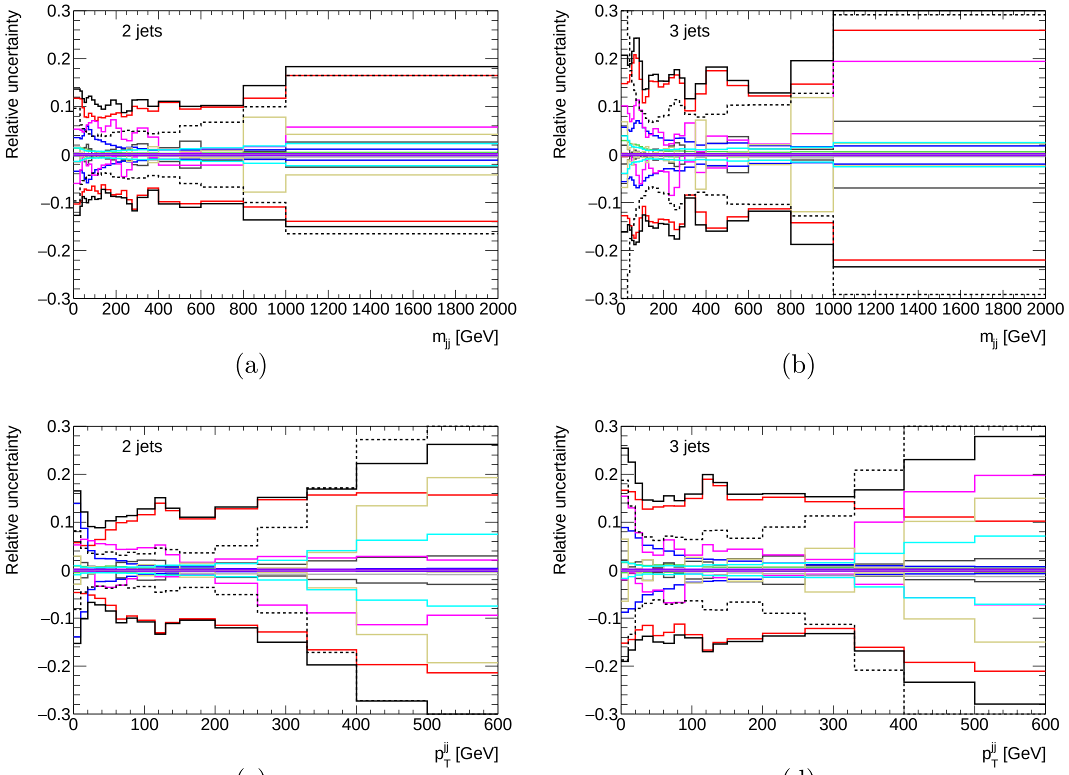

(a) (b)

(c) (d)

Figure A.32: *Relative systematic uncertainties as a function of the dijet mass and transverse momentum for all inclusive jet categories.*

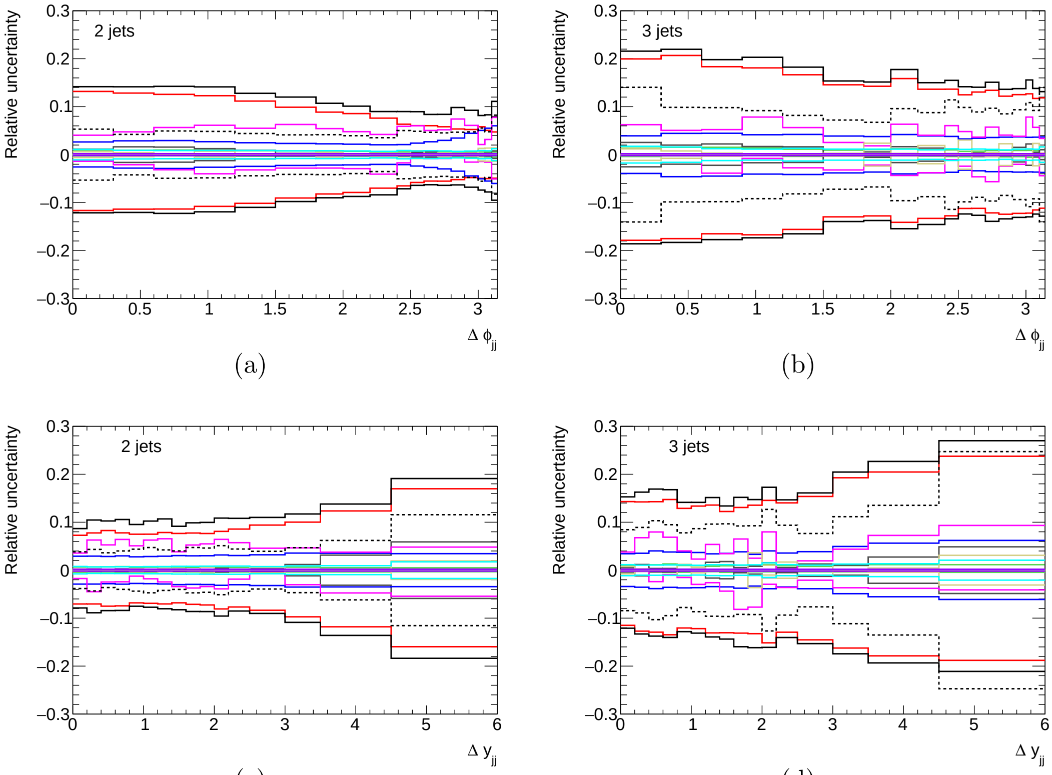

(a) (b)

(c) (d)

Figure A.33: *Relative systematic uncertainties as a function of the polar angle and rapidity differences for all inclusive jet categories.*

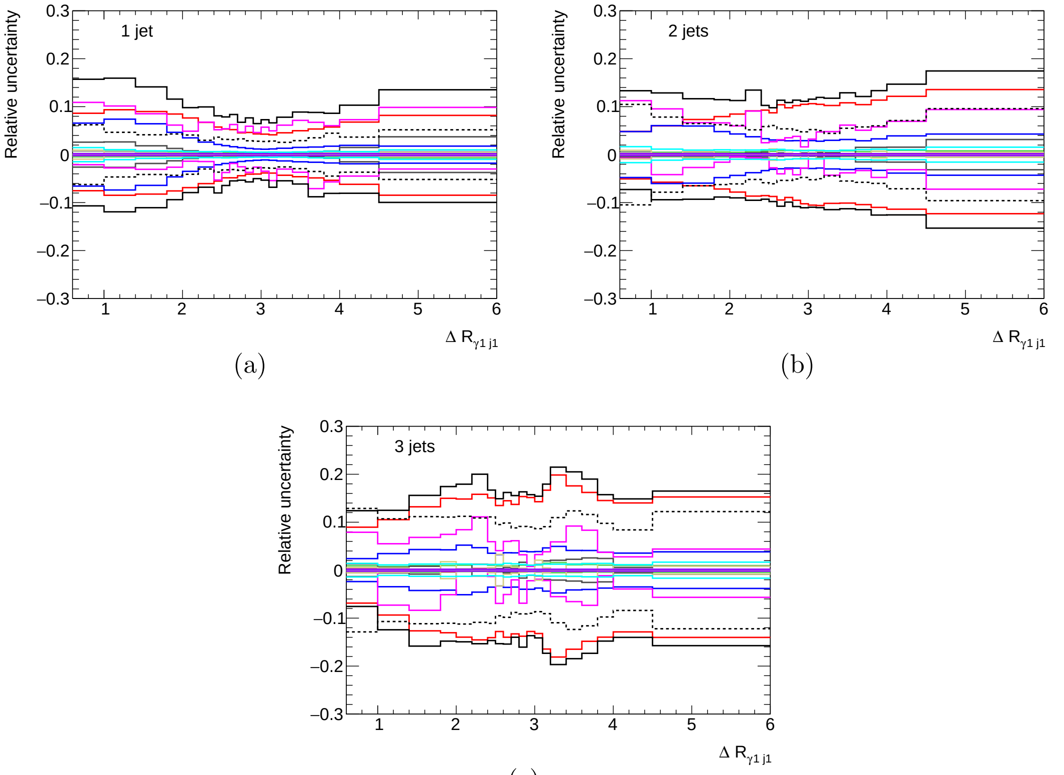

(a) (b)

(c)

Figure A.34: *Relative systematic uncertainties as a function of the distance between leading photon and leading jet for all inclusive jet categories.*

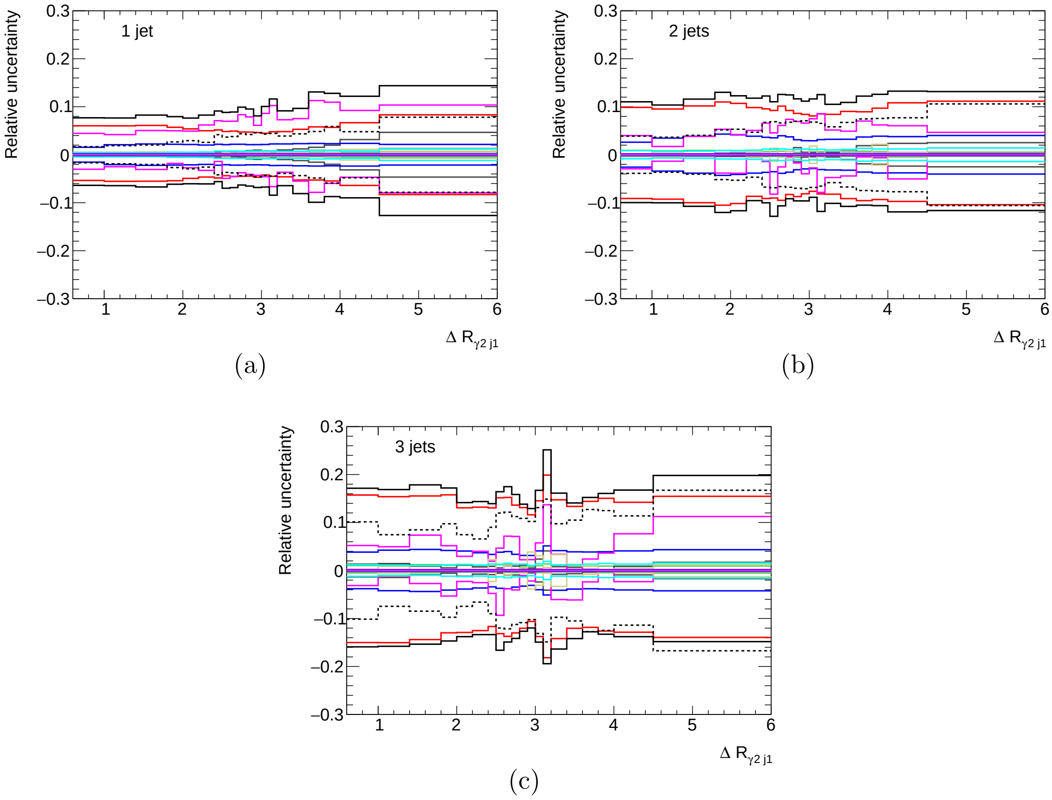

(a)

(b)

(c)

Figure A.35: *Relative systematic uncertainties as a function of the distance between subleading photon and leading jet for all inclusive jet categories.*

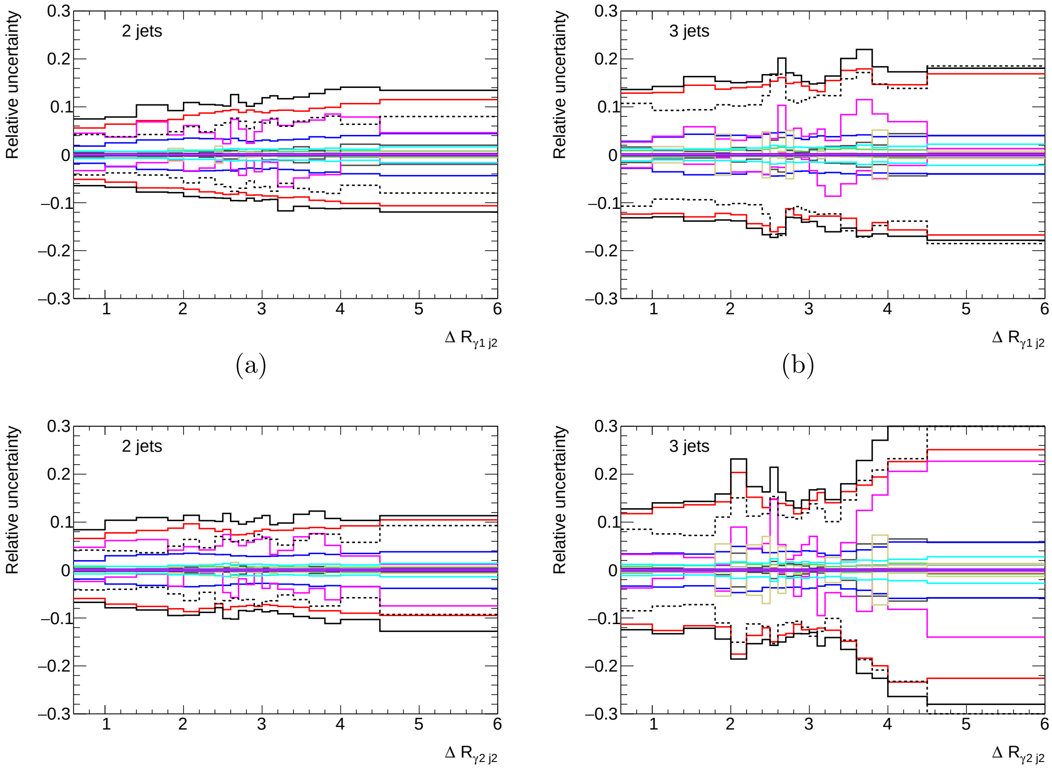

(a) (b)

(c) (d)

Figure A.36: *Relative systematic uncertainties as a function of the distance between leading photon and subleading jet (a,b) and between subleading photon and subleading jet (c,d) for* ≥ 2 *and* ≥ 3 *jets, respectively.*

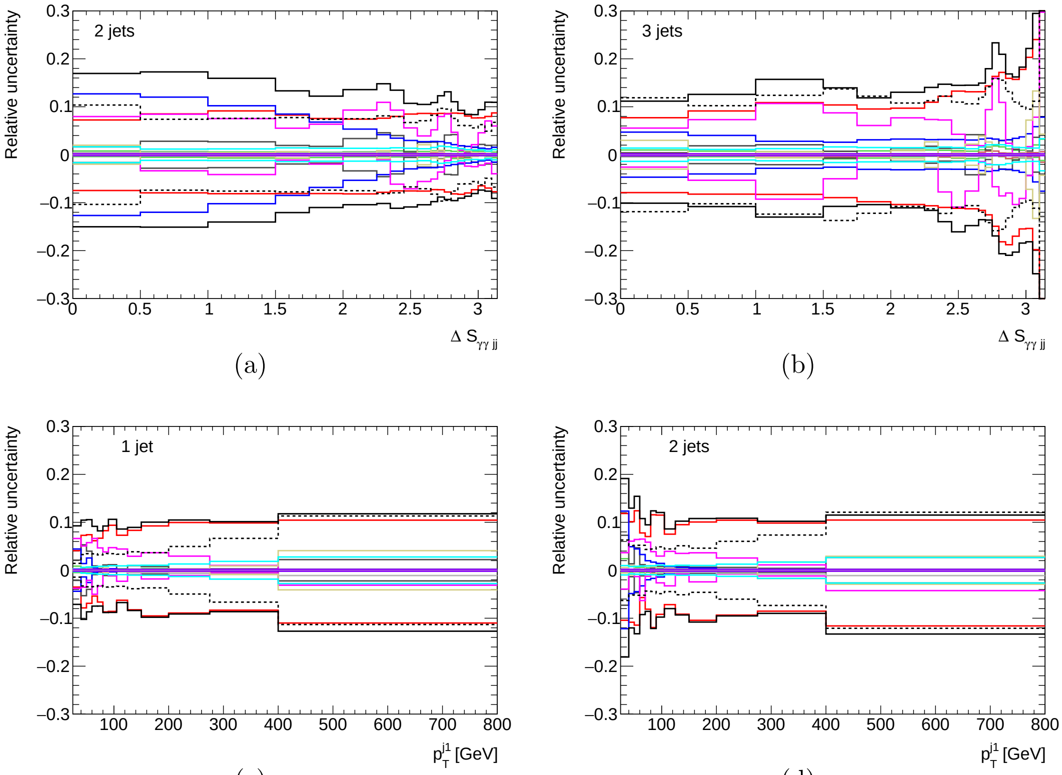

(a) (b)

(c) (d)

Figure A.37: *Relative systematic uncertainties as a function of the difference in azimuthal angle between the diphoton and the dijet system in the* $\geq$ *2-jet and* $\geq$ *3-jet categories (a,b) and the transverse momentum of the leading photon in the* $\geq$ *1-jet and* $\geq$ *2-jet categories (c,d).*

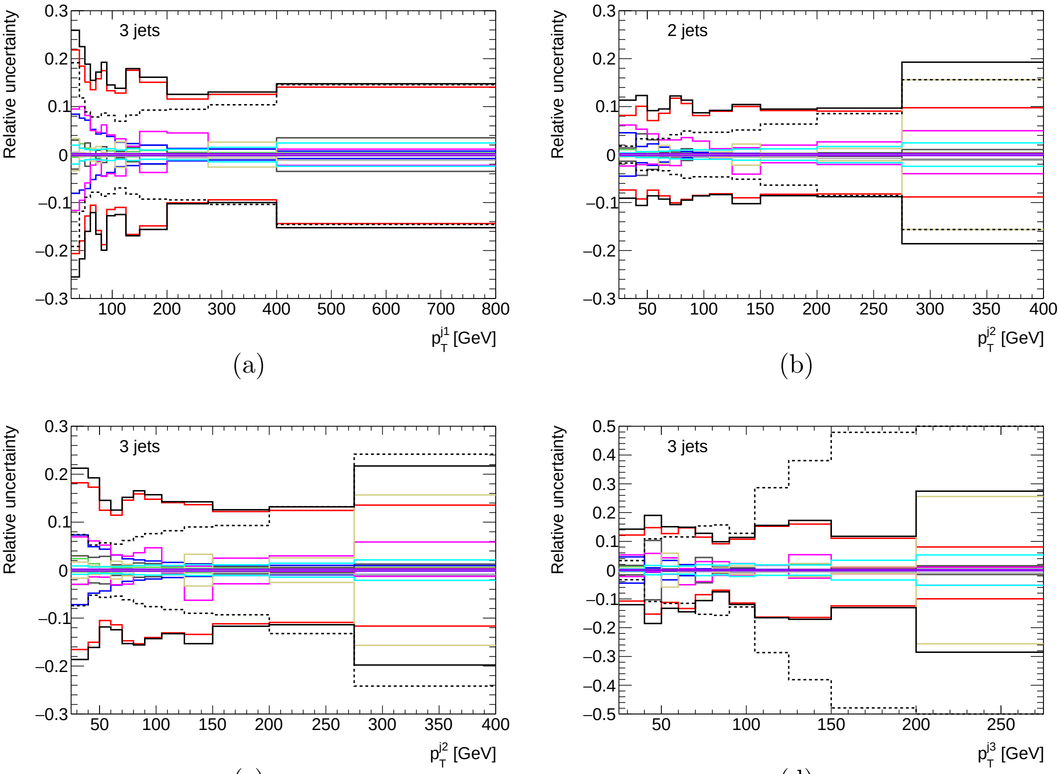

(a) (b)

(c) (d)

Figure A.38: *Relative systematic uncertainties as a function of the transverse momentum of the leading jet in the* $\geq$ *3-jet category (a), the transverse momentum of the subleading jet in the* $\geq$ *2-jet and* $\geq$ *3-jet categories (c) and the transverse momentum of the third jet in the* $\geq$ *3-jet category.*

A.5 Formulas for the different signal and background contributions to the 16 regions in the 2x2D sideband method.

This appendix contains the equations for the event yields in all 16 categories of the 2x2D sideband method, in addition to the one example shown in section 5.3.1.

$$\begin{aligned}
N_{\mathrm{TITI}} &= N_{\gamma\gamma}\varepsilon_{I1}\varepsilon_{T1}\varepsilon_{I2}\varepsilon_{T2} \\
&+ N_{\gamma j}\varepsilon_{I1}\varepsilon_{T1}f_{I2}f_{T2}\xi_{j2} \\
&+ N_{j\gamma}\varepsilon_{I2}\varepsilon_{T2}f_{I1}f_{T1}\xi_{j1} \\
&+ N_{jj}f'_{I1}f'_{T1}f'_{I2}f'_{T2}\xi_{Ijj}\xi_{j1}\xi_{j2}
\end{aligned} \tag{A.1}$$

$$\begin{aligned}
N_{\mathrm{TIT\tilde{I}}} &= N_{\gamma\gamma}\varepsilon_{I1}\varepsilon_{T1}\left(1-\varepsilon_{I2}\right)\varepsilon_{T2} \\
&+ N_{\gamma j}\varepsilon_{I1}\varepsilon_{T1}\left(1-f_{I2}\xi_{j2}\right)f_{T2} \\
&+ N_{j\gamma}f_{I1}f_{T1}\left(1-\varepsilon_{I2}\right)\varepsilon_{T2}\xi_{j1} \\
&+ N_{jj}f'_{I1}f'_{T1}\left(1-f'_{I2}\xi_{Ijj}\xi_{j2}\right)f'_{T2}\xi_{j1}
\end{aligned} \tag{A.2}$$

$$\begin{aligned}
N_{\mathrm{T\tilde{I}TI}} &= N_{\gamma\gamma}\left(1-\varepsilon_{I1}\right)\varepsilon_{T1}\varepsilon_{I2}\varepsilon_{T2} \\
&+ N_{\gamma j}\left(1-\varepsilon_{I1}\right)\varepsilon_{T1}f_{I2}f_{T2}\xi_{j2} \\
&+ N_{j\gamma}\left(1-f_{I1}\xi_{j1}\right)f_{T1}\varepsilon_{I2}\varepsilon_{T2} \\
&+ N_{jj}\left(1-f'_{I1}\xi_{Ijj}\xi_{j1}\right)f'_{T1}f'_{I2}f'_{T2}\xi_{j2}
\end{aligned} \tag{A.3}$$

$$\begin{aligned}
N_{\mathrm{T\tilde{I}T\tilde{I}}} &= N_{\gamma\gamma}\left(1-\varepsilon_{I1}\right)\left(1-\varepsilon_{I2}\right)\varepsilon_{T1}\varepsilon_{T2} \\
&+ N_{\gamma j}\left(1-\varepsilon_{I1}\right)\left(1f_{I2}\xi_{j2}\right)\varepsilon_{T1}f_{T2} \\
&+ N_{j\gamma}\left(1-\varepsilon_{I2}\right)\left(1-f_{I1}\xi_{j1}\right)\varepsilon_{T2}f_{T1} \\
&+ N_{jj}\left(1-f'_{I1}\xi_{j1}-f'_{I2}\xi_{j2}+f'_{I1}f'_{I2}\xi_{Ijj}\xi_{j1}\xi_{j2}\right)f'_{T1}f'_{T2}
\end{aligned} \tag{A.4}$$

$$\begin{aligned}
N_{\mathrm{TI\tilde{T}I}} &= N_{\gamma\gamma}\varepsilon_{I1}\varepsilon_{T1}\varepsilon_{I2}\left(1-\varepsilon_{T2}\right) \\
&+ N_{\gamma j}\varepsilon_{I1}\varepsilon_{T1}f_{I2}\left(1-f_{T2}\xi_{j2}\right) \\
&+ N_{j\gamma}f_{I1}f_{T1}\varepsilon_{I2}\left(1-\varepsilon_{T2}\right)\xi_{j1} \\
&+ N_{jj}f'_{I1}f'_{T1}f'_{I2}\left(1-f'_{T2}\xi_{j2}\right)\xi_{Ijj}\xi_{j1}
\end{aligned} \tag{A.5}$$

$$\begin{aligned} N_{\mathrm{\tilde{T}ITI}} &= N_{\gamma\gamma}\varepsilon_{I1}\left(1-\varepsilon_{T1}\right)\varepsilon_{I2}\varepsilon_{T2} \\ &+ N_{\gamma j}\varepsilon_{I1}\left(1-\varepsilon_{T1}\right)f_{I2}f_{T2}\xi_{j2} \\ &+ N_{j\gamma}f_{I1}\left(1-f_{T1}\xi_{j1}\right)\varepsilon_{I2}\varepsilon_{T2} \\ &+ N_{jj}f'_{I1}\left(1-f'_{T1}\xi_{j1}\right)f'_{I2}f'_{T2}\xi_{Ijj}\xi_{j2} \end{aligned} \tag{A.6}$$

$$\begin{aligned} N_{\mathrm{TI\tilde{T}\tilde{I}}} &= N_{\gamma\gamma}\varepsilon_{I1}\varepsilon_{T1}\left(1-\varepsilon_{I2}\right)\left(1-\varepsilon_{T2}\right) \\ &+ N_{\gamma j}\varepsilon_{I1}\varepsilon_{T1}\left(1-f_{I2}-f_{T2}+f_{I2}f_{T2}\xi_{j2}\right) \\ &+ N_{j\gamma}f_{I1}f_{T1}\xi_{j1}\left(1-\varepsilon_{I2}\right)\left(1-\varepsilon_{T2}\right) \\ &+ N_{jj}\xi_{j1}f'_{I1}f'_{T1}\left(1-\xi_{Ijj}f'_{I2}-f'_{T2}+f'_{I2}f'_{T2}\xi_{j2}\xi_{Ijj}\right) \end{aligned} \tag{A.7}$$

$$\begin{aligned} N_{\mathrm{\tilde{T}\tilde{I}TI}} &= N_{\gamma\gamma}\left(1-\varepsilon_{I1}\right)\left(1-\varepsilon_{T1}\right)\varepsilon_{I2}\varepsilon_{T2} \\ &+ N_{\gamma j}\left(1-\varepsilon_{I1}\right)\left(1-\varepsilon_{T1}\right)f_{I2}f_{T2}\xi_{j2} \\ &+ N_{j\gamma}\left(1-f_{I1}-f_{T1}+f_{I1}f_{T1}\xi_{j1}\right)\varepsilon_{I2}\varepsilon_{T2} \\ &+ N_{jj}\left(1-f'_{I1}\xi_{Ijj}-f'_{T1}+f'_{I1}f'_{T1}\xi_{j1}\xi_{Ijj}\right)f'_{I2}f'_{T2}\xi_{j2} \end{aligned} \tag{A.8}$$

$$\begin{aligned} N_{\mathrm{T\tilde{I}\tilde{T}I}} &= N_{\gamma\gamma}\left(1-\varepsilon_{I1}\right)\varepsilon_{T1}\varepsilon_{I2}\left(1-\varepsilon_{T2}\right) \\ &+ N_{\gamma j}\left(1-\varepsilon_{I1}\right)\varepsilon_{T1}f_{I2}\left(1-f_{T2}\xi_{j2}\right) \\ &+ N_{j\gamma}\left(1-f_{I1}\xi_{j1}\right)f_{T1}\varepsilon_{I2}\left(1-\varepsilon_{T2}\right) \\ &+ N_{jj}\left(1-f'_{I1}\xi_{Ijj}\xi_{j1}\right)f'_{T1}f'_{I2}\left(1-f'_{T2}\xi_{j2}\right) \end{aligned} \tag{A.9}$$

$$\begin{aligned} N_{\mathrm{\tilde{T}IT\tilde{I}}} &= N_{\gamma\gamma}\varepsilon_{I1}\left(1-\varepsilon_{T1}\right)\left(1-\varepsilon_{I2}\right)\varepsilon_{T2} \\ &+ N_{\gamma j}\varepsilon_{I1}\left(1-f_{I2}\xi_{j2}\right)\left(1-\varepsilon_{T1}\right)f_{T2} \\ &+ N_{j\gamma}f_{I1}\left(1-\varepsilon_{I2}\right)\left(1-f_{T1}\xi_{j1}\right)\varepsilon_{T2} \\ &+ N_{jj}f'_{I1}\left(1-f'_{T1}\xi_{j1}\right)\left(1-f'_{I2}\xi_{Ijj}\xi_{j2}\right)f'_{T2} \end{aligned} \tag{A.10}$$

$$\begin{aligned} N_{\mathrm{\tilde{T}I\tilde{T}I}} &= N_{\gamma\gamma}\varepsilon_{I1}\left(1-\varepsilon_{T1}\right)\varepsilon_{I2}\left(1-\varepsilon_{T2}\right) \\ &+ N_{\gamma j}\varepsilon_{I1}\left(1-\varepsilon_{T1}\right)f_{I2}\left(1-f_{T2}\xi_{j2}\right) \\ &+ N_{j\gamma}f_{I1}\left(1-f_{T1}\xi_{j1}\right)\varepsilon_{I2}\left(1-\varepsilon_{T2}\right) \\ &+ N_{jj}f'_{I1}f'_{I2}\left(1-f'_{T1}\xi_{j1}-f'_{T2}\xi_{j2}+f'_{T1}f'_{T2}\xi_{j1}\xi_{j2}\right)\xi_{Ijj} \end{aligned} \tag{A.11}$$

$$\begin{aligned}
N_{\mathrm{T\tilde{I}\tilde{T}\tilde{I}}} &= N_{\gamma\gamma}\left(1-\varepsilon_{I1}\right)\varepsilon_{T1}\left(1-\varepsilon_{I2}\right)\left(1-\varepsilon_{T2}\right)\\
&+ N_{\gamma j}(\left(1-\varepsilon_{I1}\right)\varepsilon_{T1}\left(1-f_{I2}-f_{T2}+f_{I2}f_{T2}\xi_{j2}\right)\\
&+ N_{\gamma g}\left(1-f_{I1}\xi_{j1}\right)f_{T1}\left(1-\varepsilon_{T2}\right)\left(1-\varepsilon_{I2}\right)\\
&+ N_{jj}f'_{T1}\left(1-f'_{I2}-f'_{T2}-f'_{I1}\xi_{j1}+f'_{I2}f'_{T2}\xi_{j2}+f'_{T2}f'_{I1}\xi_{j1}+f'_{I2}f'_{I1}\xi_{Ijj}\xi_{j1}-f'_{I1}f'_{I2}f'_{T2}\xi_{Ijj}\xi_{j1}\xi_{j2}\right)
\end{aligned}\tag{A.12}$$

$$\begin{aligned}
N_{\mathrm{\tilde{T}\tilde{I}T\tilde{I}}} &= N_{\gamma\gamma}\left(1-\varepsilon_{I1}\right)\left(1-\varepsilon_{T1}\right)\left(1-\varepsilon_{I2}\right)\varepsilon_{T2}\\
&+ N_{\gamma j}\left(1-\varepsilon_{I1}\right)\left(1-\varepsilon_{T1}\right)\left(1-f_{I2}\xi_{j2}\right)f_{T2}\\
&+ N_{j\gamma}\left(1-f_{I1}-f_{T1}+f_{I1}f_{T1}\xi_{j1}\right)\left(1-\varepsilon_{I2}\right)\varepsilon_{T2}\\
&+ N_{jj}\left(1-f'_{I1}-f'_{T1}-f'_{I2}\xi_{j2}+f'_{I1}f'_{T1}\xi_{j1}+f'_{T1}f'_{I2}\xi_{j2}+f'_{I1}f'_{I2}\xi_{Ijj}\xi_{j2}-f'_{I1}f'_{T1}f'_{I2}\xi_{Ijj}\xi_{j1}\xi_{j2}\right)f'_{T2}
\end{aligned}\tag{A.13}$$

$$\begin{aligned}
N_{\mathrm{\tilde{T}I\tilde{T}\tilde{I}}} &= N_{\gamma\gamma}\varepsilon_{I1}\left(1-\varepsilon_{T1}\right)\left(1-\varepsilon_{I2}\right)\left(1-\varepsilon_{T2}\right)\\
&+ N_{\gamma j}\varepsilon_{I1}\left(1-\varepsilon_{T1}\right)\left(1-f_{I2}-f_{T2}+f_{I2}f_{T2}\xi_{j2}\right)\\
&+ N_{j\gamma}f_{I1}\left(1-f_{T1}\xi_{j1}\right)\left(1-\varepsilon_{I2}\right)\left(1-\varepsilon_{T2}\right)\\
&+ N_{jj}f'_{I1}\left(\left(1-f'_{T1}\xi_{j1}\right)\left(1-f'_{I2}\xi_{Ijj}\right)-f'_{T2}\left(1-f'_{T1}\xi_{j1}\right)\left(1-f'_{I2}\xi_{j2}\xi_{Ijj}\right)\right)
\end{aligned}\tag{A.14}$$

$$\begin{aligned}
N_{\mathrm{\tilde{T}\tilde{I}\tilde{T}I}} &= N_{\gamma\gamma}\varepsilon_{I2}\left(\left(1-\varepsilon_{T2}\right)\left(1-\varepsilon_{I1}\right)-\varepsilon_{T1}\left(1-\varepsilon_{T2}\right)\left(1-\varepsilon_{I1}\right)\right)\\
&+ N_{\gamma j}f_{I2}\left(\left(1-\varepsilon_{I1}\right)\left(1-f_{T2}\xi_{j2}\right)-\varepsilon_{T1}\left(1-\varepsilon_{I1}\right)\left(1-f_{T2}\xi_{j2}\right)\right)\\
&+ N_{j\gamma}\varepsilon_{I2}\left(\left(1-\varepsilon_{T2}\right)\left(1-f_{I1}\right)-f_{T1}\left(1-f_{I1}\xi_{j1}\right)\left(1-\varepsilon_{T2}\right)\right)\\
&+ N_{jj}\left(\left(1-f'_{T2}\xi_{j2}\right)\left(1-f'_{I1}\xi_{Ijj}\right)-f'_{T1}\left(1-f'_{T2}\xi_{j2}\right)\left(1-f'_{I1}\xi_{j1}\xi_{Ijj}\right)\right)f'_{I2}
\end{aligned}\tag{A.15}$$

$$\begin{aligned}
N_{\mathrm{\tilde{T}\tilde{I}\tilde{T}\tilde{I}}} &= N_{\gamma\gamma}\left(1-\varepsilon_{T1}-\varepsilon_{T2}+\varepsilon_{T1}\varepsilon_{T2}+\varepsilon_{I2}\left(1-\varepsilon_{T1}-\varepsilon_{T2}+\varepsilon_{T1}\varepsilon_{T2}\right)+\varepsilon_{I1}\left(-\left(1-\varepsilon_{I2}\right)\left(1-\varepsilon_{T1}\right)+\varepsilon_{T2}\left(1-\varepsilon_{I2}\right)\left(1-\varepsilon_{T1}\right)\right)\right)\\
&+ N_{\gamma j}\left(1-\varepsilon_{T1}-f_{T2}+\varepsilon_{T1}f_{T2}+f_{I2}\left(1-\varepsilon_{T1}-f_{T2}\xi_{j2}+\varepsilon_{T1}f_{T2}\xi_{j2}\right)+\varepsilon_{I1}\left(\left(1-\varepsilon_{T1}\right)\left(1-f_{I2}\right)+f_{T2}\left(1-f_{I2}\xi_{j2}\right)\left(1-\varepsilon_{T1}\right)\right)\right)\\
&+ N_{j\gamma}\left(1-\varepsilon_{T2}-f_{T1}+\varepsilon_{T2}f_{T1}+\varepsilon_{I2}\left(1-f_{T1}-\varepsilon_{T2}+\varepsilon_{T2}f_{T1}\right)+f_{I1}\left(\left(1-\varepsilon_{I2}\right)\left(1-f_{T1}\xi_{j1}\right)+\varepsilon_{T2}\left(1-\varepsilon_{I2}\right)\left(1-f_{T1}\xi_{j1}\right)\right)\right)\\
&+ N_{jj}\left(1-f'_{T1}-f'_{T2}+f'_{T1}f'_{T2}+f'_{I2}\left(1-f'_{T1}-f'_{T2}\xi_{j2}+f'_{T1}f'_{T2}\xi_{j2}\right)\right)\\
&+ N_{jj}\left(f'_{I1}\left(-\left(1-f'_{I2}\xi_{Ijj}\right)\left(1-f'_{T1}\xi_{j1}\right)+f'_{T2}\left(1-f'_{I2}\xi_{Ijj}\xi_{j2}\right)\left(1-f'_{T1}\xi_{j1}\right)\right)\right)
\end{aligned}\tag{A.16}$$

Bibliography

[1] ATLAS and CMS collaboration, *Measurements of the Higgs boson production and decay rates and constraints on its couplings from a combined ATLAS and CMS analysis of the LHC pp collision data at* $\sqrt{s} = 7$ *and 8 TeV*, JHEP **08** (2016) 045

[2] LHC Team, *LHC Report: end of 2016 proton-proton operation.* https://home.cern/cern-people/updates/2016/10/lhc-report-end-2016-proton-proton-operation

[3] ATLAS collaboration, *The ATLAS Experiment at the CERN Large Hadron Collider*, 2008 JINST 3 S08003

[4] https://twiki.cern.ch/twiki/bin/view/AtlasPublic/LuminosityPublicResults

[5] ATLAS collaboration, *ATLAS Pixel Detector Electronics and Sensors*, 2008 JINST 3 P07007

[6] M. Capeans et al., *ATLAS Insertable B-Layer Technical Design Report*, CERN-LHCC-2010-013

[7] A. Ahmad et al., *The silicon microstrip sensors of the ATLAS semiconductor tracker*, Nucl. Instrum. Meth. **A 578** (2007) 98

[8] E. Abat et al., *The ATLAS Transition Radiation Tracker (TRT) proportional drift tube: Design and performance*, 2008 JINST 3 P02013

[9] A. S. Boldyrev, A. S. Maevskiy, *Simulation of the transition radiation detection conditions in the ATLAS TRT detector filled with argon and krypton gas mixtures*, Phys.Atom.Nucl. **78** (2015) no.13, 1552-1555

[10] ATLAS collaboration, *Liquid argon calorimeter technical design report*, CERN-LHCC-96-041

[11] M. L. Andrieux et al., *Construction and test of the first two sectors of the ATLAS barrel liquid argon presampler*, Nucl. Instrum. Meth. **A 479** (2002) 316

[12] ATLAS collaboration, *Tile calorimeter technical design report*, CERN-LHCC-96-042

[13] ATLAS collaboration, *The ATLAS Tile Calorimeter*, ATL-TILECAL-PROC-2015-002

[14] S. Palestini, *The muon spectrometer of the ATLAS experiment*, Nucl. Phys. **125** (Proc Suppl.) (2003) 337

[15] B. Odom, D. Hanneke, B. D'Urso, G. Gabrielse, *New Measurement of the Electron Magnetic Moment Using a One-Electron Quantum Cyclotron*, Phys. Rev. Lett. **97**, 030801

[16] W. Pauli, *The Connection Between Spin and Statistics*, Physical Review. **58** (8): 716722

[17] Original figure by Wikimedia author MissMJ, https://commons.wikimedia.org/wiki/File:Standard_Model_of_Elementary_Particles.svg, updated Higgs boson mass and removed neutrino masses.

[18] P. W. Higgs, *Broken symmetries, massless particles and gauge fields*, Phys. Lett. **12** (1964) 132.

[19] F. Englert, R. Brout, *Broken symmetry and the mass of gauge vector mesons*, Phys. Rev. Lett. **13** (1964) 321

[20] G. S. Guralnik, C. R. Hagen, T. W. B. Kibble, *Global conservation laws and massless particles*, Phys. Rev. Lett. **13** (1964) 585

[21] ATLAS collaboration, *Observation of a New Particle in the Search for the Standard Model Higgs Boson with the ATLAS Detector at the LHC*, Physics Letters B. **716** (1): 129

[22] CMS collaboration, *Observation of a new boson at a mass of 125 GeV with the CMS experiment at the LHC*, Physics Letters B. **716** (1): 3061

[23] V. Trimble, *Existence and Nature of Dark Matter in the Universe*, Ann. Rev. Astron. Astrophys. 1987. 25: 425-72

[24] N. deGrasse Tyson, D. Goldsmith, *Origins: Fourteen Billion Years of Cosmic Evolution*, W. W. Norton & Co., 2004. pp. 845.

[25] D.J. Gross; F. Wilczek, *Ultraviolet behavior of non-abelian gauge theories*, Physical Review Letters. 30 (26): 13431346

[26] *On the Quantum Theory of Field*, in *Niels Bohr and the Development of Physics (ed. W. Pauli)* (Pergamon, London, 1955), p. 52

[27] N. ArkaniHamed, S. Dimopoulos, G. Dvali, *The hierarchy problem and new dimensions at a millimeter*, Phys.Lett. **B429** (34): 262-272

[28] A. Arbey, M. Battaglia, A. Djouadi, F. Mahmoudi, J. Quevillon, *Implications of a 125 GeV Higgs for supersymmetric models*, Phys.Lett. **B708** (2012) 162-169

[29] Rajan Gupta, *Introduction to Lattice QCD*, https://arxiv.org/abs/hep-lat/9807028

[30] T. Gehrmann, N. Greiner, G. Heinrich, *Precise QCD predictions for the production of a photon pair in association with two jets*, Phys.Rev.Lett. **111** (2013) 222002

[31] T. Gleisberg et al., *Event generation with SHERPA 1.1*, JHEP **0902** (2009) 007

[32] T. Sjostrand, S. Mrenna, P. Z. Skands, *A Brief Introduction to PYTHIA 8.1*, Comput. Phys. Commun. **178** (2008) 852

[33] S. Dooling, P. Gunnellini, F. Hautmann, H. Jung, *Longitudinal momentum shifts, showering and nonperturbative corrections in matched NLO-shower event generators*, Phys. Rev. D **87**, 094009

[34] https://twiki.cern.ch/twiki/bin/view/AtlasPublic

[35] https://twiki.cern.ch/twiki/bin/view/AtlasPublic/HiggsPublicResults

[36] https://twiki.cern.ch/twiki/bin/view/AtlasPublic/StandardModelPublicResults

[37] ATLAS collaboration, *Measurement of the production cross section of an isolated photon associated with jets in proton-proton collisions at* $\sqrt{s}$ *= 7 TeV with the ATLAS detector*, Phys. Rev. **D85** (2012) 092014

[38] ATLAS collaboration, *Measurement of the cross section for inclusive isolated-photon production in pp collisions at* $\sqrt{s}$*=13 TeV using the ATLAS detector*, CERN-EP-2016-291, submitted to Physics Letters **B**

[39] ATLAS collaboration, *Dynamics of isolated-photon plus jet production in pp collisions at sqrt(s) = 7 TeV with the ATLAS detector*, Nucl.Phys. **B875** (2013) 483535

[40] ATLAS collaboration, *High-*E_{T} *isolated-photon plus jets production in pp collisions at* $\sqrt{s}$*= 8 TeV with the ATLAS detector*, CERN-EP-2016-252, submitted to Nuclear Physics **B**

[41] ATLAS collaboration, *Measurement of isolated-photon pair production in pp collisions at* $\sqrt{s} = 7$ *TeV with the ATLAS detector*, JHEP **1301** (2013) 086

[42] ATLAS collaboration, *Measurements of integrated and differential cross sections for isolated photon pair production in pp collisions at sqrt(s)=8TeV with the ATLAS detector*, https://atlas.web.cern.ch/Atlas/GROUPS/PHYSICS/PAPERS/STDM-2015-15/

[43] ATLAS collaboration, *Performance of the ATLAS Trigger System in 2015*, CERN-EP-2016-241

[44] Matteo Cacciari, Gavin P. Salam, Gregory Soyez, *The anti-k t jet clustering algorithm*, JHEP04(2008)063

[45] Ariel Schwartzman, *Jet energy calibration at the LHC*, https://arxiv.org/abs/1509.05459

[46] ATLAS collaboration, *Electron and photon energy calibration with the ATLAS detector using LHC Run 1 data*, Eur.Phys.J. **C74**.10 (2014) 3071

[47] ATLAS collaboration, *Measurement of the photon identification efficiencies with the ATLAS detector using LHC Run-1 data*, Eur. Phys. J. **C 76** (2016) 666

[48] ATLAS collaboration, *Measurement of the inclusive isolated prompt photon cross section in pp collisions at* $\sqrt{s}$*=7TeV with the ATLAS detector*, Phys. Rev. D **83**, 052005

[49] M. Hance, *Photon Physics at the LHC*, Springer Science & Business Media

[50] ATLAS e/γ Combined Performance Group, *Calorimeter shower shapes of photons from* $Z \to ll\gamma$ *decays in 20.3* fb^{-1} *of pp collisions collected by ATLAS at* $\sqrt{s}$*=8 TeV in 2012*, ATL-COM-PHYS-2013-600

[51] ATLAS Collaboration, *Photon identification in 2015 ATLAS data*, ATLAS-PHYS-PUB-2016-014

[52] ATLAS internal documentation: HSG1 Working Group, *Improved analysis of the Search for the Higgs Boson Decaying to Two Photons with 4.9* fb^{-1} *of 7TeV data*, ATL-COM-PHYS-2012-502

[53] A. Hoecker, P. Speckmayer, J. Stelzer, J. Therhaag, E. von Toerne, H. Voss, *TMVA 4 Toolkit for Multivariate Data Analysis with ROOT Users Guide*, Cern Open Documents, October 2013.

[54] V. Del Duca et al., *QCD radiative corrections to prompt diphoton production in association with a jet at hadron colliders*, JHEP **0304** (2003) 059

[55] T. Gehrmann, N. Greiner, G. Heinrich, *Photon isolation effects at NLO in gamma gamma + jet final states in hadronic collisions*, JHEP **1306** (2013) 058

[56] Z. Bern et al., *Next-to-leading order diphoton+2-jet production at the LHC (2013)*, arXiv: 1312.0592 [hep-ph].

[57] S. Badger, A. Guffanti, V. Yundin, *Next-to-leading order QCD corrections to di-photon production in association with up to three jets at the Large Hadron Collider*, JHEP03(2014)122

[58] T. Aaltonen et al., *Measurement of the cross section for prompt isolated diphoton production using the full CDF Run II data sample*, Phys.Rev.Lett. **110**.10 (2013) 101801

[59] V. M. Abazov et al., *Measurement of direct photon pair production cross sections in* $p\bar{p}$ *collisions at* $\sqrt{s} = 1.96$ *TeV*, Phys.Lett. **B690** (2010) 108117

[60] V. Abazov et al., *Measurement of the differential cross sections for isolated direct photon pair production in* $p\bar{p}$ *collisions at* $\sqrt{s} = 1.96$ *TeV*, Phys.Lett. **B725** (2013) 614

[61] ATLAS collaboration, *Measurement of the isolated diphoton cross-section in pp collisions at* $\sqrt{s} = 7$ *TeV with the ATLAS detector*, Phys.Rev. **D85** (2012) 012003

[62] CMS collaboration, *Measurement of the Production Cross Section for Pairs of Isolated Photons in pp collisions at* $\sqrt{s} = 7$ *TeV*, JHEP **01** (2012) 133

[63] CMS collaboration, *Measurement of differential cross sections for the production of a pair of isolated photons in pp collisions at* $\sqrt{s} = 7$ *TeV*, Eur.Phys.J. **C74**.11 (2014) 3129

[64] CMS collaboration, *Production of pairs of isolated photons in association with jets in pp collisions at* $\sqrt{s} = 7$ *TeV*, CMS-PAS-SMP-14-021

[65] J. Collins, D. Soper, *Angular distribution of dileptons in high-energy hadron collisions*, Phys. Rev. D **16**, 2219

[66] D. Damazio et al., *Performance of the ATLAS Electron and Photon Triggers in p-p Collisions at* $\sqrt{s} = 8$ *TeV in 2012*, ATL-COM-DAQ-2013-121 (2013)

[67] ATLAS data quality information for run 1: https://twiki.cern.ch/twiki/bin/view/AtlasPublic/RunStatsPublicResults2010

[68] J. Gao et al., *CT10 next-to-next-to-leading order global analysis of QCD*, Phys.Rev. **D89**.3 (2014) 033009

[69] J. Pumplin et al., *New generation of parton distributions with uncertainties from global QCD analysis*, JHEP **0207** (2002) 012

[70] S. Agostinelli et al., *Geant4 a simulation toolkit*, Nucl. Instrum. Meth. **A 506** (2003) 250

[71] T. Binoth et al., *A Full next-to-leading order study of direct photon pair production in hadronic collisions*, Eur.Phys.J. **C16** (2000) 311330

[72] ATLAS Collaboration, *Pile-up subtraction and suppression for jets in ATLAS*, ATLAS-CONF-2013-083

[73] ATLAS internal documentation: HSG1 Group, *Selection for $H \rightarrow$ gammagamma analysis supporting note, for Moriond 2013*, ATL-COM-PHYS-2013-093

[74] Z. Barnovska, *Diphoton measurements with the ATLAS detector at the LHC: search for new resonances and study of diphoton production in association with jets*, CERN-THESIS-2015-167

[75] ATLAS internal documentation: M. Stoebe et al., *Measurement of the inclusive isolated prompt photon cross section in pp collisions at $\sqrt{s} = 8$ TeV with the ATLAS detector using 20.2 fb 1*, ATL-COM-PHYS-2014-744

[76] ATLAS collaboration, *Electron reconstruction and identification efficiency measurements with the ATLAS detector using the 2011 LHC proton-proton collision data*, Eur. Phys. J. C (2014) 74:2941

[77] T. Skwarnicki, *A study of the radiative CASCADE transitions between the Upsilon-Prime and Upsilon resonances*, DESY-F31-86-02 (1986)

[78] L. J. Dixon, Y. Li, *Bounding the Higgs Boson Width Through Interferometry*, Phys.Rev.Lett. **111** (2013) 111802

[79] ATLAS Collaboration, *Performance of the ATLAS Electron and Photon Trigger in p-p Collisions at sqrts = 7 TeV in 2011*, ATLAS-CONF-2012-048

[80] A. Höcker, V. Kartvelishvili, *SVD Approach to Data Unfolding*, Nucl.Instrum.Meth. A372:469-481 (1996)

[81] ATLAS Collaboration, *A measurement of the calorimeter response to single hadrons and determination of the jet energy scale uncertainty using LHC Run-1 pp-collision data with the ATLAS detector*, Eur. Phys. J. C (2017) 77:26

[82] ATLAS Collaboration, *Measurements of fiducial and differential cross sections for Higgs boson production in the diphoton decay channel at $\sqrt{s} = 8$ TeV with ATLAS*, JHEP **09** (2014) 112

[83] ATLAS Collaboration, *Luminosity Determination in pp Collisions at* $\sqrt{s} = 8$ *TeV using the ATLAS Detector at the LHC*, Eur. Phys. J. **C 76** (2016) 653

Acknowledgments

Ich möchte mich bei allen bedanken, die zum Entstehen dieser Arbeit beigetragen haben. Dies sind insbesondere:

- Kerstin Tackmann als Betreuerin meiner Doktorarbeit, die auch immer wieder gute Anregungen zur Analyse hatte
- Peter Schleper, der sich ebenfalls als Betreuer zur Verfügung gestellt hat
- Ingrid Gregor als Gruppenleiterin und als Betreuerin bei meiner Autorenqualifikation
- Zuzana Barnovská, für die Zusammenarbeit in vielen Aspekten der Analyse
- Marcello Fanti, Elisabeth Petit und Marco Delmastro als weitere Mitarbeiter der Analysegruppe
- Phillip Hamnett und Fernando Monticelli, für die Zusammenarbeit bei der Photonidentifikation
- Richard Peschke, Nils Flaschel, Daniel Rauch und Alexander Morton, die oft bei Fragen weiterhelfen konnten
- Die gesamte ATLAS-Gruppe in Hamburg
- Die ATLAS-Kollaboration
- Meine Familie
- Und alle, die ich an dieser Stelle vergessen habe

Erklärung

Ich versichere, dass ich diese Arbeit selbstständig verfasst und keine anderen als die angegebenen Quellen und Hilfsmittel benutzt habe.

Hamburg, den 04. April 2017